



DOCTORAL THESIS

**Observational Study of Umbral Dots.
Manifestation of Magnetoconvection in a
Solar Sunspot**

Umbral Dotに関する観測的研究
太陽黒点における磁気対流現象

Hiroko WATANABE

渡邊 皓子

Kwasan and Hida Observatories, Department of Astronomy,
Faculty of Science, Kyoto University

Oiwake-cho Kita-shirakawa, Sakyo-ku, Kyoto City, Kyoto,
606-8502, JAPAN

January 19, 2012

Acknowledgments

First of all, I would like to express my sincere gratitude and appreciation to my supervisor, Dr. Reizaburo Kitai, for his continuous supports and stimulating discussions. He suggested me to study the fine scale structures of sunspots for my research topic. The topic attracted me, and his experiences on observation and his knowledge on the radiative transfer greatly helped me in the research. Prof. Kiyoshi Ichimoto, my vice supervisor, provided me many instrumental information about the *Hinode* and the Domeless Solar Telescope. His profound knowledge about sunspots arose my enthusiasm for the research of sunspots. I would like to thank Prof. Kazunari Shibata and Dr. Hiroaki Isobe for supporting me by their theoretical insights. Discussions with researchers in the National Astronomical Observatory of Japan, especially Dr. Yukio Katsukawa and Prof. Saku Tsuneta, were always beneficial and helpful.

I am grateful to scientists in Oslo University, Norway, and Institute de Astrofísica de Andalucía, Spain, for their great hospitalities. I had been privileged to have opportunities to stay their institutes for several months and had great experiences and collaborative researches. Prof. Mats Carlsson in Oslo University provided a rare opportunity to visit La Palma and observe with the outstanding solar telescope on La Palma. Prof. Luis Ramon Bellot Rubio kindly invited me for a collaborative work of umbral fine structure using their superb data set. I am also grateful to Dr. Alexandra Tritschler, who is one of my co-authors, for helping the analysis of Interferometric BI-dimensional Spectrometer data obtained at the Dunn Solar Telescope.

I wish to acknowledge all the members of Kwasan and Hida Observatories and my fellow colleagues in Kyoto University. I owe much to them for offering me many helpful comments and suggestions, and making my school life enjoyable.

The author is grateful to the operation team of the *Hinode* satellite, the National Solar Observatory, and the Swedish Solar Telescope for offering excellent images of sunspots.

Finally, I would like to express my sincere thanks to my husband, my parents, my sister, and my sweet little daughter for their sincere understandings and generous supports. Without their support, this work could not be completed.

This work is financially supported by a Grant-in-Aid for JSPS Fellows, and a Grant-in-Aid for Creative Scientific Research “The Basic Study of Space Weather Prediction” (Head Investigator: K. Shibata) from Ministry of Education, Culture, Sports, Science and Technology (MEXT), Japan, donation from the Sun Microsystems Inc.. I also receive financial support from the Grant-in-Aid for the Global COE Program “The Next Generation of Physics, Spun from Universality and Emergence” from the MEXT of Japan.

Preface

Sunspots are one of the oldest well-known and at the same time most mysterious scientific objectives in astronomy. Sunspots are the manifestations of the intense magnetic-flux concentrations on the solar surface, and magnetic field plays the most important role on solar energetic activities such as flares and coronal mass ejections. Accordingly sunspots are the main sites of solar activities. The full understanding of the sunspot structure and its evolution is an ultimate mission for understanding the stellar activities.

A sunspot consists of a dark umbra and an annular penumbra encompassing the umbra. An umbra is a dark region with intense vertical magnetic fields. A penumbra consists of thin filamentary structures with inclined magnetic fields. In the sunspot, the convection is suppressed by the strong magnetic field. However there exist a modified convection pattern intersected with the magnetic field, namely, “the magnetoconvection”. The manifestation of magnetoconvection in the umbra is observed as bright points called umbral dots (UDs). UD’s are small (~ 300 km) and short-lived (~ 10 minutes) bright points seen all over the umbra. They are present in all sunspots and pores without exceptions. The convection carries heat to the umbral surface from deep layer, and thus UD’s are about 1000 K hotter than the coolest part of the umbra. They cover only 3–10% of the umbral area, but contribute 10–20% of the total umbral brightness. As UD’s have their origin in the subsurface layer, they act as a valuable observation target to draw information about the unknown subsurface structure of the sunspot.

The author have two objectives about studying the UD’s. First objective is the establishment of their observational properties, i.e., UD’s size, lifetime, motion, velocity field, magnetic field, and especially their temporal evolutions. At present, only a few literature report the temporal evolution of UD’s, because they are one of the most challenging targets owing to their small spatial scale and short dynamic time scale. Only recently it became possible to address their temporal evolutions using the high resolution observations. Second objective is to investigate the subsurface structure of the sunspot based on the convective properties of UD’s. A detailed comparison between computer simulations and theoretical calculations on magnetoconvection is the key to this work. The observation helps to improve the validity of computer simulations in a complementary way.

This thesis will describe the observational properties of UD’s and insights to the subsurface structure of sunspot. This thesis is organized as follows: Section 1 is the general introduction to solar sunspots and their fine scale structures. Section 2 is dedicated for the introduction of theoretical works on the magnetoconvection. Section 3 describes the author’s motivation of studying UD’s. Section 4 to Section 6 are summarizing reviews of the following three scientific publications

on which this thesis is based:

- Hiroko Watanabe, Alexandra Tritschler, Reizaburo Kitai, and Kiyoshi Ichimoto, “*Temporal Evolution of a Rapidly-Moving Umbral Dot*”, *Solar Physics*, 266, 5-16 (2010) [Section 4]
- Hiroko Watanabe, Reizaburo Kitai, and Kiyoshi Ichimoto, “*Characteristic Dependence of Umbral Dots on their Magnetic Structure*”, *The Astrophysical Journal*, 702, 1048-1057 (2009) [Section 5]
- Hiroko Watanabe, and Luis Ramon Bellot Rubio, “*Temporal Evolution of Velocity and Magnetic Field in and around Umbral Dots*”, submitted to the *Astrophysical Journal* [Section 6]

Section 7 gives a summary, open issues, and concluding remarks.

Contents

Preface	2
1 Introduction	7
1.1 Introduction of Sunspots	7
1.1.1 Overview	7
1.1.2 History of Sunspot Observations	9
1.1.3 Magnetic Field Structure and their Origin	11
1.1.4 Fine Scale Structures Inside Sunspots	15
Penumbral filament	15
Light bridge	17
Umbral Dots	17
1.2 Magnetoconvection	21
1.2.1 Equation of Magnetoconvection	21
1.2.2 Two Convection Modes : Overturning and Oscillatory .	22
1.2.3 Simulation of Magnetoconvection in a Sunspot Umbra	24
1.3 Motivations of Studying Umbral Dots	27
1.3.1 The Importance and Difficulty of Studying Umbral Dots	27
1.3.2 The Contents of this Thesis	28
2 Temporal Evolution of a Rapidly-Moving Umbral Dot	34
2.1 Introduction	34
2.2 Observations and Data Reduction	36

<i>CONTENTS</i>	5
2.3 Line Profile Analysis	38
2.4 Results	42
2.4.1 The Position of the Rapidly-Moving Umbral Dot . . .	44
2.4.2 The Temporal Variation of the Umbral Dot	44
2.5 Discussion	47
3 Characteristic Dependence of Umbral Dots	52
3.1 Introduction	52
3.2 Observation and Data Reduction	54
3.3 Automatic Detection Algorithm	55
3.4 Results	59
3.4.1 Histogram	61
3.4.2 Scatter Diagrams	61
3.4.3 Spatial Distribution	62
3.4.4 Light Curve	65
3.5 Discussion	67
4 Temporal Evolution of Velocity and Magnetic Field	74
4.1 Introduction	74
4.2 Observations and Data Reduction	77
4.3 Data analysis	82
4.3.1 Detection and Categorization	82
4.3.2 Derivation of Velocities: Line Bisectors	86
4.3.3 Derivation of Magnetic Properties: Stokes Inversion . .	89

4.4	Convection in the Umbra	90
4.4.1	Morphology	90
4.4.2	Brightness vs Velocity	91
4.5	Umbral Dots	91
4.5.1	Case Studies	91
	Typical Central UD	93
	Distinct Central UD	94
	Typical Peripheral UD	95
	Typical Grain-Origin UDs	95
	UDs with Downflow Patches	97
4.5.2	Statistical Properties	98
4.5.3	Statistics of Bisector Velocities around UDs	98
4.5.4	Statistics of Magnetic Parameters around UDs	98
4.5.5	Typical Light Curve	102
4.5.6	Scatter Relations	105
4.6	Discussion and Conclusion	106
5	Summary and Concluding Remarks	125
5.1	Summary of Results	125
5.2	Open Issues	129
5.3	Concluding Remarks	130

1. Introduction

1.1. Introduction of Sunspots

1.1.1. Overview

Sunspots are one of the most prominent magnetic structures on the solar surface that appear dark in the white light images (Figure 1). They represent the surface manifestations of intense magnetic-field concentrations on the photosphere. A sunspot is composed of an umbra and a penumbra. The umbra is an extremely dark structure located in the center of the sunspot, whose brightness is about 0.3 times that of the quiet region. The penumbra is an aggregation of filamentary structures that encircles the umbra. The penumbra is slightly brighter than the umbra, about 0.7-0.8 times as bright as that of the quiet region. The presence of a penumbra distinguishes sunspots from pores. There are even sunspots without pores, so called orphan penumbra. The umbra is 1000–2500 K cooler than the quiet region, and the penumbra is 200–500 K cooler. This cool temperature is caused by the inhibition of convection through the magnetic field.

Typical sunspots show a bipolar magnetic structure. This fact leads to a model that sunspots are formed by the emergence of an embedded large magnetic flux tube through the solar surface from the convection layer (Zwaan 1985). The formation of a sunspot is observed as the coalescence of small pores. The time scale for the formation of a large sunspot is between a few hours and several days. Once the diameter of a pore exceeds roughly 3500 km, it usually starts to develop penumbral structure (Rucklidge et al. 1995). The penumbra develops surprisingly rapidly, being completed within an hour (e.g., Leka & Skumanich 1998). The decay of sunspots is associated with the presence of a moat flow and moving magnetic features; small magnetic elements flowing radially outward from sunspots. Recently Kubo et al. (2007) showed that the moving magnetic features alone can transport sufficient magnetic flux that are responsible for the decay a sunspot.

The size distribution of sunspots is broad, ranging from 3500–60000 km in diameter (Baumann & Solanki 2005). Smaller sunspots are more numerous. The size spectrum is characterized by a log-normal function, implying the associated magnetic flux tubes are the products of the fragmentation of a large flux tube (Abramenko & Longcope 2005). The lifetime of sunspots is between hours to months, which increases linearly as maximum size of the spot (Petrovay & van Driel-Gesztelyi 1997). The magnetic field strength of sunspots also tends to increase linearly as the size of the sunspot. The largest sunspots have field strength of 4000 G or more. The region with the strongest field within a sunspot is associated with the darkest part of the umbra. The outer edge of the penumbra possesses 700–1000 G field

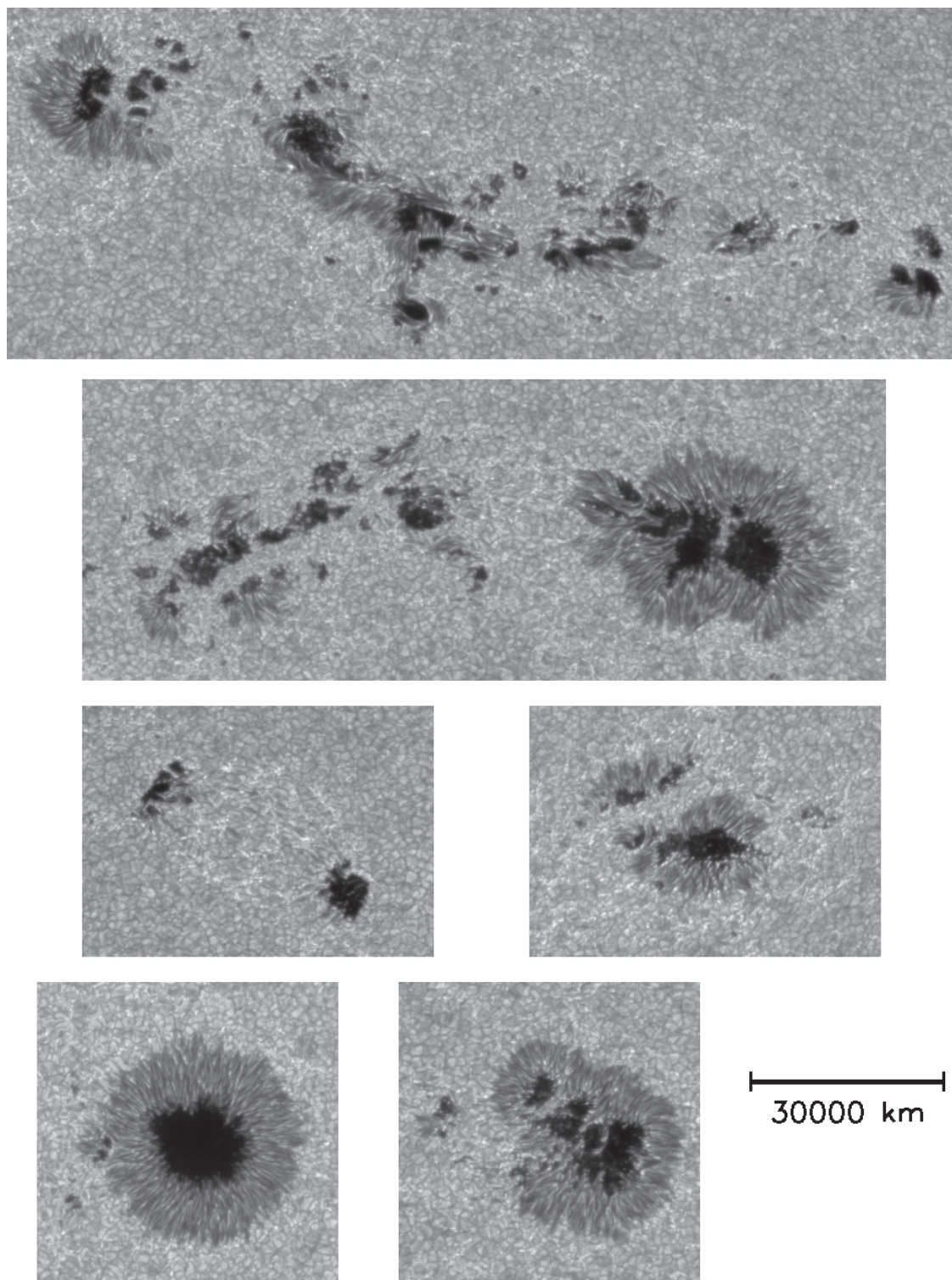


Fig. 1.— G-band sunspot images seen near the disk center (heliocentric angle $< 30^\circ$) observed by the *Hinode* Solar Optical Telescope during 2010.

strength (c.f., review in Solanki 2003).

1.1.2. History of Sunspot Observations

The existence of sunspots had been known at least since B.C. 400. In those days people watched sunspots by naked eyes at sunset or in the solar image through the leafy shade. The scientific observation of sunspots started from the time of Galileo. Galileo Galilei observed sunspots with his handmaid telescope in 1612, and published his first sunspot drawings in 1613 (Figure 2). In 1843, Samuel Heinrich Schwabe noticed that the number of sunspots show a periodic change with a period of about 11 years, which is known as the solar cycle. In 1904, Edward Walter Maunder found a rule in the distribution of sunspots. The appearance positions of the spots concentrates at mid-latitudes in the early phase of the cycle, and then move toward the equator as each cycle progresses. This is called “the butterfly diagram”, shown in Figure 4 (Ternullo 2007). It was George Ellery Hale and his collaborators who discovered magnetic field inside the sunspots in 1908 (Hale 1908). This marks the first detection of magnetic fields in the extraterrestrial field. Hale went on his observation on sunspots and derived what we call “the Hale’s polarity law” (Hale & Nicholson 1925): (1) The ordering of positive/negative polarity regions with respect to the east-west direction is the same in a given hemisphere throughout a given sunspot cycle; (2) The ordering of polarity is opposite across hemispheres throughout a cycle; (3) From one solar cycle to the next, the magnetic polarities of sunspot pairs undergo a reversal in each hemisphere (figure 3). Hale’s observations revealed that the solar cycle is a magnetic cycle with an average duration of 22 years.

Depending on these observational findings, Babcock (1961) constructed a model for the solar dynamics; (1) The start of the 22-year cycle begins with a well-established dipole field component aligned along the solar rotational axis. (2) The sun rotates at different velocity at different latitudes (differential rotation), and consequently after many rotations, the field lines become highly twisted and bundled. (3) The resulting buoyancy lifts the magnetic bundle to the solar surface, forming a bipolar field that appears as two spots. The leading spot of the bipolar field has the same polarity as the solar hemisphere, and the trailing spot is of opposite polarity. (4) The leading spot of the bipolar field tends to migrate towards the equator, while the trailing spot of opposite polarity migrates towards the solar pole of the respective hemisphere with a resultant reduction of the solar dipole moment. (5) This process of sunspot formation and migration continues until the solar dipole field reverses. This model is known as the Babcock model, and became a widely-accepted idea to date.

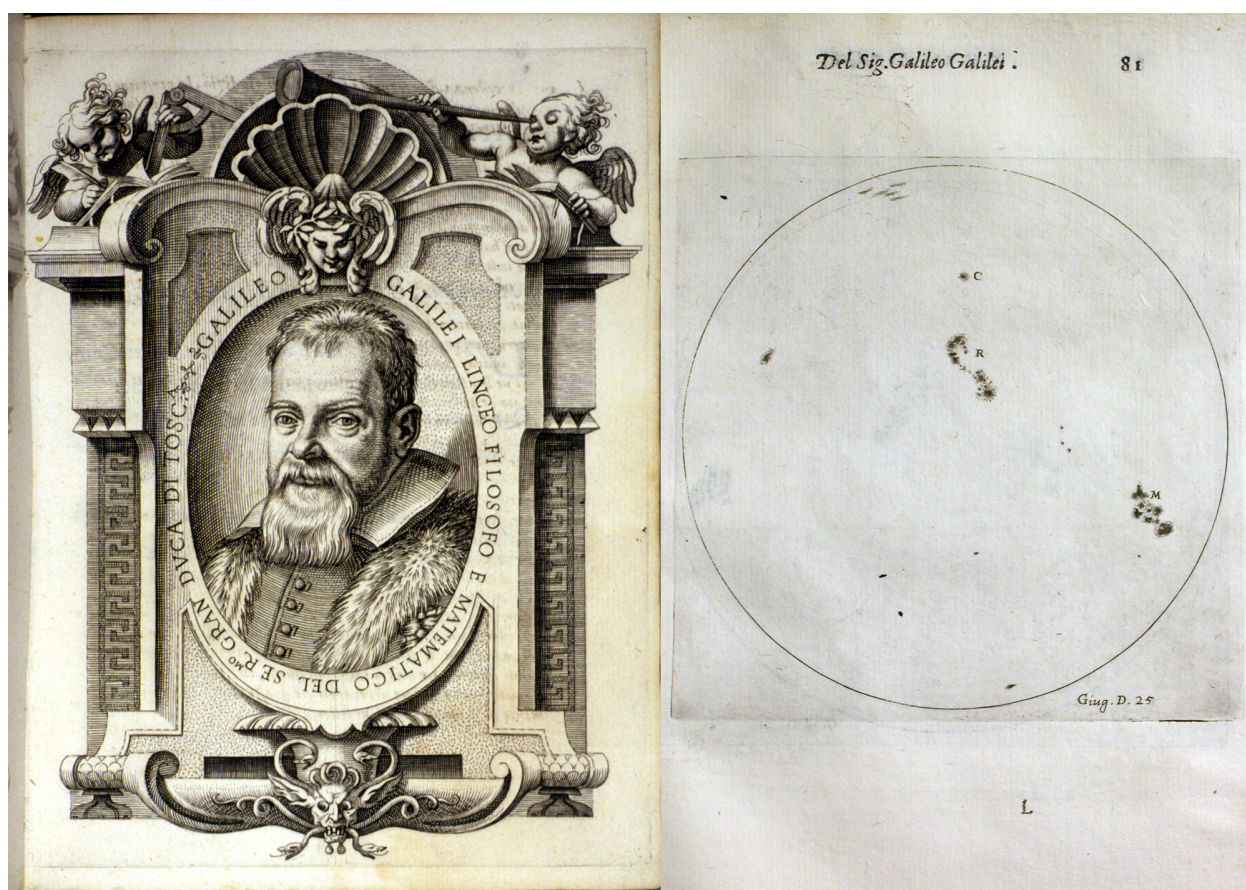


Fig. 2.— The title page and the drawing in “Letter on Sunspots” by Galileo Galilei published in 1613. Image copyright History of Science Collections, University of Oklahoma Libraries.

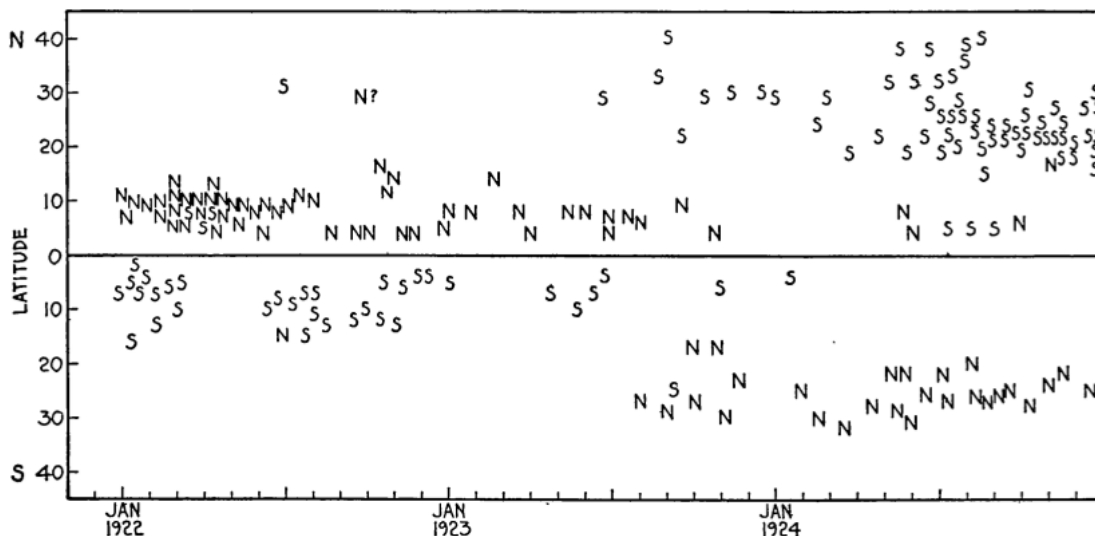


Fig. 3.— Heliocentric latitudes and magnetic polarities of sunspot groups. *N* (north-seeking) and *S* (south-seeking) represent the polarity of the preceding spot of each group. Cited from Figure 16 in Hale & Nicholson (1925).

1.1.3. Magnetic Field Structure and their Origin

The schematic illustration of sunspot's magnetic field is shown in Figure 5. The dark central umbra where the magnetic field is almost vertical, is encompassed by a filamentary penumbra. The penumbra exhibits a complicated interlocking-comb structure (Solanki & Montavon 1993; Title et al. 1993). The more horizontal flux tubes possess weaker fields than the inclined flux, and carry most of the hot plasma flow (known as the Evershed flow). The high-resolution polarimetric observations present evidence for some horizontal field lines that return back to the surface in the outer penumbra (Bellot Rubio et al. 2004; Ichimoto et al. 2007). By contrast, the inclined flux is essentially at rest, and does not return back to the solar surface. The field strength drops toward the sunspot's periphery, and becomes 700–1000 G with field inclination of 70° at the edge of the penumbra (Mathew et al. 2004; Balthasar & Collados 2005). The embedded radial outflow at the edge of a sunspot (Gizon et al. 2009; Thomas et al. 2002) is considered to be a maintenance process of this configuration.

The origin of the magnetic field inside is sitting in a hidden layer below the photosphere, where we cannot observe directly. The process of producing magnetic field in the solar interior is called the solar dynamo. Many people consider the solar dynamo is occurring at the tachocline, i.e., a region inside the Sun that exhibits the largest shear profile at the bottom of the convection zone (Ossendrijver 2003; Browning et al. 2006). At the tachocline, the electric current is produced by shear of the rotation motion and the magnetic field is

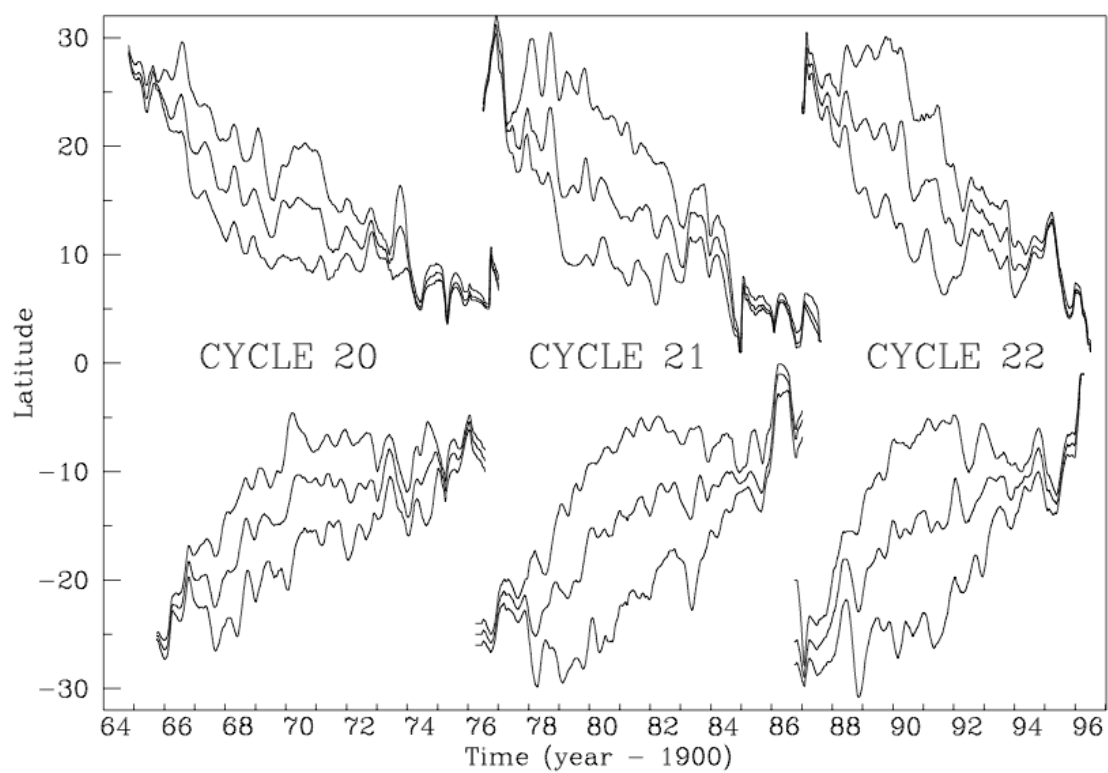


Fig. 4.— A sunspot butterfly diagram for solar cycles 20, 21, and 22. The spot zone boundaries and center of mass are shown by solid lines. Cited from Figure 4 in Ternullo (2007).

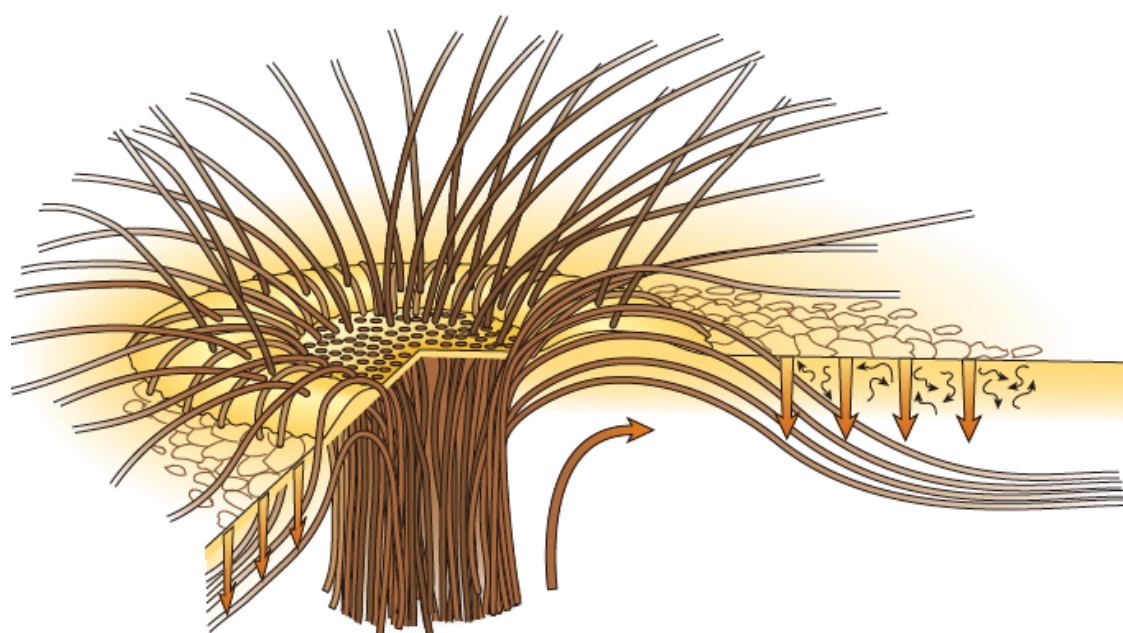


Fig. 5.— A sketch showing the structure of the magnetic field in a sunspot. The penumbral filaments are showing the interlocking-comb structure. Some of the flux tubes extending radially outward beyond the penumbra dive back below the surface, being held down by turbulent pumping due to granular convection (indicated by vertical arrows). Cited from Figure 1 in Thomas et al. (2002).

created. The process to carry the magnetic field from the tachocline to the photosphere is also a long-standing mystery, because the turbulent convective motion works to diffuse the magnetic field and the field should collapse before it reaches the photosphere. An important idea to solve this difficulty is the twist of the flux tubes. A number of theoretical studies (e.g., Archontis et al. 2004) show that the tubes must have a significant amount of twist in order to maintain their cohesiveness. Indeed some observations show that magnetic flux usually emerges at the surface in a significantly twisted state (Ishii et al. 1998; Fan 2009).

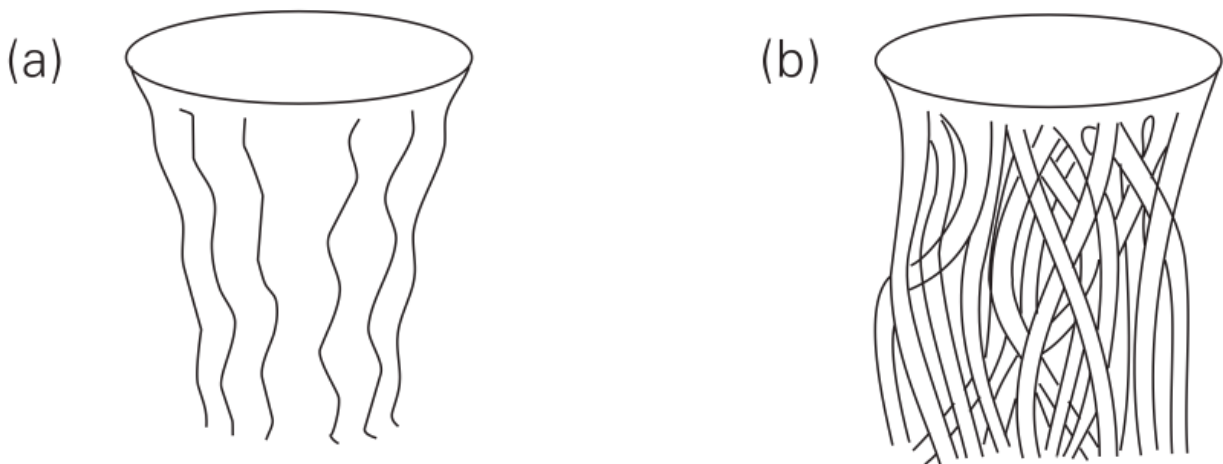


Fig. 6.— Sketches of the monolith (a) and cluster (b) models of the subsurface structure of sunspot magnetic fields. Cited from Thomas & Weiss (1992).

Because of the big uncertainty of the subsurface structure of sunspots, there is still an argument whether the basic magnetic field configuration of the sunspot is nonuniform (“cluster model”, Parker 1979) or uniform (“monolithic model”, Weiss et al. 2002) (Figure 6). The cluster model considers the basis structure of a sunspot as a cluster of isolated and unbound flux tubes. Their aggregation is supported by the downdrafts and vortex flows in the sublayers. On the other hand, the monolithic model suggests a sunspot as one large magnetic flux tube below the photosphere. Flows around flux tubes are driven by cooling of plasma, leading to downflows around the tube and hence inflows at the visible surface (Hurlburt & Rucklidge 2000). Surface observations have not given an answer to favor either of these models. By a helioseismology technique, Zhao et al. (2001) found powerful converging and downward directed flows beneath a sunspot at depths of 1.5-5 Mm, which may provide evidence for the downdrafts and vortex flows suggested by the cluster model.

1.1.4. Fine Scale Structures Inside Sunspots

Recent observations have revealed many small-scale structures in sunspots. The penumbra is made of numerous filamentary structures called “penumbral filaments”. “Light bridges”, which are bright slender structures running across the umbrae, are often observed within disintegrating sunspots. Bright tiny points, called “umbral dots”, are distributed almost all over the umbra without an exception. We will look into these individual phenomena in this section.

Penumbral filament

As illustrated in Figure 5, the penumbra is composed of thin filamentary flux tubes with horizontal and inclined magnetic inclinations. This is called the uncombed penumbra, or the interlocking comb structure of the penumbra. The typical width of the penumbral filaments is 150–250 km (Scharmer et al. 2002; Rouppe van der Voort et al. 2004). The bright penumbral filaments correspond to the filaments with inclined field inclination, whereas the dark penumbral filaments correspond to horizontal ones. The difference in inclination angle between the inclined and horizontal filaments lies between 30–40° (Langhans et al. 2005). The most characteristic and dynamic velocity field observed in the penumbra is the plasma flow outward from the umbra, i.e., the Evershed flow (Evershed 1909). The velocity of the Evershed flow reaches 6–7 km s⁻¹, which is only slightly smaller than the local sound speed in the photosphere. The Evershed flow is mainly concentrated in dark filaments where the field is weaker and nearly horizontal. The flow channels originate in bright, inner footpoints of 150–300 km with an upflow, and then turns into a horizontal outflow (Figure 7, Ichimoto et al. 2007). The brightness of these inner footpoints (called “penumbral grain”) exceeds that of the quiet Sun. The penumbral grain moves towards the center of the umbra at 0.5–1 km s⁻¹ (Rimmele & Marino 2006). Sometimes the tip of the penumbral grain separates from the filamentary structure and becomes a roundish bright point called a peripheral umbral dot (Section 1.4.3). Recent high resolution observation revealed the existence of dark lanes sitting in the middle of the penumbral filaments (Scharmer et al. 2002; Bellot Rubio et al. 2007), which is assumed to be a signature of sharp rise in the opacity.

Many theoretical models were proposed to account for the penumbral structure and associated velocity field (see review in Thomas & Weiss 2004), including the siphon flow model, the moving flux tube model, and the gappy penumbra model. The siphon flow model (Montesinos & Thomas 1998) is based on the flow driven by the difference in the gas pressure at the two footpoints of the flux tubes. In the moving flux tube model (Schlichenmaier 2002), a flux tube initially located at the magnetopause and becomes buoyant due to radiative heating. Radiative cooling at the surface produces pressure differences along the tube, and

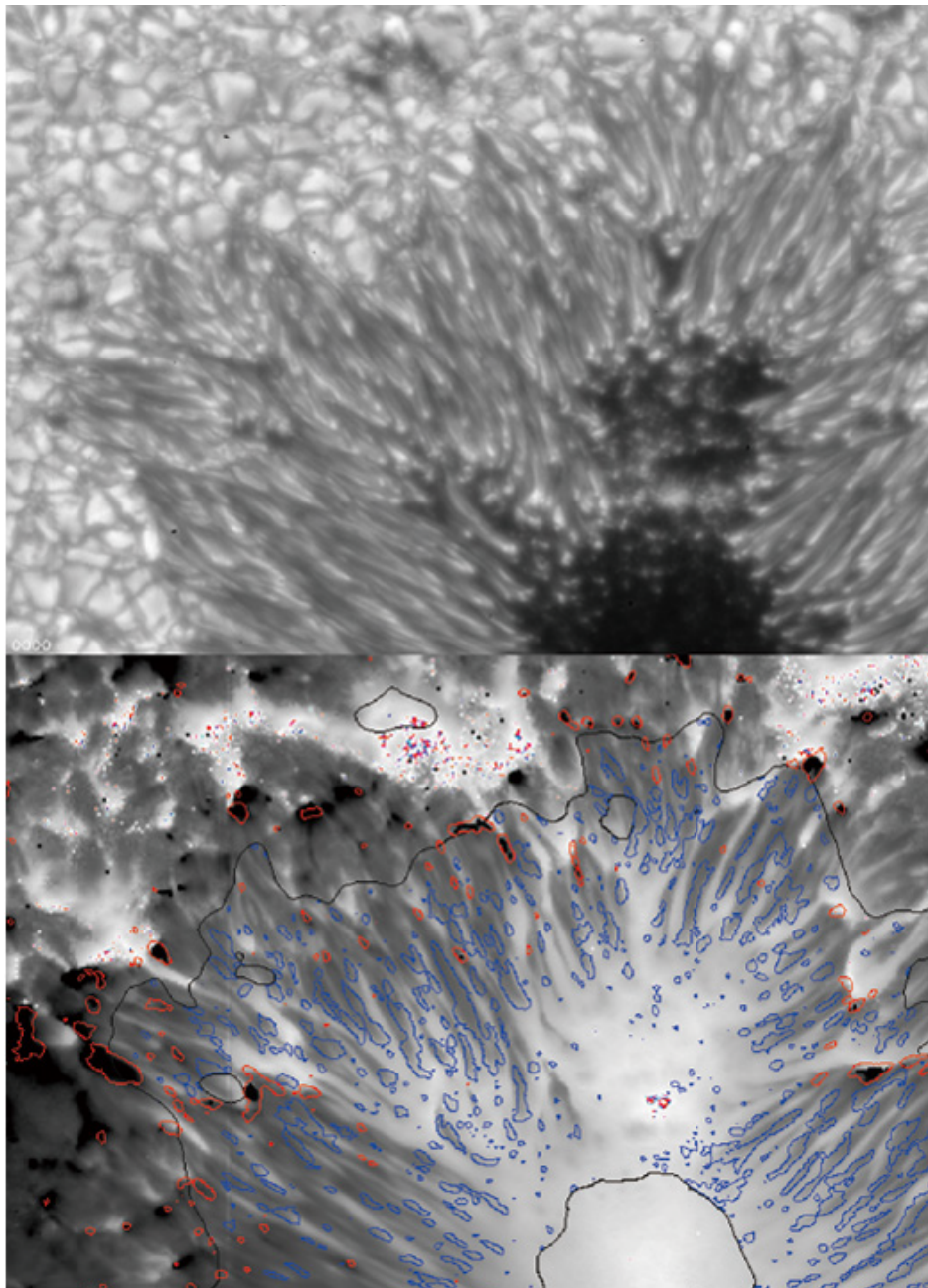


Fig. 7.— The continuum image (*top*) and the distribution of field inclination (*bottom*). In the bottom panel, dark color represents more horizontal fields and bright represents more vertical fields. Blue and red contours indicate the locations of upflow and downflow, respectively. Image courtesy to K. Ichimoto.

drives the outward-directed flow. The gappy penumbra model (Spruit & Scharmer 2006) appeared on the basis of the discovery of dark-cored penumbral filaments. It assumes that the penumbral filaments are due to convection in field-free, radially aligned gaps below the visible surface of the penumbra. The Evershed flow is located along horizontal magnetic field structures above the field-free gap, although the model allows the flow only over a finite distance.

Light bridge

Light bridges (LBs) have a shape like a bridge spanning the umbra with a width of only 300–1000 km. They are considered to have connections with the reestablishment of a granular surface leading to the decay of the sunspot (Vazquez 1973). According to their appearance, LBs are classified into two types; photospheric and penumbral types (Figure 8). The photospheric LBs (Muller 1979) are an aggregation of granules or umbral dots, while the penumbral LBs are the extension of the penumbral filaments (Sobotka et al. 1993). Bumba & Hejna (1980) found the relation between the two types of LBs in terms of the topology of the magnetic field. The photospheric LBs divide umbral cores of the same magnetic polarity, whereas penumbral LBs are formed along the boundary of opposite polarities.

Spectroscopic observations of LBs revealed a weaker and more horizontal magnetic field associated with an upflow within the LBs (Leka 1997). There is a positive correlation between the brightness and upflow velocities (Rimmele 1997). These studies suggest a scenario of the hot gas convection in LBs. Some observations indicate strong connections with penumbral filaments and umbral dots. The precursor of the LB formation is sometimes associated with the slow inward motion of umbral dots (Berger & Berdyugina 2003; Katsukawa et al. 2007). A narrow (<140 km) central dark lane running in the middle of the LB is found by recent high resolution observations (e.g., Rimmele 2008), like so in dark-cored penumbral filaments.

LBs are also important from the viewpoint of chromospheric activities. Shimizu et al. (2009) reported a LB produces chromospheric plasma ejections intermittently and recurrently for more than one day. There exists strong vertical electric current on the interface between the LB and pre-existing umbral field, causing the long-lasting chromospheric plasma ejections through the magnetic reconnection.

Umbral Dots

Umbral dots (UDs), the main target of our thesis, are tiny bright points in the umbra, and are observed in all of the sunspots and in pores (Sobotka et al. 1997a,b, 1999b). Their size is about 300 km and they live about 10 min. On average, UD are 500–1000 K cooler

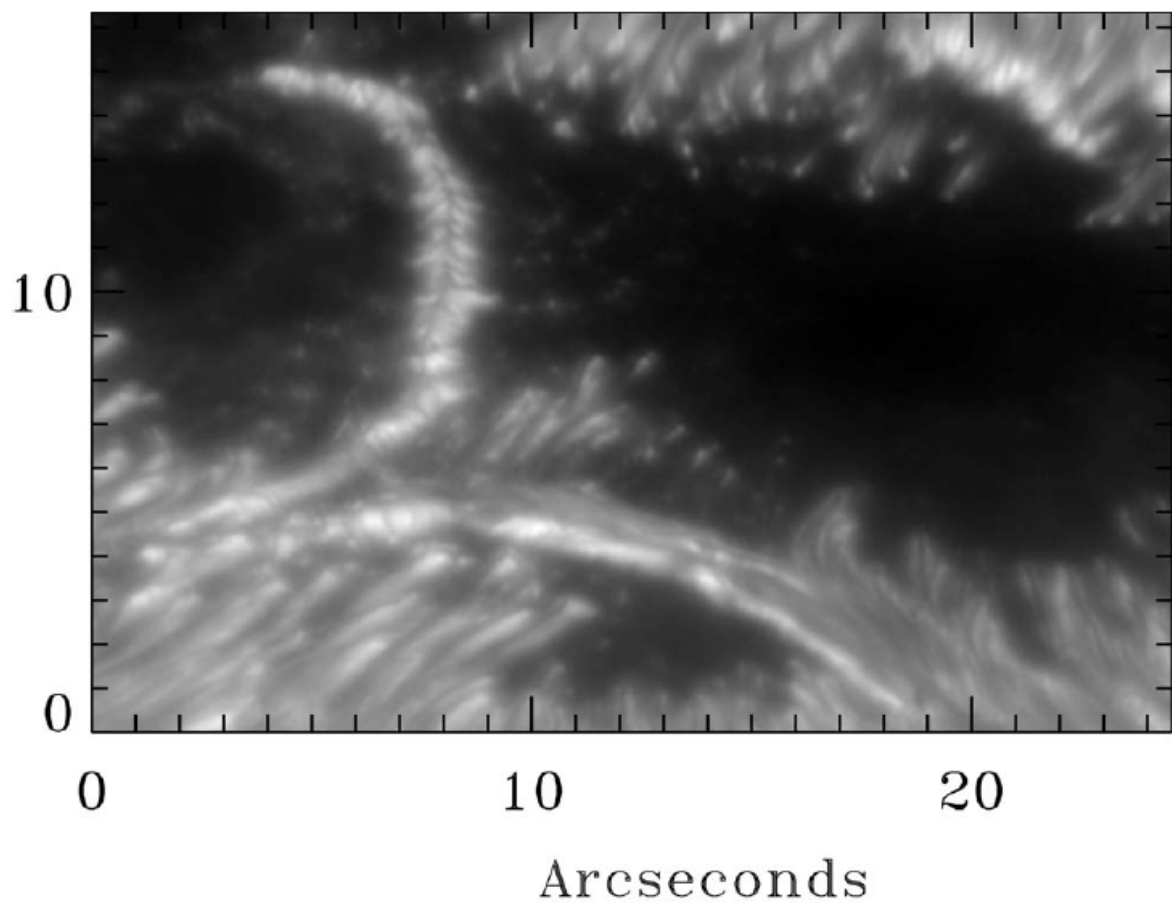


Fig. 8.— The continuum image showing the detail of the LBs within the largest umbra of NOAA 10036. The upper-left LB belongs to photospheric type, and the lower LB belongs to penumbral type. Cited from Figure 5 in Lites et al. (2004).

than the quiet region, but are about 1000 K hotter than the coolest part of the umbra (Kitai et al. 2007). This enhanced heat in UDs are supplied by the convective transport from the bottom layer, which contributes the total brightness of the umbra (Deinzer 1965).

The first observation of UDs was achieved by Chevalier (1916). Because of its small size and dynamic motion, it has been quite difficult to determine the statistical properties of lifetime, proper motion, and spectroscopic properties. The launch of the *Hinode* Solar Optical Telescope marks a new era of the research of UDs. First statistical study of UD's morphological properties was done by Kitai et al. (2007) using the *Hinode* continuum images. The fission and fusion events of UDs (Figure 9) were reported with seeing-free observations. Bharti et al. (2007b) found a hint of substructure within one UD using the *Hinode* G-band image. The velocity field and magnetic field of UDs has been studied using the high-precision *Hinode* spectropolarimeter. A number of literatures report negligible or small upflow in UDs (Watanabe et al. 2009b; Sobotka & Puschmann 2009), while strong upflow is found only in the deep layer of the photosphere in Riethmüller et al. (2008). UDs exhibit weaker magnetic field than the surrounding umbra, as well as more inclined magnetic field (Watanabe et al. 2009b; Sobotka & Puschmann 2009). These spectroscopic properties match well with the convective upwelling scenario of UDs. On the other hand, ground-based telescopes have an advantage in high resolution observation with their large apertures. The 1-m Swedish Solar Telescope discovered substructures within UDs, i.e., dark lanes and downflow patches at the edge of dark lanes (Ortiz et al. 2010). The width of smallest dark lanes is only 100 km, which is comparable to the diffraction limit of the largest telescope ever. The concentrated patches of downflow at their edges have sizes of about 180 km and velocities of up to 1 km s^{-1} .

As described in Section 1.3, there are two conflicting ideas about the sunspot substructure. The monolithic model considers UDs as the manifestations of overstable convection in a magnetic plasma (Knobloch & Weiss 1984). In the cluster model, UDs are interpreted as the thermal signature of field-free gas that is pushing magnetic field lines aside and penetrating from below into the photosphere (Parker 1979). Schüssler & Vögler (2006) presented realistic numerical simulations of umbral magnetoconvection using the framework of the monolithic model. Their model reproduced UDs as a natural result of convection in a strong, initially monolithic magnetic field. The convective energy transport is dominated by narrow upflow plumes with adjacent downflows, which become almost field-free near the surface layers. The simulated UDs correspond well to the observed features of umbral dots (systematic comparison between observation and simulation was done by Bharti et al. 2010), including their dark lanes and downflow patches (Rimmele 2008; Ortiz et al. 2010). Their simulation gives a strong support for the monolithic model as a driving process of UDs.

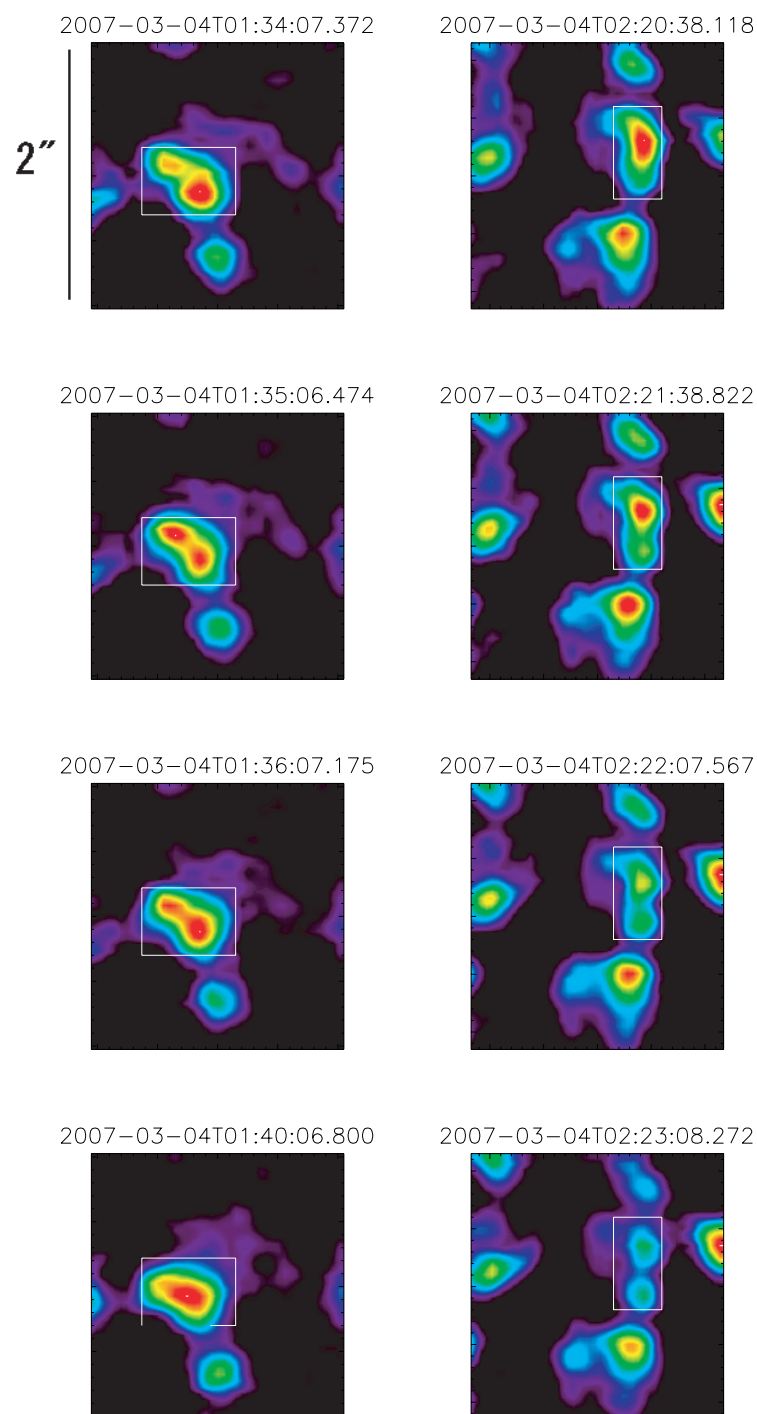


Fig. 9.— Temporal evolution of fission and fusion of UD's shown in pseudo-colors. The left column shows the fusion of two UD's, while the right column shows the fission of another UD. Cited from Figure 8 in Kitai et al. (2007).

1.2. Magnetoconvection

In recent years, the study of magnetoconvection, i.e., how magnetic fields make an effect on the convective process, in the solar interior has made significant advances. The advances greatly owe to the increasing computer power and its application to more physically established regimes and to more realistic geometry in numerical models. In this section I present the basic formula of magnetoconvection, and some recent realistic simulations of sunspot structures, referring mainly to the theoretical works by Weiss et al. (1990), Cattaneo et al. (2003), Vögler et al. (2005), and reviews by Hurlburt et al. (2000).

1.2.1. Equation of Magnetoconvection

The simulations of magnetoconvection in the solar interior are solved in a frame of a plane-parallel layer of gas with constant gravitational acceleration in the vertical (z) direction. This perfect monatomic gas has constant shear viscosity μ , magnetic permeability μ_0 , thermal conductivity K , electrical conductivity σ_c , heat capacities c_p and c_v , and ratio of specific heats $\gamma = \frac{5}{3}$. The influence of the Coriolis force is negligible for sunspot's fine structures as their dynamic timescales are much shorter than the Sun's rotation period. The stratification in the absence of motion is given by a polytrope, where temperature T , density ρ , and pressure P have the form

$$T = \Delta T z, \rho = \rho_0 (z/z_0)^m, P = [gd\rho_0/(m+1)]z^{m+1}/z_0^m \quad (1)$$

where $z_0 = T_0 d/\Delta T$ is the value of z at the upper boundary, ρ_0 is density at $z = z_0$, the polytropic index $m = (gd/\mathcal{R}T) - 1$, g is the gravitational acceleration, d is a depth of a layer, and \mathcal{R} is the gas constant.

The (kinetic) Prandtl number σ , the ratio of viscous diffusivity ν over thermal diffusivity κ , is constant but the diffusivity ratio ζ of the magnetic to the thermal diffusivity

$$\zeta = \frac{\eta}{\kappa} = \frac{c_p \rho}{\mu_0 \sigma_c K} = \zeta_0 \left(\frac{\rho}{\rho_0} \right) \quad (2)$$

is proportional to ρ . This diffusivity ratio ζ is the critical factor to determine the convection behavior. If $\zeta > 1$ the layer is filled with steady overturning convection, while if $\zeta < 1$ obtains oscillatory convection (Section 2.2).

The equations governing the magnetohydrodynamic system in terms of density ρ , velocity \mathbf{u} , and magnetic field \mathbf{B} are written as follows.

The continuity equation,

$$\frac{\partial \rho}{\partial t} = -\nabla \cdot (\rho \mathbf{u}) \quad (3)$$

The induction equation,

$$\frac{\partial \mathbf{B}}{\partial t} = \nabla \times (\mathbf{u} \times \mathbf{B}) + \zeta_0 \bar{K} \nabla^2 \mathbf{B} \quad (4)$$

The equation of motion,

$$\frac{\partial}{\partial t}(\rho \mathbf{u}) = -\nabla \cdot (\rho \mathbf{u} \mathbf{u} + F \mathbf{B} \mathbf{B}) - \nabla(P + \frac{1}{2}F|\mathbf{B}|^2) + (m+1)\hat{z} + \nabla \cdot \boldsymbol{\tau} \quad (5)$$

The energy equation,

$$\begin{aligned} \frac{\partial}{\partial t} \left[\rho \left(\frac{T}{\gamma-1} + \frac{1}{2}|\mathbf{u}|^2 - (m+1)z \right) + \frac{1}{2}F|\mathbf{B}|^2 \right] = \\ -\nabla \cdot \left[\rho \left(\frac{\gamma T}{(\gamma-1)} + \frac{1}{2}|\mathbf{u}|^2 - (m+1)z \right) \mathbf{u} + F \mathbf{B} \times (\mathbf{u} \times \mathbf{B}) - \zeta_0 \bar{K} \nabla \times \mathbf{B} - \bar{K} \nabla T + \mathbf{u} \cdot \boldsymbol{\tau} \right] \end{aligned} \quad (6)$$

Here the viscous stress tensor

$$\tau_{ij} = \sigma \bar{K} \left(\frac{\partial u_i}{\partial x_j} + \frac{\partial u_j}{\partial x_i} - \frac{2}{3} \delta_{ij} \frac{\partial u_k}{\partial x_k} \right), \quad (7)$$

dimensionless thermal conductivity

$$\bar{K} = \frac{K}{c_p \rho_0 d (\mathcal{R} \Delta T)^{1/2}}, \quad (8)$$

and the field strength is measured by the dimensionless quantity F .

$$F = \frac{B_0^2}{\mu_0 \mathcal{R} \rho_0 \Delta T} = \sigma \zeta_0 \bar{K}^2 Q \quad (9)$$

(Q is the Chandrasekhar number)

The corresponding β ratio of the gas pressure to the magnetic pressure is $\beta = 2z^{m+1}/(Fz^m)$. The superadiabatic gradient, or the strength of thermal buoyancy relative to dissipation, is measured by the Rayleigh number $R = (m+1)^2(\nabla - \nabla_{\text{ad}})(z^{2m+1}/(\sigma \bar{K}^2 z_0^{2m}))$. As the Rayleigh number increases, more turbulent convection occurs. The Chandrasekhar number Q is a measure of the imposed magnetic field, which can be expressed as $Q = B_z^2 \sigma_m / \sigma^2$. Here σ is the kinetic Prandtl number and $\sigma_m (= \nu/\eta)$ is the magnetic Prandtl number. The behavior of the system also depends on the horizontal scale of the perturbations.

1.2.2. Two Convection Modes : Overturning and Oscillatory

The critical Rayleigh number R_{crit} is determined for the onset of convection. In the absence of external magnetic fields, convection sets in as an overturning convection when R

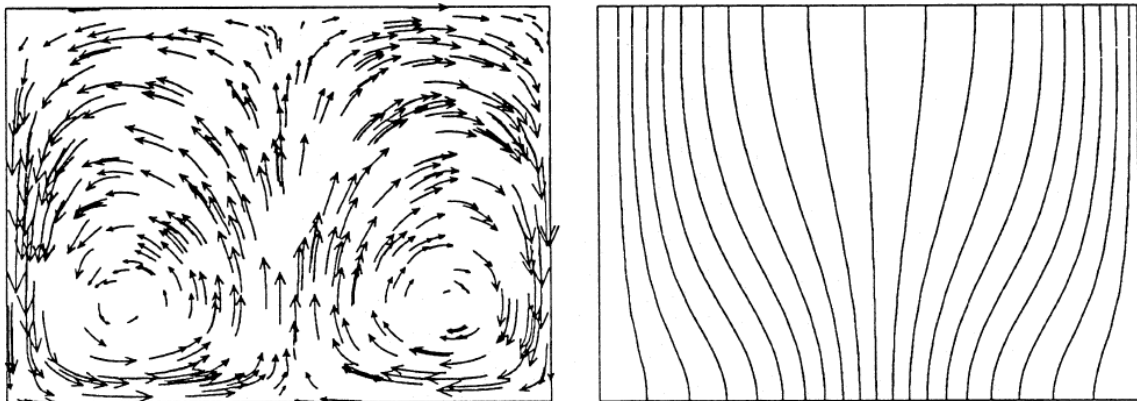


Fig. 10.— Steady overturning convection: streaklines (left) and field lines (right). Cited from Figure 4 in Weiss et al. (1990).

exceeds R_{crit} . The presence of an external magnetic field adds complexity to the problem and allows for the possibility of overstability. From linear analysis, it is derived that two convective modes exist, i.e., overturning and oscillatory convections, depending on the value of ζ , magnetic field strength, and horizontal scale of the perturbations. The critical condition of magnetic field strength and horizontal scale of the perturbations can be expressed in terms of the Chandrasekhar number.

If $\zeta \geq 1$, convection takes the form of an overturning convection (Figure 10) for all values of the magnetic field strength. If $\zeta < 1$, convection set in as an overturning convection if the imposed field is below the critical value, and as an oscillatory convection (Figure 11) if the imposed field exceeds the critical value. The critical value can be described in terms of the Chandrasekhar number,

$$Q_{\text{crit}} = \frac{k^4}{\pi^2} \frac{1 + \sigma}{\sigma_m - \sigma} \quad (10)$$

where k_h and k are the horizontal and total wavenumbers: $k_h^2 = k_x^2 + k_y^2$ and $k^2 = k_h^2 + \pi^2$. At a fixed value of the Rayleigh number, the bifurcations of overturning ($Q^{(e)}$) and oscillatory ($Q^{(o)}$) are expressed as follows.

$$Q^{(e)} = \frac{k_h^2 R - k^6}{\pi^2 k^2} \quad (11)$$

$$Q^{(o)} = \frac{1 + \sigma}{\pi^2 \sigma^2} \left[\frac{\sigma_m^2 k_h^2 R}{(1 + \sigma_m) k^2} - (\sigma + \sigma_m) k^4 \right] \quad (12)$$

An oscillatory bifurcation appears provided that

$$\frac{(k_h^2 + \pi^2)^3}{k_h^2} < \frac{\sigma_m - \sigma}{1 + \sigma_m} R. \quad (13)$$

In linear analysis, the preferred horizontal scale of convection decreases with increasing field strength, i.e., narrower convective cells are formed for stronger fields.

1.2.3. Simulation of Magnetoconvection in a Sunspot Umbra

In the umbra, we must enter the non-linear regime because of the rapid rise in ζ as height. For a model umbra with a magnetic field of 3000 G (Meyer et al. 1974; Maltby et al. 1986), $\zeta = 0.003$ at $z = 0$ km (photosphere) but $\zeta = 32$ at $z = 4000$ km depth. Oscillatory convection is the preferred mode in the first few thousand km depth below the umbral photosphere, but overturning convection is preferred in much deeper layer. Thus it is necessary to consider the non-linear magnetoconvection in an atmosphere with $\zeta < 1$ at the top but $\zeta > 1$ at the bottom. The magnetic field in the umbra is relatively uniform and vertical. Therefore models using simple, uniformly vertical field configuration can describe the physics in the umbra. The computer simulations with vertical field model in three dimension are performed by Vögler et al. (2005) and Schüssler & Vögler (2006). Here I present their results, and present many similarities with observations.

Their numerical model is like this. The computational box includes $5760 \text{ km} \times 5760 \text{ km}$ in the horizontal directions and 1600 km in depth (1200 km below and 400 km above optical depth $\tau=1$). The computational mesh size is 20 km in horizontal and 10 km in vertical direction. The imposed vertical magnetic flux is fixed, corresponding to averaged vertical field strength of 2500 G. The thermal energy density of the inflowing matter at the bottom boundary is fixed at a rate of $3.5 \times 10^{12} \text{ ergs cm}^{-3}$, leading to an average radiative energy output through the upper boundary around 17–18% of its value outside sunspots.

The snapshot of the simulation result is shown in Figure 12. The upwelling convective plumes start off like oscillatory convection columns below the surface but turn into narrow overturning cells driven by the strong radiative cooling, becoming almost field-free near the surface layers. The bright features in the intensity image have a typical size of 200–300 km, a lifetime on the order of 30 min, and a broad distribution of brightness. These values are consistent with the parameters of observed UDs (Bharti et al. 2010). Most of the simulated UDs have an elongated shape, a central dark lane, and downflows concentrated at the endpoints of the dark lanes. The magnetic field is strongly reduced in the near-surface layer, leading to the elongated shape of UDs. The upflow is strongly braked near the surface where the plasma rapidly loses its buoyancy due to radiative cooling. The plasma piles up and the flow turns horizontal in the direction of the dark lane, finally descending in narrow downflow channels at their endpoints.

A new and interesting feature predicted in the simulation is a narrow jetlike upflow above an UD. The pressure build-up drives matter out along the magnetic field with a velocity of 1 km s^{-1} . This could explain the chromospheric dynamics and heating above the sunspot. The observation detection of this upward injection from UDs has not achieved yet.

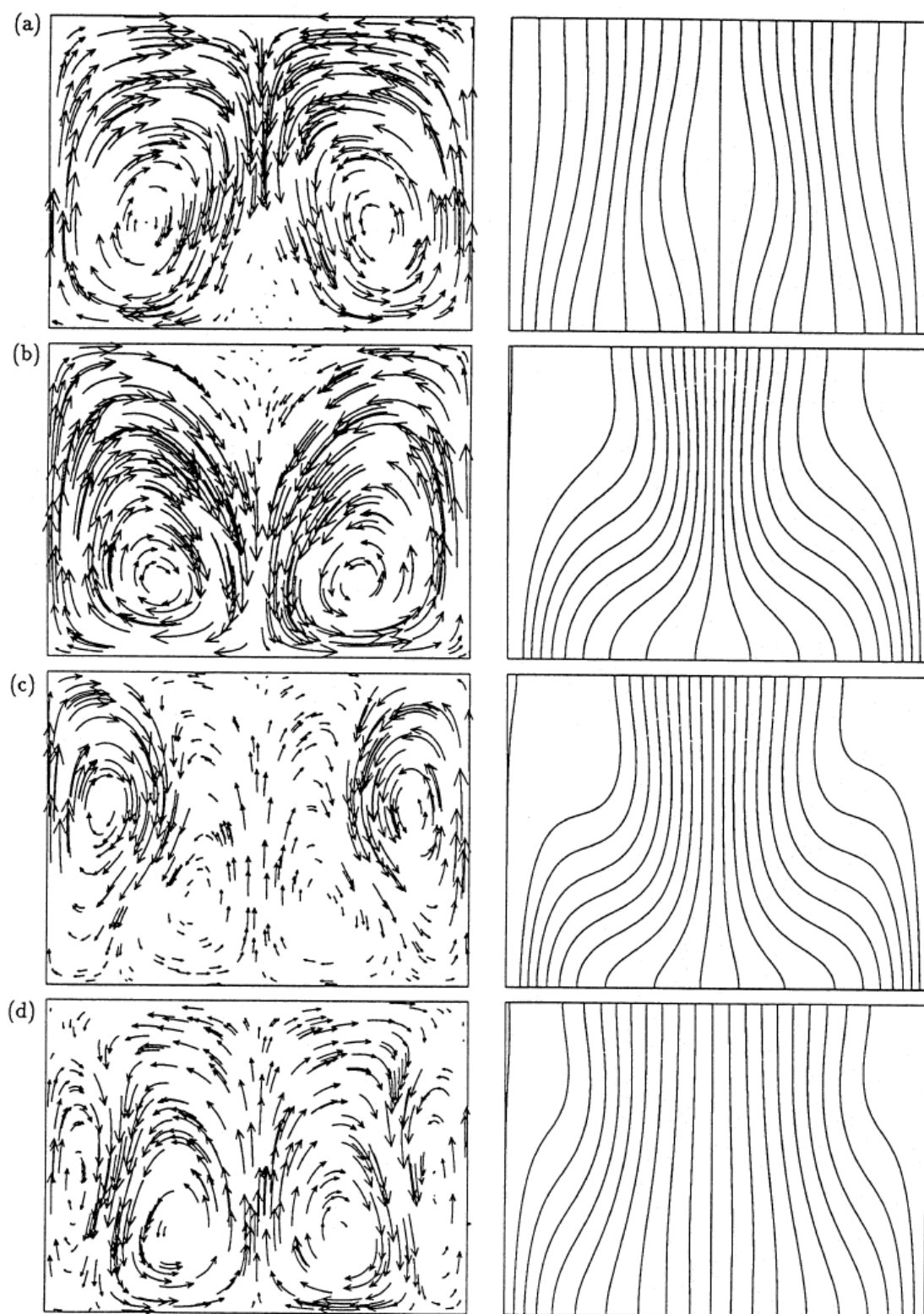


Fig. 11.— Oscillatory convection: streaklines (left) and field lines (right). The time proceeds from (a) to (d). Cited from Figure 6 in Weiss et al. (1990).

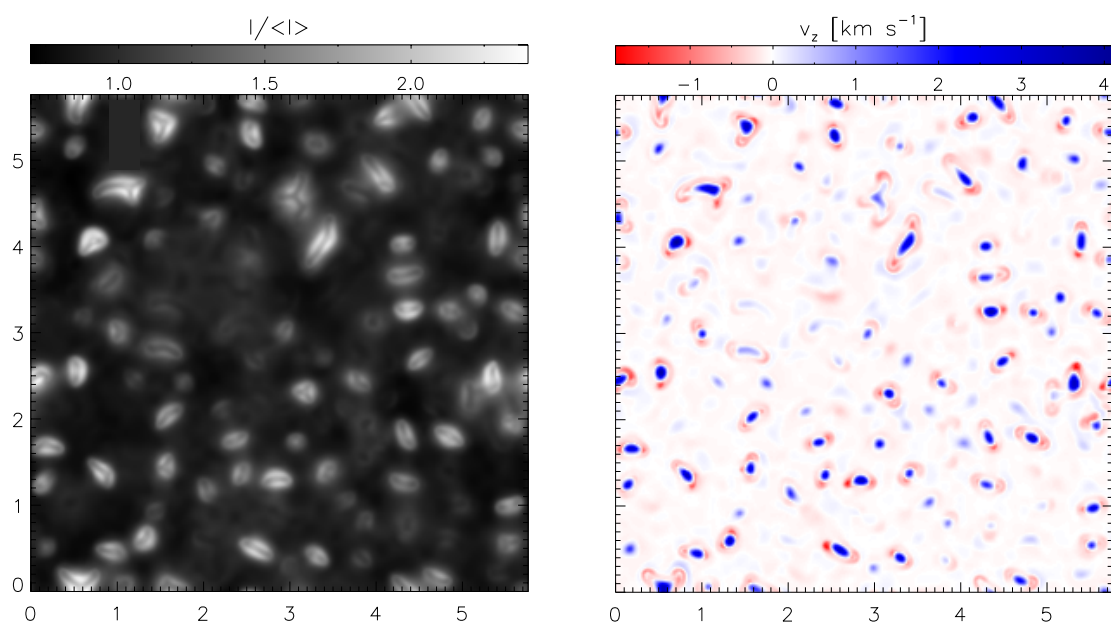


Fig. 12.— Vertically emerging grey intensity, normalized by its horizontal average (left) and cuts of the vertical velocity (right, blue means upflow and red means downflow) at a height of 1200 km above the bottom of the simulation box. The length unit is Mm. Adapted from Figure 1 in Schüssler & Vögler (2006).

1.3. Motivations of Studying Umbral Dots

1.3.1. The Importance and Difficulty of Studying Umbral Dots

Magnetic activity is exhibited by not only in the Sun, but also in the late-type stars with deep convective envelopes, accretion disks, neutron stars, and so on. However, the Sun is the unique existence whose surface manifestations can be directly observed down to tiny scales. From this viewpoint, the Sun is often referred as “the laboratory of plasma physics”. Likewise, umbral dots (UDs), small bright points distributed in the sunspot umbra, are so to say “the laboratory of magnetoconvection”. UD provide the best situation for studying the magnetoconvective phenomena in both observational and theoretical ways. We are at the stage of achieving down to $0.1''$ (corresponds to 70 km on the solar surface) spatial resolution (c.f., *Hinode* satellite, Swedish 1-m Solar Telescope, 1.6-m New Solar Telescope). Moreover, the Sun emits enormous luminosity, which is 3.8×10^{33} erg s⁻¹. These favorable situations allow us to observe UD with an enough spatial and temporal resolution. The theoretical study of umbral magnetoconvection is relatively simple, because the field configuration of the umbra can be considered as uniform and vertical. Indeed, the three dimensional MHD simulation assuming uniform vertical magnetic field by Schüssler & Vögler (2006) succeeded in reproducing the basic properties of UD. As a next step, the extension to other magnetoconvective phenomena (penumbral grains, light bridges, penumbral filaments) is being studied in the same framework but with more realistic field configurations (Heinemann et al. 2007; Rempel et al. 2009).

Recent UD observations entered a new phase that the realistic computer simulations give a stimulating predictions and observations check the validity of their predictions. The central dark lanes within bright structures, created by the pile-up of plasma raising the equal optical depth layer, was first observed in the penumbral filaments (Scharmer et al. 2002; Spruit & Scharmer 2006) and later in the light bridge (Rimmele 2008; Rouppe van der Voort et al. 2010). The finding of central dark lanes within UD comes in last because of its small size and faint transience. Ortiz et al. (2010) reported that the width of the dark lanes is of the order of $0.1''$, and they keep their identity for only a few minutes. Ortiz et al. (2010) also discovered the downflow patches at the endpoints of the central dark lanes. Near the surface the convective gas constituting UD receives radiative cooling and moves in the direction of the dark lane, until the gas returns to deeper layer along narrow channels. This returning of the convective flow corresponds to downflow patches at the endpoints of the dark lanes. The observed downflow patches have typical size of $0.25''$ and velocities up to 1 km s^{-1} , and possess enhanced net circular polarization signals.

Although many observational discoveries were achieved, there still remain unsolved topics. One of them is the observational counterpart of the narrow upward ejecting plumes

above the photospheric surface of UDs predicted by Schüssler & Vögler (2006). The existence of upward ejecting plumes above UDs may explain the contribution to the umbral brightness and the chromospheric heating. Although UDs cover only 3–10% of the umbral area, they contribute 10–20% of the umbral brightness. The process how UDs contribute to the umbral brightness is not totally understood. In the chromospheric umbra, chromospheric UDs and oscillating signature called umbral flashes are observed, but their counterpart in the photosphere is unknown. The UD is one of the promising candidates of their counterparts. Another remaining topics is the temporal evolution of spectropolarimetric properties. While the thorough researches on the photometric temporal evolution are available (Riethmüller et al. 2008b), the temporal evolution of spectropolarimetric properties, i.e., line-of-sight velocity and magnetic field of UDs, is rarely performed. This is because the spectropolarimetric observation optimized for UDs is highly challenging. The standard methods of spectropolarimetric observation, the slit spectrograph and the imaging spectrograph, have merits and demerits. The slit spectrograph can take the line profile in a high spectral resolution, but it needs time to scan the field. Sobotka & Jurčák (2009) used the *Hinode* slit spectrographic data, which scans 8'' width region with 333 s temporal cadence. The 333 s temporal cadence is too coarse to describe 10 min lifetime of UDs. The imaging spectrograph is able to cover a large area, but the spectral resolution has to be reduced in order to save the time for spectral scanning. The observation used in Ortiz et al. (2010) took 26 s to scan the Fe I 630.15 and 630.25 nm lines in wavelength steps of 4.8 pm. Not simultaneous acquisition of the spectral profile and the coarse spectral resolution may partly smear out the dynamic of UDs. We have to choose appropriate observation method depending on our purposes.

Another important motivation of UD studies lies in the clarification of the sunspot subsurface structure. There are two prevailing models of the sunspot structures: the monolithic and the cluster model (Knobloch & Weiss 1984; Parker 1979). The monolithic model considers UDs as the manifestation of magnetoconvection in a uniform magnetic field, while the cluster model interprets UDs as the thermal signature of field-free gas that is penetrating from subsurface layer. A detailed comparison between models and observations have the possibility to give us the ultimate understanding of the sunspot structure. In this sense, UDs are the unique observation target to extract the subsurface information, apart from the helioseismology techniques (Moradi et al. 2010).

1.3.2. The Contents of this Thesis

The author has two objectives about studying the UDs. First objective is to derive the spectropolarimetric properties of UDs and their temporal evolution in a statistical way. At present, only a few literature report the temporal evolution of UDs, but with either insufficient temporal cadence or unreliable statistics. The excellent datasets taken at the

Dunn Solar Telescope and the Swedish 1-m Solar Telescope motivate the author to address this topic. Second objective is to investigate the subsurface structure of a sunspot based on the convective properties of UDs. This work could be done by improving the validity of numerical simulations to match the real sunspot phenomena. Thus we performed analysis of UD's physical parameters (size, lifetime, temporal evolution, ...) dependency on their birthplace magnetic field. This is, so to say, a parameter survey of magnetoconvection, because the simulation creates different size of UDs by changing its input magnetic field. This is the only way to solve the subsurface structure by the surface observation.

We utilized different instruments offering different advantages, depending on the purpose of the research. As the Dunn Solar Telescope is capable of taking spectroscopic information at relatively high cadence in many kinds of spectral lines, we performed the temporal evolution of UD's velocity field (Section 4). The spectropolarimeter onboard *Hinode* has the superb polarimetric sensitivity and free from atmospheric disturbances, enabling the dependency study of UDs on their magnetic structure (Section 5). The Swedish 1-m Solar Telescope is the largest aperture telescope by the time that the New Solar Telescope has started operation in 2011, thus is appropriate for high spatial resolution observation. Combined with high temporal polarimetric observation by the CRISP spectropolarimeter, the temporal evolution of magnetic field around UDs are studied (Section 6).

UD's analysis is a challenge against high spatial resolution and high temporal cadence combined with a stable seeing condition. The observational data the author uses are surely the best in recent years. Plus, the careful data calibration and the sufficient statistics derive some new common kinetic properties of UDs, although the change caused by UDs is so small. The derived properties are in good agreements with the recent MHD simulations based on magnetoconvection in a uniform magnetic field, but some results poses inconsistencies. These inconsistencies will help improving the assumed sunspot modeling, and hopefully lead to the ultimate understanding of sunspots.

The brief summary of the results and open issues are described in Section 7.1 and 7.2. Finally the author concludes the thesis with some remarks (Section 7.3).

REFERENCES

- Abramenko, V. I., & Longcope, D. W. 2005, *ApJ*, 619, 1160
- Archontis, V., Moreno-Insertis, F., Galsgaard, K., Hood, A., & O'Shea, E. 2004, *A&A*, 426, 1047
- Babcock, H. W. 1961, *ApJ*, 133, 572
- Baumann, I., & Solanki, S. K. 2005, *A&A*, 443, 1061
- Balthasar, H., & Collados, M. 2005, *A&A*, 429, 705
- Bellot Rubio, L. R., Balthasar, H., & Collados, M. 2004, *A&A*, 427, 319
- Bellot Rubio, L. R., et al. 2007, *ApJ*, 668, L91
- Berger, T. E., & Berdyugina, S. V. 2003, *ApJ*, 589, L117
- Bharti, L., Joshi, C., & Jaaffrey, S. N. A. 2007, *ApJ*, 669, L57
- Bharti, L., Beeck, B., & Schüssler, M. 2010, *A&A*, 510, A12
- Browning, M. K., Miesch, M. S., Brun, A. S., & Toomre, J. 2006, *ApJ*, 648, L157
- Bumba, V., & Hejna, L. 1980, *Bulletin of the Astronomical Institutes of Czechoslovakia*, 31, 257
- Cameron, R., Schüssler, M., Vögler, A., & Zakharov, V. 2007, *A&A*, 474, 261
- Cattaneo, F., Emonet, T., & Weiss, N. 2003, *ApJ*, 588, 1183
- Chevalier, S., 1916, *Ann. Obs. Astron, Zo-Sè*, 9, B1
- Deinzer, W. 1965, *ApJ*, 141, 548
- Evershed, J. 1909, *MNRAS*, 69, 454
- Fan, Y. 2009, *ApJ*, 697, 1529
- Gizon, L., et al. 2009, *Space Sci. Rev.*, 144, 249
- Hale, G. E. 1908, *ApJ*, 28, 315
- Hale, G. E., & Nicholson, S. B. 1925, *ApJ*, 62, 270
- Heinemann, T., Nordlund, Å., Scharmer, G. B., & Spruit, H. C. 2007, *ApJ*, 669, 1390

- Hurlburt, N. E., Matthews, P. C., & Rucklidge, A. M. 2000, *Sol. Phys.*, 192, 109
- Hurlburt, N. E., & Rucklidge, A. M. 2000, *MNRAS*, 314, 793
- Ichimoto, K., et al. 2007, *PASJ*, 59, 593
- Ishii, T. T., Kurokawa, H., & Takeuchi, T. T. 1998, *ApJ*, 499, 898 & Tokumaru, M. 2009, *Journal of Geophysical Research (Space Physics)*, 114, 10102
- Katsukawa, Y., et al. 2007, *PASJ*, 59, 577
- Kitai, R., et al. 2007, *PASJ*, 59, 585
- Knobloch, E., & Weiss, N. O. 1984, *MNRAS*, 207, 203
- Kubo, M., Shimizu, T., & Tsuneta, S. 2007, *ApJ*, 659, 812
- Langhans, K., Scharmer, G. B., Kiselman, D., Löfdahl, M. G., & Berger, T. E. 2005, *A&A*, 436, 1087
- Leka, K. D. 1997, *ApJ*, 484, 900
- Leka, K. D., & Skumanich, A. 1998, *ApJ*, 507, 454
- Lites, B. W., Scharmer, G. B., Berger, T. E., & Title, A. M. 2004, *Sol. Phys.*, 221, 65
- Maltby, P., Avrett, E. H., Carlsson, M., Kjeldseth-Moe, O., Kurucz, R. L., & Loeser, R. 1986, *ApJ*, 306, 284
- Mathew, S. K., Solanki, S. K., Lagg, A., Collados, M., Borrero, J. M., & Berdyugina, S. 2004, *A&A*, 422, 693
- Meyer, F., Schmidt, H. U., Wilson, P. R., & Weiss, N. O. 1974, *MNRAS*, 169, 35
- Montesinos, B., & Thomas, J. H. 1998, *Ap&SS*, 263, 323
- Moradi, H., et al. 2010, *Sol. Phys.*, 267, 1
- Muller, R. 1979, *Sol. Phys.*, 61, 297
- Ossendrijver, M. 2003, *A&A Rev.*, 11, 287
- Ortiz, A., Bellot Rubio, L. R., & Rouppe van der Voort, L. 2010, *ApJ*, 713, 1282
- Parker, E. N. 1979, *ApJ*, 230, 905
- Petrovay, K., & van Driel-Gesztelyi, L. 1997, *Sol. Phys.*, 176, 249

- Rempel, M., Schüssler, M., & Knölker, M. 2009, *ApJ*, 691, 640
- Riethmüller, T. L., Solanki, S. K., & Lagg, A. 2008a, *ApJ*, 678, L157
- Riethmüller, T. L., Solanki, S. K., Zakharov, V., & Gandorfer, A. 2008b, *A&A*, 492, 233
- Rimmele, T. R. 1997, *ApJ*, 490, 458
- Rimmele, T., & Marino, J. 2006, *ApJ*, 646, 593
- Rimmele, T. 2008, *ApJ*, 672, 684 *Sol. Phys.*, 198, 5
- Roupe van der Voort, L. H. M., Löfdahl, M. G., Kiselman, D., & Scharmer, G. B. 2004, *A&A*, 414, 717
- Roupe van der Voort, L., Bellot Rubio, L. R., & Ortiz, A. 2010, *ApJ*, 718, L78
- Rucklidge, A. M., Schmidt, H. U., & Weiss, N. O. 1995, *MNRAS*, 273, 491
- Scharmer, G. B., Gudiksen, B. V., Kiselman, D., Löfdahl, M. G., & Roupe van der Voort, L. H. M. 2002, *Nature*, 420, 151
- Schlichenmaier, R. 2002, *Astronomische Nachrichten*, 323, 303
- Schüssler, M., Vögler, A. 2006, *ApJ*, 641, L73
- Shimizu, T., et al. 2009, *ApJ*, 696, L66
- Sobotka, M., Bonet, J. A., & Vazquez, M. 1993, *ApJ*, 415, 832
- Sobotka, M., Brandt, P. N., & Simon, G. W. 1997a, *A&A*, 328, 682
- Sobotka, M., Brandt, P. N., & Simon, G. W. 1997b, *A&A*, 328, 689
- Sobotka, M., Vázquez, M., Bonet, J. A., Hanslmeier, A., & Hirzberger, J. 1999, *ApJ*, 511, 436
- Sobotka, M., & Jurčák, J. 2009, *ApJ*, 694, 1080
- Sobotka, M., & Puschmann, K. G. 2009, *A&A*, 504, 575
- Solanki, S. K. 2003, *A&A Rev.*, 11, 153
- Solanki, S. K., & Montavon, C. A. P. 1993, *A&A*, 275, 283
- Spruit, H. C., & Scharmer, G. B. 2006, *A&A*, 447, 343

- Ternullo, M. 2007, *Sol. Phys.*, 240, 153
- Thomas, J. H., & Weiss, N. O. 1992, *NATO ASIC Proc. 375: Sunspots. Theory and Observations*,
- Thomas, J. H., Weiss, N. O., Tobias, S. M., & Brummell, N. H. 2002, *Nature*, 420, 390
- Thomas, J. H., & Weiss, N. O. 2004, *ARA&A*, 42, 517
- Title, A. M., Frank, Z. A., Shine, R. A., Tarbell, T. D., Topka, K. P., Scharmer, G., & Schmidt, W. 1993, *ApJ*, 403, 780
- Vazquez, M. 1973, *Sol. Phys.*, 31, 377
- Vögler, A., Shelyag, S., Schüssler, M., Cattaneo, F., Emonet, T., & Linde, T. 2005, *A&A*, 429, 335
- Watanabe, H., Kitai, R., Ichimoto, K., & Katsukawa, Y. 2009, *PASJ*, 61, 193
- Weiss, N. O., Brownjohn, D. P., Hurlburt, N. E., & Proctor, M. R. E. 1990, *MNRAS*, 245, 434
- Weiss, N. O., Proctor, M. R. E., & Brownjohn, D. P. 2002, *MNRAS*, 337, 293
- Zhao, J., Kosovichev, A. G., & Duvall, T. L., Jr. 2001, *ApJ*, 557, 384
- Zwaan, C. 1985, *Sol. Phys.*, 100, 397
-

2. Temporal Evolution of a Rapidly-Moving Umbral Dot

Abstract

We performed two-dimensional spectroscopic observations of the preceding sunspot of NOAA 10905 located off disk center ($S8^\circ E36^\circ$, $\mu \approx 0.81$) by using the Interferometric BI-dimensional Spectrometer (IBIS) operated at the Dunn Solar Telescope (DST) of the National Solar Observatory, New Mexico. The magnetically insensitive Fe I line at 709.04 nm was scanned in wavelength repetitively at an interval of 37 s to calculate sequences of maps of the line-wing and line-core intensity, and the line-of-sight Doppler velocity at different line depths (3% to 80%). Visual inspection of movies based on speckle reconstructions computed from simultaneous broadband data and the local continuum intensity at 709.04 nm revealed an umbral dot (UD) intruding rapidly from the umbral boundary to the center of the umbra. The apparent motion of this object was particularly fast (1.3 km s^{-1}) when compared to typical UD. The lifetime and size of the UD was 8.7 min and 240 km, respectively. The rapid UD was visible even in the line-core intensity map of Fe I 709.04 nm and was accompanied by a persistent blueshift of about 0.06 km s^{-1} .

2.1. Introduction

Umbral dots (UDs) are numerous bright points observed almost all over the umbra. The size and lifetime of UD have been studied by many authors such as Kitai *et al.* (2007), Riethmüller *et al.* (2008), and Rimmele (2008). They found consistent values for sizes and lifetimes of $0.2''$ - $0.5''$ and ≈ 15 min, respectively. UD are usually classified into two subclasses; central UD and peripheral UD. The peripheral UD have higher temperature than central UD (Grossmann-Doerth, Schmidt, and Schroeter 1986), and are distributed at the periphery of the umbra. The central UD are almost static, while the peripheral UD move toward the center of the umbra with speeds less than 1.0 km s^{-1} (Sobotka, Brandt, and Simon 1997). The importance of UD with respect to the energy transport inside sunspot umbrae is reviewed in Solanki (2003).

In order to extract information about the thermodynamic structure of the solar at-

mosphere in and around UDs, high resolution spectroscopy and spectro-polarimetry play a crucial role. From spectroscopic observations, Rimmele (2004) find strong upflows of the order of 1 km s^{-1} in the deep photosphere of UDs. Riethmüller, Solanki, and Lagg (2008) performed an inversion of the Stokes profiles recorded by the *Hinode* Solar Optical Telescope (Tsuneta *et al.* 2008; Ichimoto *et al.* 2008) and found no difference between UDs and the surrounding umbra in higher layers ($-3 \leq \log(\tau_{500}) \leq -2$, where τ_{500} is the optical depth at 500 nm), and upflows of 0.8 km s^{-1} in deeper layers ($\log(\tau_{500}) = 0$) only for peripheral UDs. Similarly, upflows of $\approx 0.4 \text{ km s}^{-1}$ decreasing with time were found only in peripheral UDs by the repetitive Fe I 630 nm line scanning data in Sobotka and Jurčák (2009). Bharti, Joshi, and Jaaffrey (2007) found an upward velocity of the order of 0.4 km s^{-1} surrounded by a downward velocity of 0.3 km s^{-1} within relatively large ($0.5''$) UDs.

The origin of UDs has been addressed by three-dimensional numerical simulations of solar magnetoconvection in strong fields by Schüssler and Vögler (2006). In the simulations, UDs are rising hot plumes, which radiatively cool at the surface, giving rise to overturning motions. Furthermore, the plumes show a substructure in computed intensity maps, a central dark lane, caused by a local density enhancement which locally elevates the $\tau = 1$ level to higher and cooler layers. Properties of these simulated UDs have been more recently studied by Bharti, Beeck, and Schüssler (2010). There is some evidence that observed UDs show such a dark lane (Bharti, Joshi, and Jaaffrey 2007; Rimmele 2008; Bharti *et al.* 2007; Sobotka and Puschmann 2009).

Similarly, Heinemann *et al.* (2007) performed simulations to study the penumbral fine structure. In their simulations penumbral structures develop and show striking morphological and kinematic similarities to the observed fine structure, e.g., dark cored filaments and an inward migration of those structures towards the umbra (see, e.g., Figure 5 in Heinemann *et al.* 2007).

UDs are not the only structures found in the umbra. There are also light bridges (LBs), which may appear with different sizes and shapes. A faint thin streamer in the umbra which appears to consist of a chain of bright UDs is called an umbral LB (Muller 1979). Katsukawa *et al.* (2007) observed the continuous formation of an umbral LB for several days and found that the precursor of the LB formation as a relatively slow inward motion of UDs. During its formation, many UDs were observed to be rapidly intruding into the umbra ($1\text{--}2 \text{ km s}^{-1}$). The existence of such inward motions in umbral LBs has been also reported by Berger and Berdyugina (2003) and Rimmele (2008).

The present analysis concentrates on the temporal evolution of a peculiar UD detected in the observations, which is accompanied by a clear and persistent blueshift signature throughout its lifetime. The UD appeared at the umbral-penumbral boundary and propagated rapidly towards the more central parts of the umbra with a horizontal speed of

1.3 km s^{-1} . The spectroscopic observations of the Fe I 709.04 nm line were recorded with a two-dimensional tunable filtergraph featuring high spectral and spatial resolution. The spectral line scans allow us to perform a bisector analysis to derive line-of-sight (LOS) velocities that are roughly representative of different heights in the solar atmosphere. In the following sections, we describe the observations (Section 2.2), the line profile analysis (Section 2.3), the results (Section 2.4), and in Section 2.5 we discuss our results.

2.2. Observations and Data Reduction

The observations were performed on 24 August 2006, utilizing the Interferometric Bi-dimensional Spectrometer (IBIS)¹ installed at the Dunn Solar Telescope (DST) of the National Solar Observatory (NSO), Sunspot, New Mexico. IBIS is a Fabry–Pérot-based tunable narrowband filtergraph (for details see Cavallini 2006; Reardon and Cavallini 2008).

The target of the observation was the preceding mature sunspot (at about $S8^\circ E36^\circ$, $\mu \approx 0.81$) of active region NOAA 10905 (see Figure 13) which first appeared on the east limb on 21 August 2006. On 27 August the observed sunspot started to disintegrate. The active region triggered several GOES C-class flares (such as the C2.5 event at 19:52 UT on 26 August), but no events occurred during the 2 h of our observational period from 15:49 UT until 17:42 UT on 24 August 2006. During the whole observational period real-time seeing correction and image stabilization was accomplished by a high-order adaptive optics system installed at the DST (Rimmele 2004). However, the last 20 min of the observations suffered from variable seeing conditions and are therefore not included in the analysis. IBIS scanned the magnetically insensitive Fe I 709.04 nm line which has a low response to temperature perturbations, and is thus suitable for measuring LOS velocities (Cabrera Solana, Bellot Rubio, and del Toro Iniesta 2005). The spectral line was sampled at 40 wavelength points on an equidistant grid with a step size of 1.5 pm. The spectral resolution of IBIS at 709 nm is about 295000 (Reardon and Cavallini 2008) which corresponds to a full-width-half-maximum (FWHM) in the transmission profile of 2.4 pm. As a consequence, we only slightly undersampled spectrally since critical sampling implies a spectral step size of 1.2 pm (at 709 nm). A whole scan was completed within 9.6 s, with an exposure time for each filtergram of 20 ms. During the relevant observing time of about 2 h, 148 scans were recorded with a mean cadence of 37 s. The difference between the cadence and the scan acquisition time is caused by the fact that the Fe I 709.04 nm observations comprise only a subset of the full data set. The

¹IBIS has been built by INAF/Osservatorio Astrofisico di Arcetri with contributions from the Universities of Firenze and Roma “Tor Vergata”, the National Solar Observatory, and the Italian Ministries of Research (MUR) and Foreign Affairs (MAE).

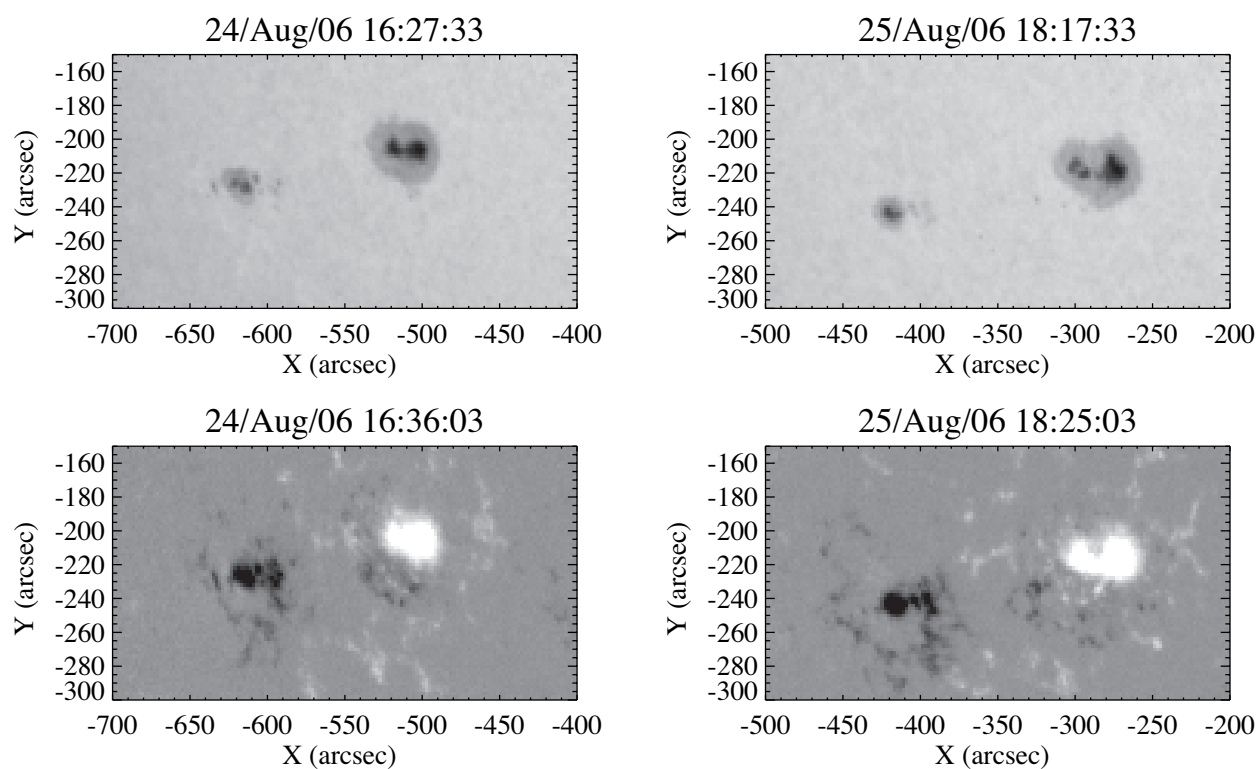


Fig. 13.— NOAA 10905 as seen by the Michelson Doppler Imager (MDI) aboard the Solar and Heliospheric Observatory (SOHO) satellite. Left panel: MDI continuum intensity (top) and longitudinal magnetogram (bottom) on 24 August 2006. Right panel: Same as left but on 25 August 2006.

instrument was operated in the binned readout mode which results in a detector image scale of $0.165'' \text{ pixel}^{-1}$ covering the full IBIS circular field-of-view (FOV) with a diameter of $80''$.

In addition, two other lines were scanned (Na I 589.6 nm, Ca II 854.21 nm). Results from one of those lines (Ca II 854.21 nm) have been already published by Tritschler, Uitenbroek, and Reardon (2008), in which they report the evidence for a current sheet above the umbra.

For each narrowband filtergram a simultaneous broadband image was recorded. The broadband channel was equipped with a filter centered on 721.53 nm with a FWHM of 9.6 nm. The broadband images are used to correct for image shifts during the scan, and light-level fluctuations. For each individual scan of the Fe I line, we perform a speckle reconstruction (based on 120 broadband images acquired within 37 s), and the result is used as a reference for the destretching process applied to the narrowband images of the same scan. The speckle reconstruction is computed using the speckle masking code developed by Wöger and von der Lühe (2007) which takes into account how the speckle transfer function (von der Lühe 1985) is affected by the wavefront correction of the AO system.

Extracted from one scan data set, Figure 14 displays a speckle reconstruction, a broadband image with the highest contrast out of the 40 individual images of the Fe I scan, and the line-wing (-7.5 pm away from the line core) and line-core intensity of the Fe I 709.04 nm line.

2.3. Line Profile Analysis

We performed a bisector analysis to derive the LOS velocities from Doppler shifts that represent the average properties of the solar atmosphere. A bisector is defined as the midpoint in wavelength between equal intensity levels on either side of the spectral line. We calculated 12 bisector positions at intensity levels between 3% (close to line core) and 80% (far line wing, close to the continuum) of the line depth (see Figure 15). The individual bisector positions result from a linear interpolation between the relevant intensities in the observed line profile and the corresponding wavelength positions (see, e.g., Tritschler *et al.* 2004). In order to reduce noise, we average over three bisector levels, which leads to four bisectorgrams: v_{highest} , $v_{\text{mid-high}}$, $v_{\text{mid-deep}}$, and v_{deepest} as is shown in Figure 15.

The Fe I 709.04 nm line is blended with molecular lines formed by TiO in both wings (see, e.g., Wallace *et al.* 1999). These lines are part of the extended TiO γ ($A^3\Phi - X^3\Delta$) system with the bandhead at $\approx 705.425 \text{ nm}$ (14172 cm^{-1}). For low temperatures the molecular lines strengthen and particularly influence the red line wing (Makita 1968; Sinha 1977), as demonstrated by the dark umbral core profile in Figure 15. In addition to the TiO lines there is a CN blend to the red at $\approx 709.069 \text{ nm}$ (Moore, Minneart, and Houtgast 1966),

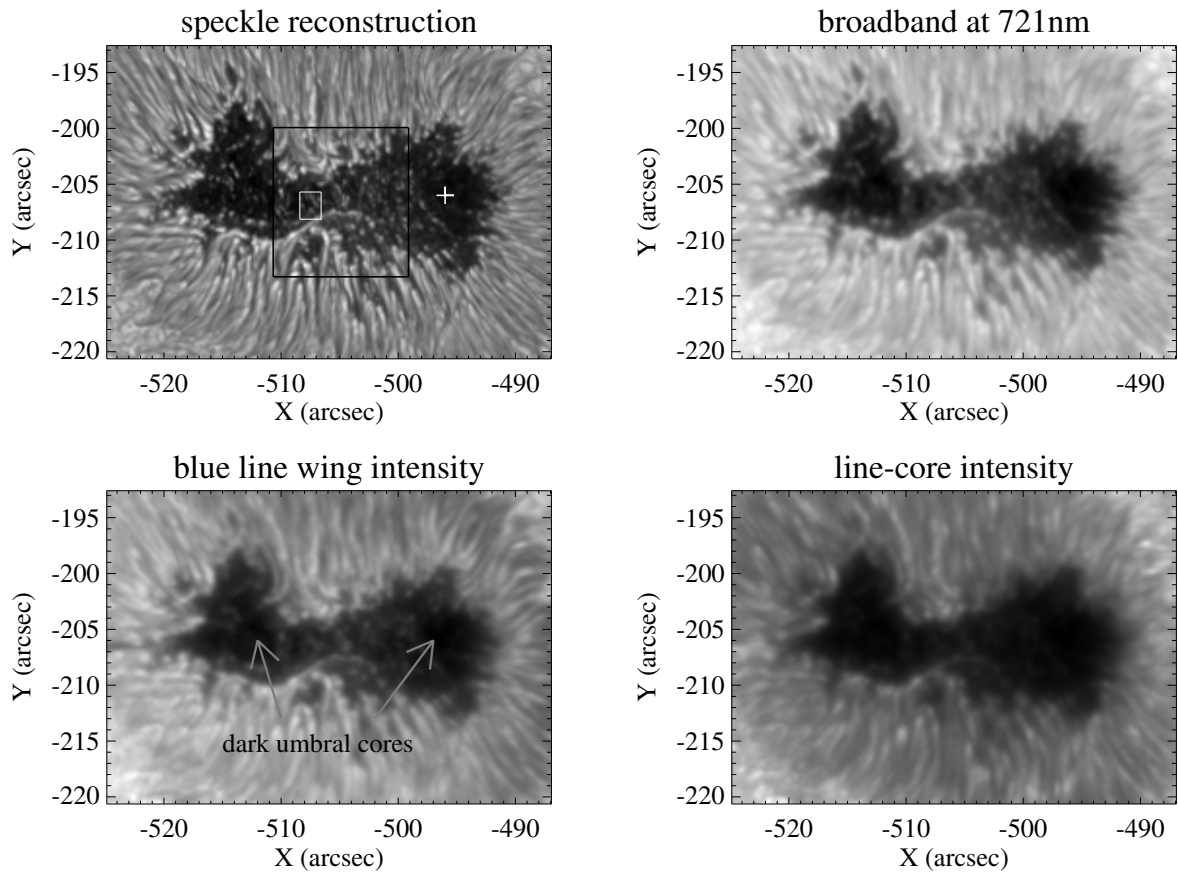


Fig. 14.— Typical maps of a speckle reconstruction (upper left), the broadband continuum intensity at 721 nm (upper right), blue line-wing intensity at -7.5 nm from the line core (lower left), and the line-core intensity of the Fe I 709.04 nm line (lower right). A movie (from 16:46 UT to 17:18 UT) of the area indicated by the black rectangle in the speckle reconstruction is available as online material (http://www.kwasan.kyoto-u.ac.jp/~watanabe/movie_watanabe+etal2010.mov). A zoom-in version of this area is shown in Figure 17. The small white rectangle in the speckle reconstruction indicates the FOV of the individual images displayed in Figure 18. The +-symbol in the speckle reconstruction map is the position of a dark umbral core’s profile shown in Figure 15.

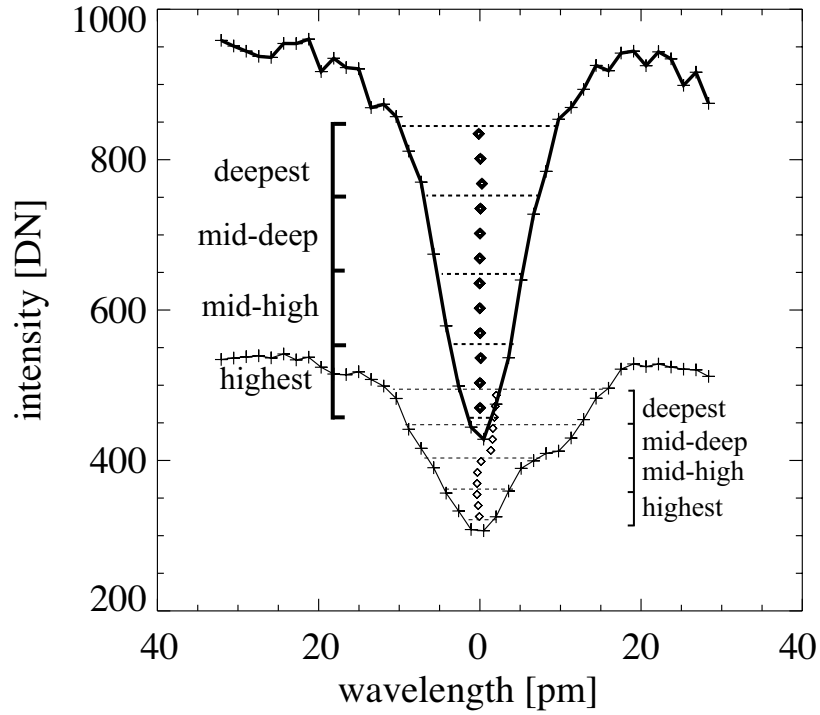


Fig. 15.— Spectral profiles of the scanned Fe I 709.04 nm line extracted from a typical UD site (top) and from the darkest parts of the umbra (bottom, the position is indicated in Figure 14). The plus-symbols indicate the scanned wavelength points. The \diamond -symbols mark the central position (in wavelength) between equal intensity levels on either side of the line profile, *i.e.*, the bisector positions. We average over three bisector levels to define: v_{highest} , $v_{\text{mid-high}}$, $v_{\text{mid-deep}}$, and v_{deepest} .

which is of negligible influence because of its distance to the Fe I line and its narrow line width. The molecular TiO blends are very temperature sensitive and start to strengthen at temperatures that are ≈ 1000 K colder, become really visible at ≈ 1250 K colder, and completely dominate the spectrum for temperatures ≈ 2000 K colder than the quiet solar photosphere. It is important to remark that the TiO lines in the blue wing (about -20 pm from the Fe I line core) have negligible influence on the Fe I line profile in the umbra.

Obviously, the presence of the TiO blends complicates the interpretation of the bisector shapes and thus the derived velocities in the umbral areas. We account for this complication in the following way. We argue that thermal conditions prevailing in UDs and their immediate surroundings are likely to be affected only very little by the molecular lines. We therefore concentrate our analysis on that part of the umbra which is heavily populated with UDs (the area is indicated by the black rectangle in Figure 14). That same (central) part of the umbra is also the location where the sunspot started to form a strong LB one day after our observation and disintegrated three days after our observation. In the late phase of a sunspot, the evolution of LB often indicates (as in our case) a potential fragmentation or break-up. We argue that the heavy accumulation of UDs in the analyzed region is a precursor of the LB formation and is accompanied by changes in the thermal conditions of the subsurface- and line-forming layers that are not favorable for the formation of the TiO lines.

To calibrate the LOS velocities we use the umbral background within the area indicated by the black rectangle in Figure 14 as a frame of reference. First, we remove temporal variations caused by umbral oscillations by applying a low-pass filter (< 3 mHz) to the Fourier transformed Dopplergrams. Second, we calibrate each bisector level separately by subtraction of the corresponding velocity averaged over the umbral background determined within the black rectangle at each time step. As an example, the temporal variation of v_{highest} averaged over the umbral background is shown in Figure 16. We follow the astronomical convention that redshifts are positive (bright in Figures) and blueshifts are negative (dark in Figures).

After this calibration procedure, the LOS velocity of v_{highest} averaged over quiet areas ($4'' \times 1.5''$) outside the sunspot is about -180 m s^{-1} . In order to verify this value we performed preliminary line synthesis calculations based on three different snapshots (corresponding to different time steps) of the three-dimensional radiative MHD simulations by Stein and Nordlund (1998). Those calculations predict an average convective blueshift at the view angle of 36° of about -250 m s^{-1} . Under the assumption that the simulations reflect solar atmospheric conditions close to reality, we ascribe the difference between the observed and predicted values (at least partially) to the fact that the selected umbral reference frame may not be at rest but blueshifted by about -70 m s^{-1} .

The accuracy of the velocity measurement depends mostly on the finite spectral resolu-

tion and the spectral sampling size. The influence of the finite spectral resolution and the sampling size has been addressed by Reardon and Cavallini (2008) (see also Dravins and Nordlund 1990) and Tritschler *et al.* (2002), respectively. In general, finite spectral resolution will straighten the bisector and thus smooth out existing line asymmetries reflected in the bisector shape. Therefore, Doppler shifts are under-estimated. The effect of the finite spectral resolution also depends on the specific spectral line that is used in the observations. Typically, weaker lines will be less prone to such effect than stronger lines. The Fe I 709.04 nm line is not a strong line. From synthesized line profiles convolved with the IBIS transmission profile we estimate that the influence of the finite spectral resolution and the (almost) critical spectral sampling on the Fe I line is in the range of 5–100 m s⁻¹ depending on the individual bisector position. To our best knowledge, the influence of asymmetries present in the IBIS transmission (or instrumental) profile can be considered negligible (see Reardon and Cavallini 2008). The precision of the instrument is estimated as ≈ 5 m s⁻¹ rms at the observed wavelength (Kevin Reardon, private communication). Furthermore, the inaccuracies introduced by the linear interpolation of the discrete spectral sampling positions correspond to 0.02 km s⁻¹.

In addition to the calculation of bisector velocities, we use the line-core and line-wing intensity. The line-core intensity is the image of the fixed wavelength position at the approximate line-core position. The line-wing intensity is taken from the blue line wing at -7.5 pm from the line-core position.

2.4. Results

The observed sunspot showed two dark umbral cores on 24 August. In the middle of the umbra, the number density of UDs was highest. On 25 August, the two umbral cores further separated (Figure 13) and a LB formed in-between. This is the area where we identify a rapidly-moving UD in the speckle reconstructions. This rapidly-moving UD is also visible in maps of the Fe I line-wing and line-core intensity. The UD is accompanied by a clear blueshift signature (Figure 17) during its lifetime. The UD appeared at the periphery of the umbra close to a LB-like structure as if emanating from it, and propagated perpendicularly to the LB-like structure with a large speed. An online movie of the speckle reconstructions and $v_{\text{mid-high}}$ covering the period of 16:46 UT–17:18 UT is available at http://www.kwasan.kyoto-u.ac.jp/~watanabe/movie_watanabe+etal2010.mov.

We define the lifetime of the UD as the time its intensity in the speckle reconstruction is larger than $60\% \times I_{\text{quiet}}$ (I_{quiet} : the intensity averaged over the quiet-sun region surrounding the sunspot). Then, the lifetime of the UD is 8.7 min. It appeared at 17:04 UT and disappeared at 17:13 UT. The diameter of the UD was 240 km, which is the average FWHM of a

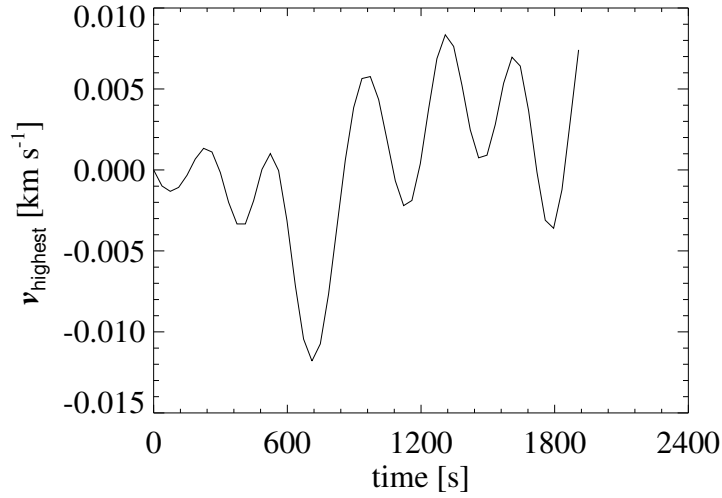


Fig. 16.— v_{highest} averaged over the umbral background within the black rectangle in Figure 14 used for the velocity calibration. The differences from the first frame (16:46 UT) are shown.

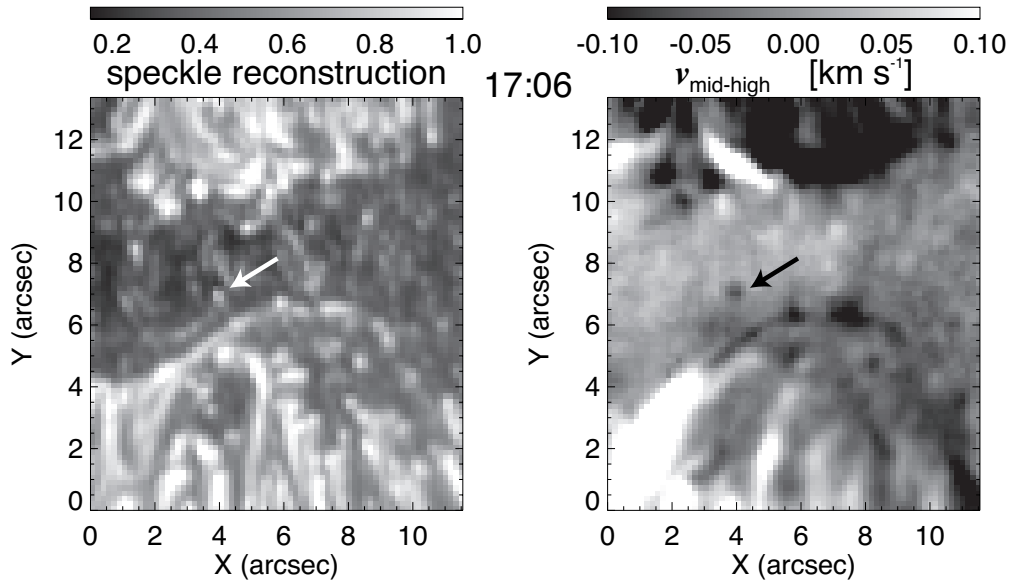


Fig. 17.— Speckle reconstruction (left) and LOS-Dopplergram corresponding to $v_{\text{mid-high}}$ (right) of the area indicated by the black rectangle in Figure 14 as observed at 17:06 UT. The arrows mark the position of the rapidly-moving UD. Blueshifts are negative (dark) and redshifts are positive (bright). A movie is available as online material (http://www.kwasan.kyoto-u.ac.jp/~watanabe/movie_watanabe+etal2010.mov).

Gaussian fit including a linear trend to the UD's speckle reconstructed intensity during its lifetime. In the following we will focus on this particular UD.

After the appearance of the rapidly-moving UD, we observe another consecutive UD following almost the same path. This consecutive UD appeared at 17:08 UT, 4 min after the appearance of the preceding one. However, this consecutive UD did not show a significant blueshift.

2.4.1. The Position of the Rapidly-Moving Umbral Dot

Figure 18 shows the time series of the region marked by the white rectangle in Figure 14 with a $1.86'' \times 2.48''$ FOV. From top to bottom we display from 17:02 UT to 17:14 UT with a cadence of 37 s, the speckle reconstruction, the line-wing and line-core intensity, and the four bisectorgrams. The line-wing and line-core intensities are more sensitive to seeing effect than the composite speckle images.

The position of the UD was first determined by eye-detection on the PC screen using the speckle reconstruction images. Then we fit the intensity distribution around the UD ($3.3'' \times 3.3''$) by the (Gaussian + linear trend) function to improve the accuracy of the peak detection. The resulting position of the UD is indicated by the tick marks in Figure 18. The horizontal motion speed averaged over the UD's whole lifetime is 1.3 km s^{-1} .

Figure 19 shows the timeslice of the UD in x -direction, *i.e.*, the spatial cut along the x -direction at the relevant y -positions of the UD. The spatial coverage for the x -direction is $2.68''$. The trajectory of the UD is shown by the black dashed line. It clearly shows that the UD is co-spatial with persistent blueshifts in all bisector levels. The contour in the speckle reconstruction outlines the intensity $> 60\% \times I_{\text{quiet}}$. The black and gray contours in v_{highest} and $v_{\text{mid-high}}$ outline the level $< -0.03 \text{ km s}^{-1}$. The black and gray contour on $v_{\text{mid-deep}}$ and v_{deepest} outline the level $< -0.04 \text{ km s}^{-1}$.

2.4.2. The Temporal Variation of the Umbral Dot

Figure 20 shows the temporal evolution of different parameters in and around the UD. The solid lines show the temporal evolution of the UD, and the dashed lines show the temporal evolution of the position 430 km eastward from the center of the UD as a reference. All intensities (shown in the top panel of Figure 20) are normalized to the intensity averaged over a quiet-sun region (I_{quiet}). The UD is visible also in the line-wing and line-core intensity, although with a much reduced contrast.

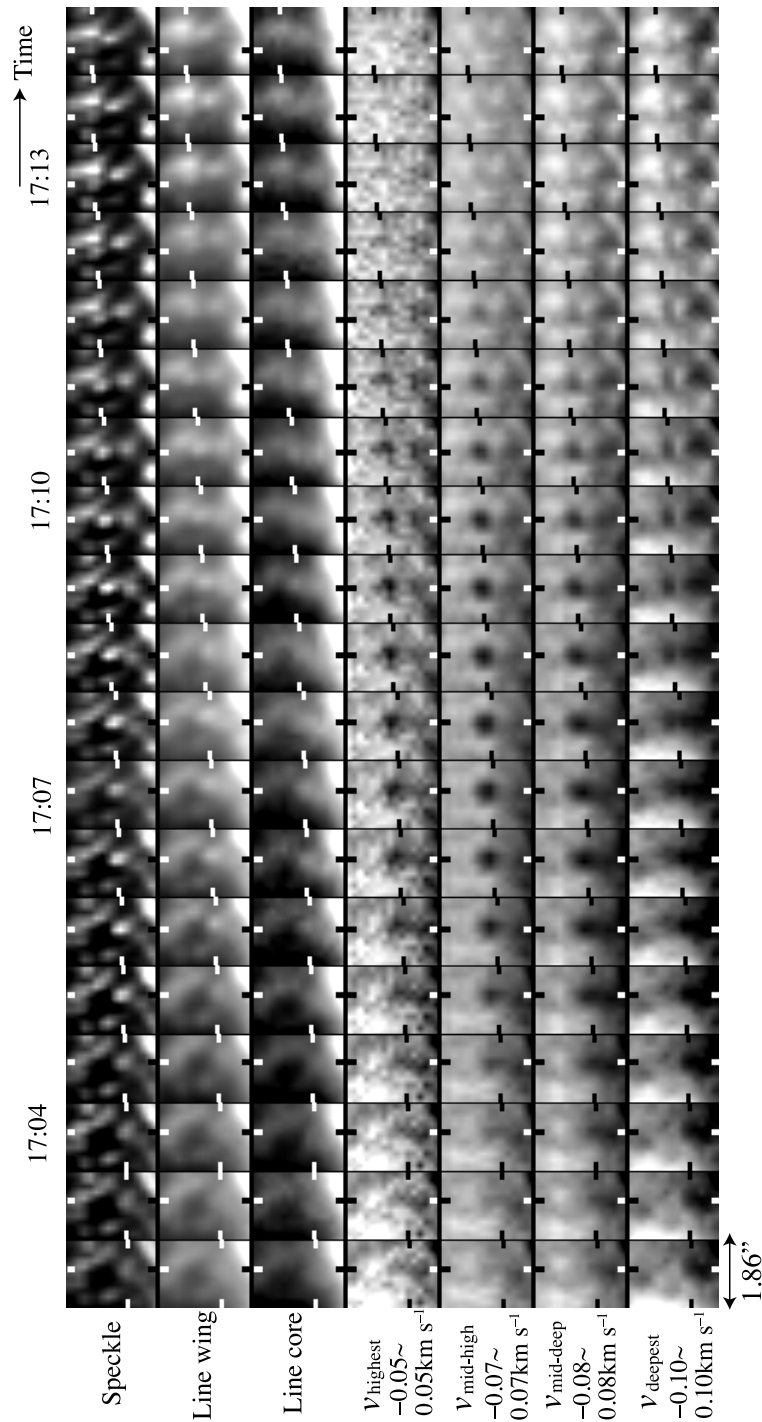


Fig. 18.— Time sequence of the FOV ($1.86'' \times 2.48''$) indicated by the white rectangle in Figure 14. The cadence is 37 s. Top to bottom: speckle reconstruction at 721 nm, line-wing intensity and line-core intensity of Fe I 709.04 nm, LOS velocities (blueshifts are negative) corresponding to v_{highest} , $v_{\text{mid-high}}$, $v_{\text{mid-deep}}$, and v_{deepest} . The black and white ticks mark the UD position.

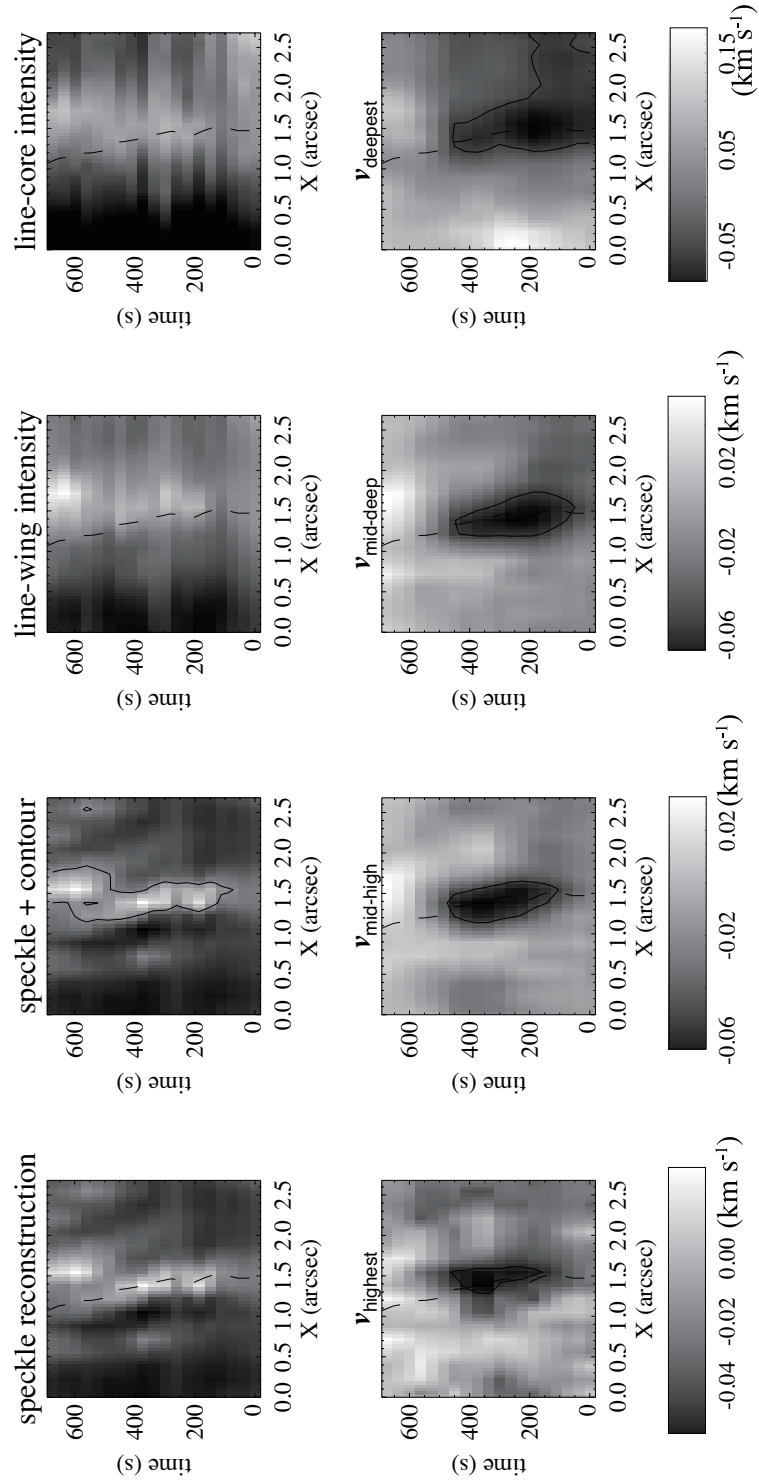


Fig. 19.— Space-time slices of the rapidly-moving UD. Dashed lines indicate the interpolated trajectory of the UD as obtained from the speckle reconstructions. The contour in the speckle reconstruction outlines the intensity $> 60\% \times I_{\text{quiet}}$. Black contours outline the level $v_{\text{highest, mid-high}} < -0.03 \text{ km s}^{-1}$ and $v_{\text{mid-deep, deepest}} < -0.04 \text{ km s}^{-1}$.

The highest blueshift signal appeared in the order of v_{deepest} (190 s after the UD's appearance), $v_{\text{mid-deep}}$ (220 s), and simultaneously in $v_{\text{mid-high}}$ and v_{highest} (370 s). The brightness of speckle reconstruction peaks when the highest blueshift in $v_{\text{mid-high}}$ and v_{highest} are observed. The peak blueshifts are -0.10 km s^{-1} for v_{deepest} , -0.07 km s^{-1} for $v_{\text{mid-deep}}$, -0.06 km s^{-1} for $v_{\text{mid-high}}$, and -0.05 km s^{-1} for v_{highest} . However, there is a possibility that the strong blueshifts in deep layers are biased by the long-lasting blueshift accompanied by the LB-like structure.

2.5. Discussion

We focused on a rapidly-moving UD that appeared at the umbra boundary and propagated towards the center of the umbra. The lifetime and the diameter of the UD are 8.7 min and 240 km, respectively. The average speed of its proper motion is 1.3 km s^{-1} , which is faster than the typical speed of the peripheral UDs (1.0 km s^{-1} at most).

The UD shows a rather strong blueshift compared to other umbral brightenings at all bisector levels. We have to be very careful in interpreting this LOS velocity because of projection effect. The umbra we observed was located at ($S8^\circ E36^\circ$, $\mu \approx 0.81$). This is far from disk center, and blueshifts (redshifts) along the LOS cannot be unambiguously interpreted as upflows (downflows). The measured blue- and redshifts along the LOS are a mixture of vertical and horizontal motions in the solar atmosphere. However, there are two hints which support the idea that the observed blueshift is dominated by a vertical upflow. First, since the horizontal motion of the UD inferred from the apparent movement is almost perpendicular to the LOS, the rapid horizontal proper motion will not contribute to the LOS velocity. Second, the persistent blueshift at all bisector levels is consistent with the picture that the UD is supplied with hot gas from deeper layers which moves upwards and overshoots. The peak blueshifts are -0.10 km s^{-1} for v_{deepest} , -0.07 km s^{-1} for $v_{\text{mid-deep}}$, -0.06 km s^{-1} for $v_{\text{mid-high}}$, and -0.05 km s^{-1} for v_{highest} , which indicates a deceleration with height.

We calculated the contribution functions for different line depressions using the synthesis code described in Grossmann-Doerth (1994) and found the following values: For quiet sun based on the empirical atmosphere of Holweger and Mueller (1974), the line formation height (peak of the response function) of Fe I 709.0 nm line above the continuum level is 225 km at line core, 114 km at line wing, and 98 km at far line wing. For umbra based on the umbral model of Maltby *et al.* (1986), the line formation height is 99 km at line core, 31 km at line wing, and 10 km at far line wing. The formation height at the UD may be intermediate between those of quiet sun and umbra, because the temperature at UD is higher than the surrounding umbra but lower than the quiet sun (Kitai *et al.* 2007). Since the rapidly-moving

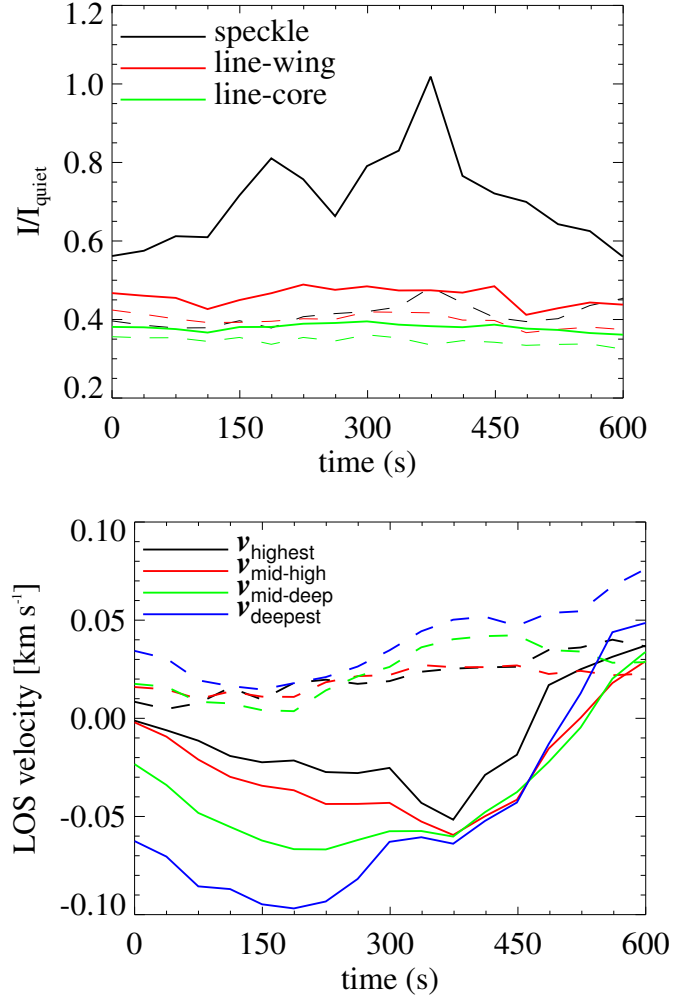


Fig. 20.— Temporal evolution of different parameters at the UD (solid line) and at 420 km eastwards from the UD (dashed line). Upper panel: UD brightness from the speckle reconstruction (black), line-wing intensity (red), and line-core intensity (green). The intensities are normalized to the intensity averaged over a quiet-sun region. Lower panel: v_{highest} (black), $v_{\text{mid-high}}$ (red), $v_{\text{mid-deep}}$ (green), and v_{deepest} (blue). Blueshifts are negative.

UD was visible in the line-core intensity map, the UD, which we suppose to be a result of overshooting convection, reached at least more than 100 km above the continuum level. We can speculate the propagation speed of the overshooting convection by the timing difference between the peak blueshifts in $v_{\text{mid-deep}}$ and v_{highest} . As the height difference between $v_{\text{mid-deep}}$ and v_{highest} is 70–110 km and the timing difference is 150 s, the speed is about 0.5–0.7 km s⁻¹.

The UD we observed is similar to mobile UDs reported in Katsukawa *et al.* (2007), that is, components of a LB. The rapidly-moving UDs in Katsukawa *et al.* (2007) also bring a strong blueshift signal (0.2–0.5 km s⁻¹). We could not see the creation of a LB in our observation period, but the central part of the umbra is the location where the sunspot started to form a strong LB one day after our observation. Therefor we argue that the rapidly-moving UD is a precursor of a LB. Similar phenomena are reported as an extremely faint LB consisting of mobile UDs in Sobotka, Bonet, and Puschmann (1993) and Rimmele (2008).

We could not find an observational signature of downflow patches as in the case of the MHD simulation by Schüssler and Vögler (2006). Only recently Ortiz, Bellot Rubio, and Rouppe van der Voort (2010) found a very small (0.15''–0.3'') localized downflow patches at the edge of dark lanes utilizing the observation of 1-m aperture Swedish Solar Telescope. The persistent blueshift throughout the UD's evolution reported here add supporting evidence of overturning convection mechanism of UDs.

REFERENCES

- Berger, T. E., Berdyugina, S. V. 2003, ApJ, **589**, 117
- Bharti, L., Beeck, B., Schüssler, M. 2010, A&A, **510**, A12
- Bharti, L., Joshi, C., Jaaffrey, S. N. A. 2007a, ApJ, **665**, 79
- Bharti, L., Joshi, C., Jaaffrey, S. N. A. 2007b, ApJ, **669**, 57
- Bharti, L., Joshi, C., Jaaffrey, S. N. A., Jain, R. 2009, MNRAS, **393**, 65
- Cabrera Solana, D., Bellot Rubio, L. R., del Toro Iniesta, J. C. 2005, A&A, **439**, 687
- Cavallini, F. 2006, Sol. Phys., **236**, 415
- Dravins, D., Nordlund, A. 1990, A&A, **228**, 203
- Grossmann-Doerth, U. 1994, A&A, **285**, 1012
- Grossmann-Doerth, U., Schmidt, W., Schroeter, E. H. 1986, A&A, **156**, 347

- Heinemann, T., Nordlund, Å., Scharmer, G. B., Spruit, H. C. 2007, *ApJ*, **669**, 1390
- Holweger, H., Mueller, E. A. 1974, *Sol. Phys.*, **39**, 19
- Ichimoto, K., Lites, B., Elmore, D., Suematsu, Y., Tsuneta, S., Katsukawa, Y., *et al.* 2008, *Sol. Phys.*, **249**, 233
- Katsukawa, Y., Yokoyama, T., Berger, T.E., Ichimoto, K., Kubo, M., Lites, B., *et al.* 2007, *PASJ*, **59**, 577
- Kitai, R., Watanabe, H., Nakamura, T., Otsuji, K., Matsumoto, T., Ueno, S., *et al.* 2007, *PASJ*, **59**, 585
- Makita, M. 1968, *Sol. Phys.*, **3**, 557
- Maltby, P., Avrett, E. H., Carlsson, M., Kjeldseth-Moe, O., Kurucz, R. L., Loeser, R. 2007, *ApJ*, **306**, 284
- Moore, C. E., Minneart, M. G. J., Houtgast, J. 1966, *The Solar Spectrum 2935 Å to 8770 Å*, *National Bureau of Standards Monograph* **61**, US Department of Commerce
- Muller, R. 1979, *Sol. Phys.*, **61**, 297
- Ortiz, A., Bellot Rubio, L. R., Rouppe van der Voort, L. 2010, *ApJ*, **713**, 1282
- Reardon, K. P., Cavallini, F.: 2008, *A&A*, **481**, 897
- Riethmüller, T. L., Solanki, S. K., Lagg, A. 2008, *ApJ*, **678**, 157
- Riethmüller, T. L., Solanki, S. K., Zakharov, V., Gandorfer, A. 2008, *A&A*, **492**, 233
- Rimmele, T. 2008, *ApJ*, **672**, 684
- Rimmele, T.: 2004, In: Bonaccini Calia, D., Ellerbroek, B.L., Ragazzoni, R. (eds.), *Advancements in Adaptive Optics, Proc. SPIE*, **5490**, 34
- Schüssler, M., Vögler, A. 2006, *ApJ*, **641**, 73
- Sinha, K. 1977, *Bull. Astron. Soc. India* **5**, 49
- Sobotka, M., Jurčák, J. 2009, *ApJ*, **694**, 1080
- Sobotka, M., Puschmann, K. G. 2009, *A&A*, **504**, 575
- Sobotka, M., Bonet, J. A., Vazquez, M. 1993, *ApJ*, **415**, 832
- Sobotka, M., Brandt, P. N., Simon, G. W. 1997, *A&A*, **328**, 689

Solanki, S. K. 2003, *A&A Rev.*, **11**, 153

Stein, R. F., Nordlund, A. 1998, *ApJ*, **499**, 914

Tritschler, A., Uitenbroek, H., Reardon, K. 2008, *ApJ*, **686**, 45

Tritschler, A., Schmidt, W., Langhans, K., Kentischer, T. 2002, *Sol. Phys.*, **211**, 17

Tritschler, A., Schlichenmaier, R., Bellot Rubio, L.R., the KAOS Team 2004, *A&A*, **415**, 717

Tsuneta, S., Ichimoto, K., Katsukawa, Y., Nagata, S., Otsubo, M., Shimizu, T., *et al.* 2008, *Sol. Phys.*, **249**, 167

von der Lühe, O. 1985, *A&A*, **150**, 229

Wallace, L., Livingston, W. C., Bernath, P. F., Ram, R. S. 1999, *An Atlas of the Sunspot Umbral Spectrum in the Red and Infrared from 8900 to 15,050 cm⁻¹ (6642 to 11,230 Å)*, Revised, *NSO Technical Report #99-001*, US National Solar Observatory, Tucson, Arizona

Wöger, F., von der Lühe, O. 2007, *Appl. Opt.*, **46**, 8015

3. Characteristic Dependence of Umbral Dots on their Magnetic Structure

Abstract

Umbral dots (UDs) were observed in a stable sunspot in NOAA 10944 by the *Hinode* Solar Optical Telescope on 2007 March 1. The observation program consisted of blue continuum images and spectropolarimetric profiles of Fe I 630 nm line. An automatic detection algorithm for UD's was applied to the 2 hr continuous blue continuum images, and using the obtained data, the lifetime, size, and proper motion of UD's were calculated. The magnetic structure of the sunspot was derived through the inversion of the spectropolarimetric profiles.

We calculated the correlations between UD's parameters (size, lifetime, occurrence rate, proper motion) and magnetic fields (field strength, inclination, azimuth), and obtained the following results: (1) Both the lifetime and size of UD's are almost constant regardless of the magnetic field strength at their emergence site. (2) The speed of UD's increases as the field inclination angle at their emergence site gets larger. (3) The direction of movement of UD's is nearly parallel to the direction of the horizontal component of magnetic field in the region with strongly inclined field, while UD's in the region with weakly inclined field show virtually no proper motion.

Our results describe the basic properties of magnetoconvection in sunspots. We will discuss our results in comparison to recent magnetohydrodynamic simulations by Schüssler & Vögler (2006) and Rempel et al. (2009).

3.1. Introduction

Umbral dots (UDs), small bright points with size of ~ 300 km and lifetime of ~ 15 minutes, are observed ubiquitously across the umbra (Sobotka et al. 1997a,b; Thomas & Weiss 2004). Since the first observation of UD's by Chevalier (1916), it has been found that UD's play an important role in the energy balance in sunspots. The brightness of an umbra is about 5%-

20% of that of a quiet region, because convection is strongly suppressed in the presence of a strong magnetic field (a few thousand gauss in an umbra). However, in order to account for the observed brightness of an umbra, heat must be supplied by convective transport (Deinzer 1965). UDs are the signature of this convective heat transport. Therefore, understanding the physics of UDs is key to constructing a precise model of sunspot substructure.

The mechanism behind the formation of UDs is thought to be magnetoconvection. In recent years, theoretical studies of magnetoconvection have greatly improved knowledge of the phenomena. Two-dimensional magnetoconvection in a Boussinesq fluid was studied by Proctor & Weiss (1982), and a systematic investigation of compressible magnetoconvection was described by Weiss et al. (1990). Weiss et al. (1990) revealed that the modes of magnetoconvection are governed by the ratio ζ of the magnetic diffusivity to the thermal diffusivity. For $\zeta \lesssim 1$, we obtain oscillatory convection with periodic reversals of the flow velocity. For $\zeta \gtrsim 1$, overturning convection occurs with a spatially asymmetric rising and falling of the convective plumes. In the quiet photosphere, the thermal diffusivity usually exceeds the magnetic diffusivity and as a result ζ is far smaller than unity. In the umbra, however, the atmospheric conditions are such that $\zeta < 1$ near the surface and $\zeta > 1$ at depth below 1500 km. Because of these complex atmospheric condition, the magnetoconvection in sunspots has been investigated mainly through the use of computer simulations (Schüssler & Vögler 2006; Heinemann et al. 2007; Rempel et al. 2009). In the simulations by Schüssler & Vögler (2006), they found that UDs are convective plumes that are triggered by oscillatory convection, but turn into overturning cells because of the radiative cooling at the surface. Upward velocity surrounded by downflow was found in Fe I 5576Å line observation (Bharti et al. 2007), which was suggested to be supporting evidence of overturning convection.

Observations of umbra have revealed that UDs form at regions with a reduced field strength and a local upward velocity (Watanabe et al. 2009; Sobotka & Jurčák 2009). Socas-Navarro et al. (2004) found that there are systematic differences between UDs and the surrounding umbra, such as small upflows ($\sim 100 \text{ m s}^{-1}$), higher temperatures ($\sim 1 \text{ kK}$), and weaker fields ($\sim 500 \text{ G}$) with more inclined orientations ($\sim 10^\circ$). These results are consistent with theoretical models for the convection processes driving UDs. In this paper, we report the statistical relationship between the magnetic field and UDs through the use of filtergram and spectrogram observations from the *Hinode* Solar Optical Telescope (SOT). If UDs are the convective plumes controlled by the magnetic field, there must be correlations between UDs and magnetic field, for example, between field strength and UD's size, or between field strength and proper motion of UDs. Our results can serve as a guide for more realistic magnetohydrodynamic (MHD) simulations, leading toward an ultimate understanding of the subsurface structure of sunspots.

In the following sections, we describe the observations and the data reduction techniques

(Section 3.2), explain the UD detection algorithm (Section 3.3), analyze the properties of UDs and their relationship to the magnetic fields (Section 3.4), and finally we will discuss the results in Section 3.5.

3.2. Observation and Data Reduction

The target in this paper is a stable and circular sunspot in NOAA 10944 observed with the *Hinode* SOT. With the SOT/Broadband Filter Imager (BFI) (Tsuneta et al. 2008), blue continuum images were taken from 00:14UT till 02:30UT on 2007 March 1. The blue continuum image by the SOT/BFI has wavelength centered on 450.45 nm and the line width of 0.4 nm. The diffraction limit of blue continuum for the *Hinode* SOT is 164 km. On March 1, the sunspot was located almost at the disk center: the heliocentric coordinates for the sunspot at 00:14UT on March 1 were (63'', 17''). The images were taken with a constant 6 s interval. However, since we analyzed every fourth image, in our study the temporal cadence is ~ 25 s. The spatial pixel size was $0.054'' \times 0.054''$, and the exposure time was relatively long, 102 ms, in order to obtain adequate photons for the umbra. The field of view (FOV) of the images was $54'' \times 27''$, which contains the entire umbra.

The total number of the continuum images was 321, which covers the observational period of 136 minutes. After the dark field subtraction and the flat fielding, the images were carefully co-aligned by finding the displacement which gave the maximum cross-correlation between consecutive frames. In order to reduce high-frequency noise in space caused by CCD or photon noise, we applied a low-pass filter (Hanning filter) to the Fourier transformed image, and then an inverse Fourier transformation was performed. Finally, we normalized the images with a low-frequency component of the averaged light curve of the quiet-Sun region. In doing so, we removed the effect of the small orbital variation of the CCD gain whose period is ~ 96 minutes.

In addition to the filtergram, we used the *Hinode* spectropolarimeter (SP) data to study the magnetic field of the sunspot. Unfortunately, no SP data were taken simultaneously with the blue continuum imaging. Instead, we created a composite map from the two closest SP maps taken before and after the filtergram imaging. One map was taken at 17:58UT on February 28 (about 6 hr before the start of the filtergram observation), and the other was taken at 06:14 on March 1 (about 4 hours after the end of the filtergram observation). The spectral FOV includes the two magnetic-sensitive iron lines, Fe I 630.15 nm and 630.25 nm. The two SP scans were carried out in normal mode. In this mode, it takes about 45 minutes to scan the FOV of $76'' \times 82''$ with a polarization accuracy of 0.1%. The observed full Stokes parameters (I , Q , U , V) were processed through a dark field subtraction, a flat fielding, and a thermal drift calibration using the standard routine.

To extract the magnetic field information, we applied the Milne-Eddington inversion (Yokoyama et al. 2009, in preparation) to the calibrated profiles. The umbral photosphere is well suited to the application of Milne-Eddington inversions, since the velocity and magnetic field gradients are very small. As a result of the inversion, we obtained maps of magnetic field strength (B), field inclination (i), and field azimuth (ψ).

The two magnetic maps, taken at the different times, were rotated to match the sunspot's orientation at 01:30UT on March 1 (in the middle of the filtergram observation) by a coordinate rotation. In this procedure, the magnetic field inclination and azimuth were converted using a planar approximation. The inclination is, hereafter, defined by the angle between a field line and the local normal, i.e., 0° inclination means a vertical, 90° inclination means a horizontal field line. The field azimuth is measured counterclockwise from the right-to-left (east) direction. Subsequently, the two maps were co-aligned by finding the best cross-correlation displacements and averaged into one map. Finally, the magnetic strength and inclination maps were boxcar-smoothed with a width of $1.1'' \times 1.1''$ to extract the global structure. We define this composite map as the magnetic field at 01:30UT on March 1, and use it for the following analysis. It is worth noting that our composite magnetic map can be used only for retrieving the global magnetic characteristics, because the individual original magnetic maps (6 hr before and 4 hr afterward) may include local variations contributed by UDs.

The obtained SP map is enlarged to have the same pixel size as that of the blue continuum image. For the alignment process between the blue continuum and the SP, we made the line wing intensity map at around 630.3 nm. The smallest displacement was calculated using the blue continuum image taken at 01:30UT and the line wing intensity map by a cross-correlation analysis.

As can be seen in Figure 21, the sunspot was almost circular and encompassed with a penumbra. Two umbral dark core regions with large field strengths >2600 G can be seen in the southern region of the sunspot. Between these two dark cores, a short light bridge connects to the southern penumbra .

3.3. Automatic Detection Algorithm

To perform a statistical analysis of UDs, it is necessary to use an automatic detection algorithm, because the sunspot of interest produced numerous UDs. Based on previous papers which utilized automated algorithms, such as Sobotka et al. (1997a) and Riethmüller et al. (2008), we constructed a new automatic detection algorithm. Compared to previous work, our algorithm can be kept simpler since the *Hinode* data are free from variable atmospheric

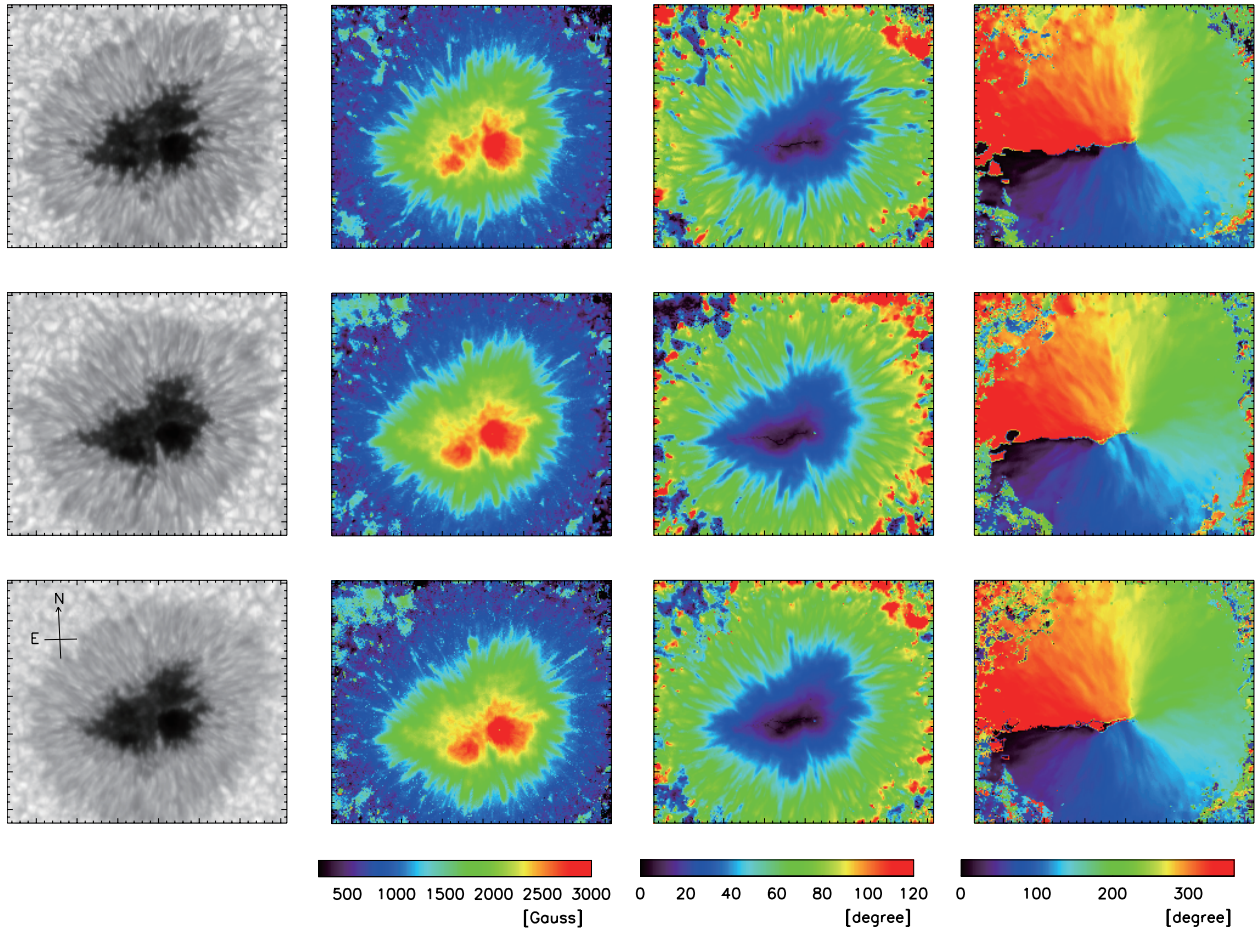


Fig. 21.— From left to right: the continuum intensity at ~ 630.3 nm, magnetic field strength, field inclination, and field azimuth. From top column to bottom: the SP at 17:58UT on February 28 (the images were rotated to the sunspot's location at 01:30UT on March 1, see the text), the SP at 06:14UT on March 1 (ditto), and the composite map of the two (before smoothing). The marks are shown in $1''$ intervals on all sides of the images.

seeing conditions.

The algorithm consists of six steps.

1. Identify local peaks where $I(x, y)$ (I : intensity of a pixel normalized by the averaged quiet region) is equal to the maximum value within ± 2 pixels (± 78 km) of the vicinity (Figure 22(b))
2. Construct background image (bg). First, from the original image, we assign the minimum intensity within ± 6 pixels (± 235 km) of its vicinity into each pixel. The obtained image is boxcar-smoothed with a width of 20×20 pixels (782 km). Define the umbra as the region where the intensity of bg is less than 0.4. This umbra region will be analyzed in the following steps. (Figure 22(c)).
3. Define UD's positions as pixels where $I_{peak}(x, y)/I_{bg}(x, y)$ is larger than 1.3. The total number of UDs in each frame is on average 124 (Figure 22(d)).
4. Calculate the size of the UDs. When determining the size, we apply two different methods and take the smaller value of the two. The first method uses the distance from the UD's peak position to the nearest inflection point; the second one uses the distance to the threshold of $0.5*(I_{peak}(x, y) - I_{bg}(x, y)) + I_{bg}(x, y)$. These calculations are applied to the eight directions spaced at 45° intervals from the peak positions. Finally, we take the median of the eight values (Figure 22(e) and (f)).
5. Once the position of each UD in every frame has been decided, the temporal succession of each UD is determined as follows: the succession is confirmed if an UD is found in the next frame (taken 25s later) within ± 2 pixels of its previous position. If no UD is found, the continuation ends at that point. However, when there is no UD in the next frame but an UD is found within ± 2 pixels in the following one or two frames, the succession is continued. Fission (two UDs within ± 2 pixels) and fusion (two UDs coalesce into one UD) events are taken into account, though these events are scarce (less than 0.2% of all UDs in one frame). This procedure is applied to all UDs until they fade out, or the final frame of the data is reached.
6. Classify UDs into two categories, i.e., central UDs (umbral origin) and peripheral UDs (penumbral origin). The boundary between central and peripheral UDs is set to the contour line of $I_{bg}=0.2$. Peripheral UDs are those which have their origins in brighter region, i.e., outside of the $I_{bg}=0.2$ contour (Figure 22(d)).

Using the above method, 2268 UDs were detected. Out of 2268 UDs, 825 of them were central UDs and 1443 of them were peripheral UDs. We want to note that 245 UDs

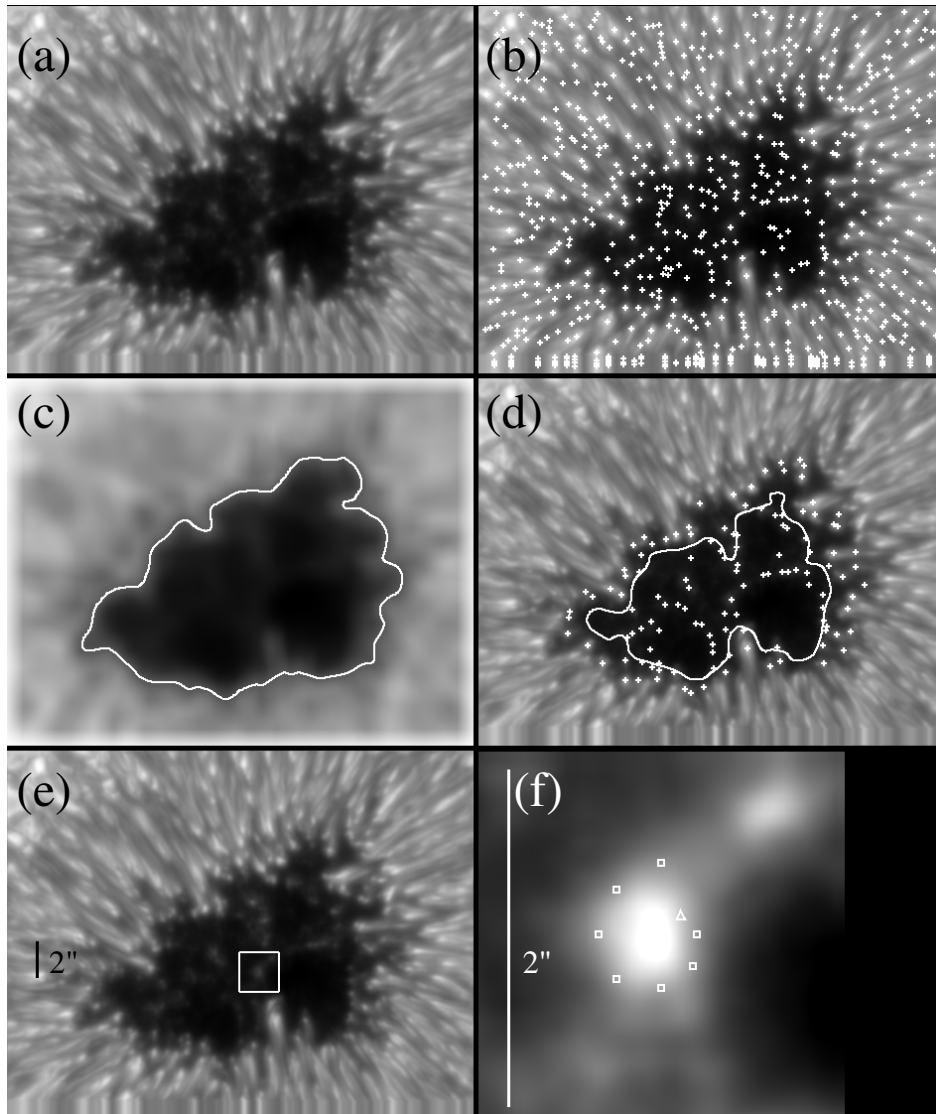


Fig. 22.— (a) Hanning filtered image (b) Peak detection (c) Background image. The contour denotes the boundary of the umbra ($I_{bg}=0.4$). (d) UD positions. The contour denotes the boundary of peripheral UDs ($I_{bg} =0.2$). UDs outside of the contour are peripheral, and UDs inside are central. (e) The position of the UD shown in (f). (f) An example of the size calculation. The seven squares (threshold of $I(x, y)=0.5*(I_{peak}(x, y) - I_{bg}(x, y))+I_{bg}(x, y)$) and the triangle (inflection point) indicate the UD's boundary points for the eight directions.

either already existed before the first frame or lasted longer than the end of the observation. These 245 UDs can not be tracked from the beginning to the end, so their lifetimes are underestimated. Nevertheless, we include these UDs in our analysis, because they sometimes represent long-life UDs.

3.4. Results

We detected the temporal trajectories of 2268 UDs using the method described in Section 3.3. Using this information, we calculated the eight parameters which characterize the UDs: lifetime, average size, brightness ratio, velocity amplitude, velocity orientation, magnetic field strength, field inclination, and field azimuth. The term “velocity” in our analysis refers to the proper motion, that is, the horizontal velocity. These parameters are defined as follows:

- Lifetime (T): (temporal cadence 25 s) \times (number of frames in which the UD is observed).
- Average size (S): the average of the individual size calculated at frames in which the UD is observed (the size in each frame is described in Section 3.3, step (4)).
- Brightness ratio (R): the average of the individual I_{peak}/I_{bg} calculated at frames in which the UD is observed.
- Velocity amplitude ($|V|$): (the distance between its emergence and fade-out location)/(lifetime).
- Velocity orientation (v): the direction from its emergence location to its fade-out location measured counter-clockwise from the left-to-right (west), i.e., in the opposite direction of the field azimuth.
- Magnetic field strength (B): the magnetic field strength at its origin (note that the magnetic field information is global, composed from two SP maps taken at different times. See Section 3.2).
- Field inclination (i): the field inclination at the UD’s origin.
- Field azimuth (ψ): the field azimuth at the UD’s origin.

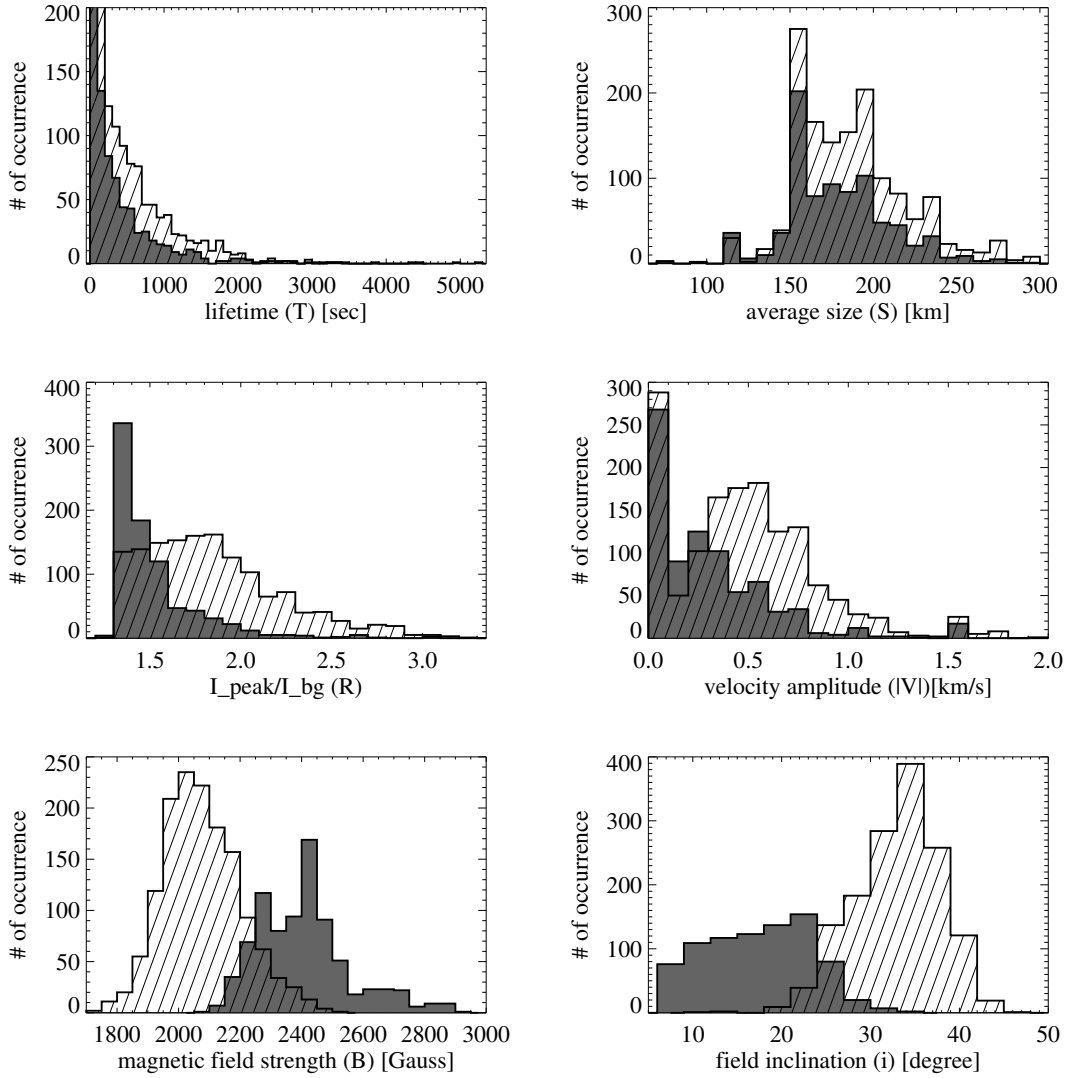


Fig. 23.— Histograms for 2268 UD. The gray and hatched regions correspond to the central and peripheral UD, respectively.

3.4.1. Histogram

Figure 23 shows the histograms of the six parameters ($T, S, R, |V|, B, i$). The gray and hatched bars indicate the central and the peripheral UDs, respectively. The average values of each parameter are summarized in Table 1. As the diffraction limit of blue continuum imaging is 164 km, UDs with a size smaller than 164 km can not be defined accurately. We found that peripheral UDs tend to have brighter intensity, faster proper motion, weaker field with a larger field inclination than central UDs. This result is consistent with Sobotka et al. (1997a,b) and Kitai et al. (2007), which supports the validity of our automatic detection method.

3.4.2. Scatter Diagrams

Next, we study the scatter plots of the parameters of UDs against the magnetic field strength and inclination, as shown in Figure 24. Please refer to Figure 21 for the spatial distributions of the magnetic field components. Considering the large 1σ errors, the lifetimes of UDs are independent of the magnetic field strength and inclination. The sizes of UDs are almost constant, at approximately 190 km. There is a hint that the average size in the dark umbral core ($B > 2600$ G and $i \sim 20^\circ$) is about 20% smaller compared to 190 km, though the statistical significance remains unproved. Because of the large scatter and non-Gaussian distributions of the samples, the brightness ratio I_{peak}/I_{bg} does not show a clear correlation with the field strength, although high contrast UDs seems to correspond to low magnetic field (~ 2000 G). We will study these topics further in Section 3.4.4. The velocity amplitude shows a clear dependence both on the field strength and on the field inclination, with the dependence on the field inclination being more pronounced than on the field strength. Most of the samples with $|V|=0$ km s $^{-1}$ and >1.5 km s $^{-1}$ corresponds to short-lived UDs, because

Table 1: Average of UD parameters

	Average of 2268 UDs	Average of 825 Central UDs	Average of 1443 Peripheral UDs
T (s)	441	391	469
S (km)	184	178	187
R	1.73	1.51	1.85
$ V $ (km s $^{-1}$)	0.44	0.33	0.50
B (G)	2197	2406	2077
i (deg)	27	17	33

1 pixel movement (39 km) in one frame (25 s) results in $|V|=1.56 \text{ km s}^{-1}$. If we neglect these short-lived UDs, the velocity amplitude clearly increases with the field inclination.

Figure 25 shows the six scatter diagrams of the velocity orientation of UDs versus the field azimuth for 1762 UDs for different ranges of the field inclination. Here, we ignored the 506 UDs which had no detectable movement from their emergence to fade out, because their velocity orientation could not be defined. Note that the 0° direction of the velocity orientation and of the field azimuth have opposite directions. Thus, an UD which move toward the center of the umbra along the field line has the same velocity orientation angle as the field azimuth. In the bottom panels of Figure 25, the velocity orientation angles are nearly parallel to the field azimuth. This is because the peripheral UDs generally move umbra inward. However, this correlation is weaker for UDs with smaller field inclinations (upper panels in Figure 25). The correlation coefficients for the different inclination ranges are: 0.22 (inclination $<15^\circ$), 0.45 (15° - 20°), 0.47 (20° - 25°), 0.63 (25° - 30°), 0.64 (30° - 35°), and 0.75 ($>35^\circ$). Therefore, we conclude that the velocity orientation of UDs in regions with large field inclination is determined by the field azimuth, while the velocity orientation of UDs in regions with small field inclination is weakly dependent on the field azimuth.

3.4.3. Spatial Distribution

It is known that dark cores include few UDs (Beckers & Schröter 1968; Kitai et al. 2007), because the magnetic field in dark cores is too strong to produce effective magnetoconvection. We confirmed that strongly magnetized regions include fewer UDs, as shown in Figure 26. The occurrence rate is given by the ratio of the number of UDs within regions of a specific field strength to the area of these regions. The left image in Figure 26 shows the distribution of the emergence positions of all UDs. A cluster of UDs appear in the areas surrounding the dark cores, which may be an indication of flux separation (Tao et al. 1998; Weiss et al. 2002). As well as UDs surrounding the dark cores, we can see some cellular patterns in the left image of Figure 26. These cellular patterns may reflect the global subsurface magnetic field configuration as was supposed in the cluster model (Parker 1979). The temporal evolution of these global cellular patterns is of great interest and should be studied further.

The histograms of the difference between the emergence (start) and fade-out (end) locations of the field strength and the inclination are shown in Figure 27. 73% of the peripheral (hatched) and 56% of the central UDs (gray) faded out in an area with a larger field strength than in their emergence location, while only 8.0% of the peripheral and 16% of the central UDs faded out in an area with a smaller field strength. Similar results are found for the field inclination in Figure 27(b): 73% of the peripheral and 58% of the central UDs faded out in an area with a less inclined field than in their emergence location, while 7.5% of the peripheral

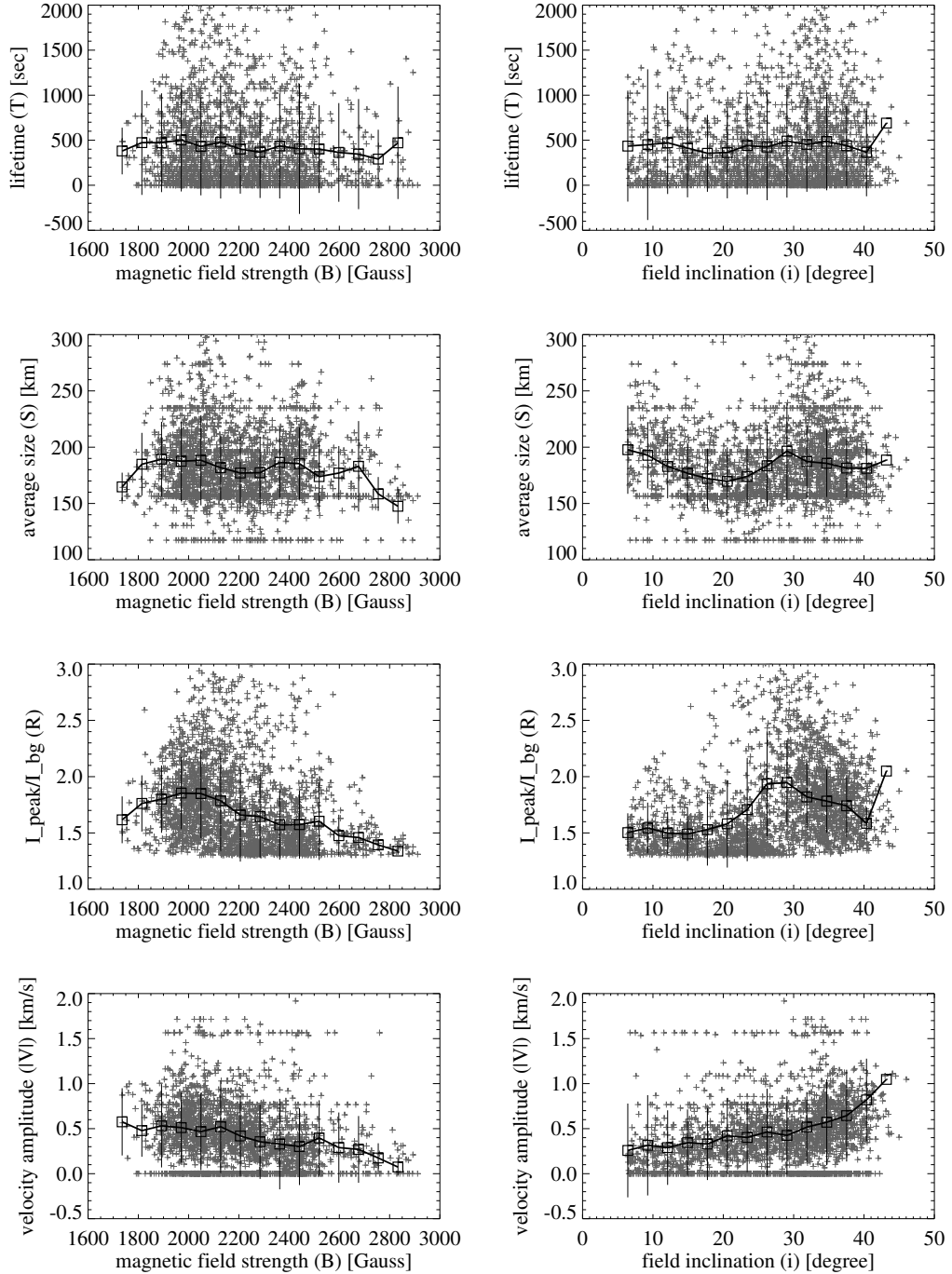


Fig. 24.— *Left column:* scatter plots of the lifetime, average size, I_{peak}/I_{bg} , and velocity amplitude vs. the magnetic field strength. The average of bins of 80 G is shown with square symbols, and the solid lines denote the standard deviation error bars. *Right column:* scatter plots of the lifetime, average size, I_{peak}/I_{bg} , and velocity amplitude vs. the field inclination. The average of bins of 3° is shown with square symbols, and the solid lines denote the standard deviation error bars.

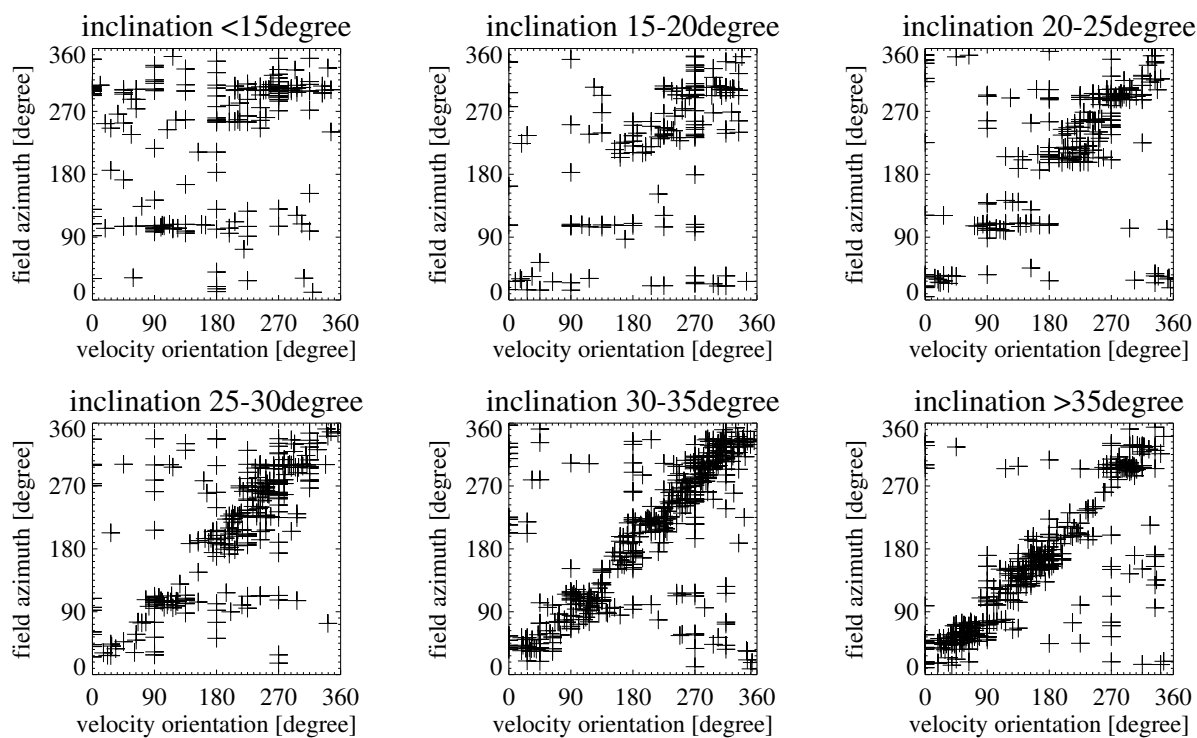


Fig. 25.— Scatter plots of the velocity orientation vs. the field azimuth for different ranges of the field inclination.

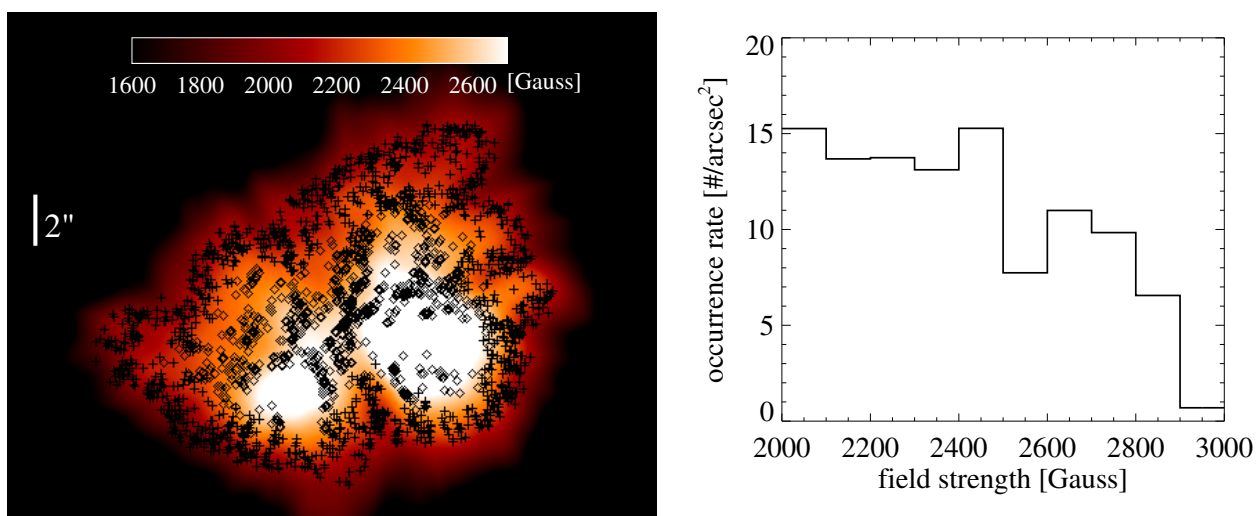


Fig. 26.— *Left*: the emergence positions of the central UDs (diamonds) and the peripheral UDs (plus signs), overlaid on the background image of the magnetic field strength. *Right*: the UD's occurrence rate vs. the field strength with field strength bins of 100 G.

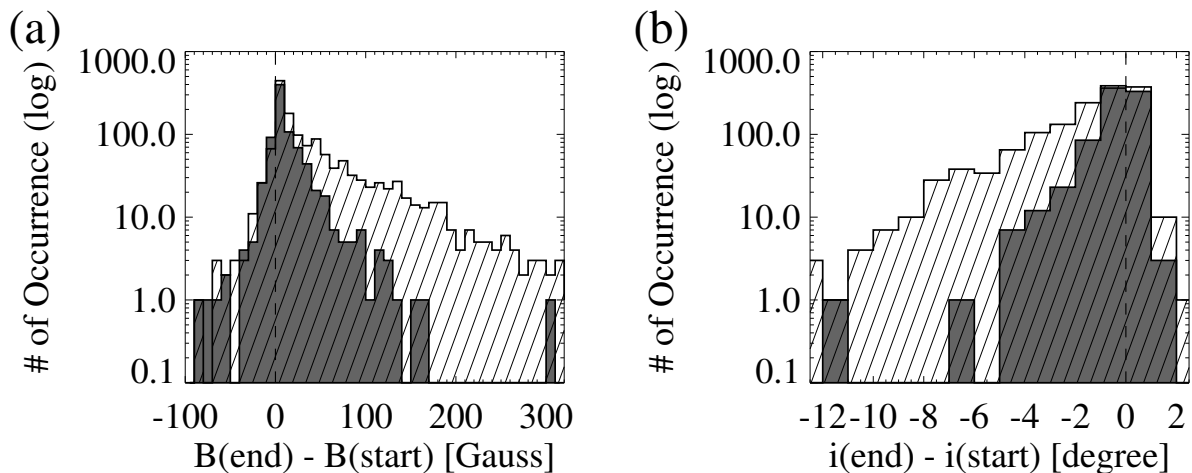


Fig. 27.— (a) Histogram of the field strength differences between their emergence (start) and fade-out (end) locations (log scale). The gray bars indicate central UDs, the hatched bars indicate peripheral ones. (b) Histogram of the field inclination differences between their emergence (start) and fade-out (end) locations (log scale). The gray bars indicate the central UDs, and the hatched bars indicate the peripheral ones.

and 12% of the central UDs faded out in an area with a more inclined field. This means that not only the peripheral UDs, but also the central UDs are likely to appear in weaker field regions with more inclined field orientation and disappear in stronger field regions with less inclined field orientation. This is a natural consequence for peripheral UDs, because they move inward from the penumbra to the umbra. For central UDs, however, the mechanism is less obvious. Further investigations should be possible using the temporal evolution of the magnetic field.

3.4.4. Light Curve

We compared the characteristic light curves of UDs in different field strength regions. Only UDs with lifetimes of $T > 120$ s are selected for analysis in this section. First, UD lifetimes are normalized to unity (0 at their emergence and 1 at their fade-out). A typical light curve is then defined as the average of the temporal variation of the UD brightness. The results are shown in Figure 28. The characteristic light curves of the central and the peripheral UDs (top panels of Figure 28) are consistent with those in Kitai et al. (2007) and Riethmüller et al. (2008). The uniqueness of our analysis lies in the lower four plots in Figure 28. We note a clear dependence of the contrast and the amplitude of the brightness fluctuations on the magnetic field strength. High contrast UDs appear in low magnetic field

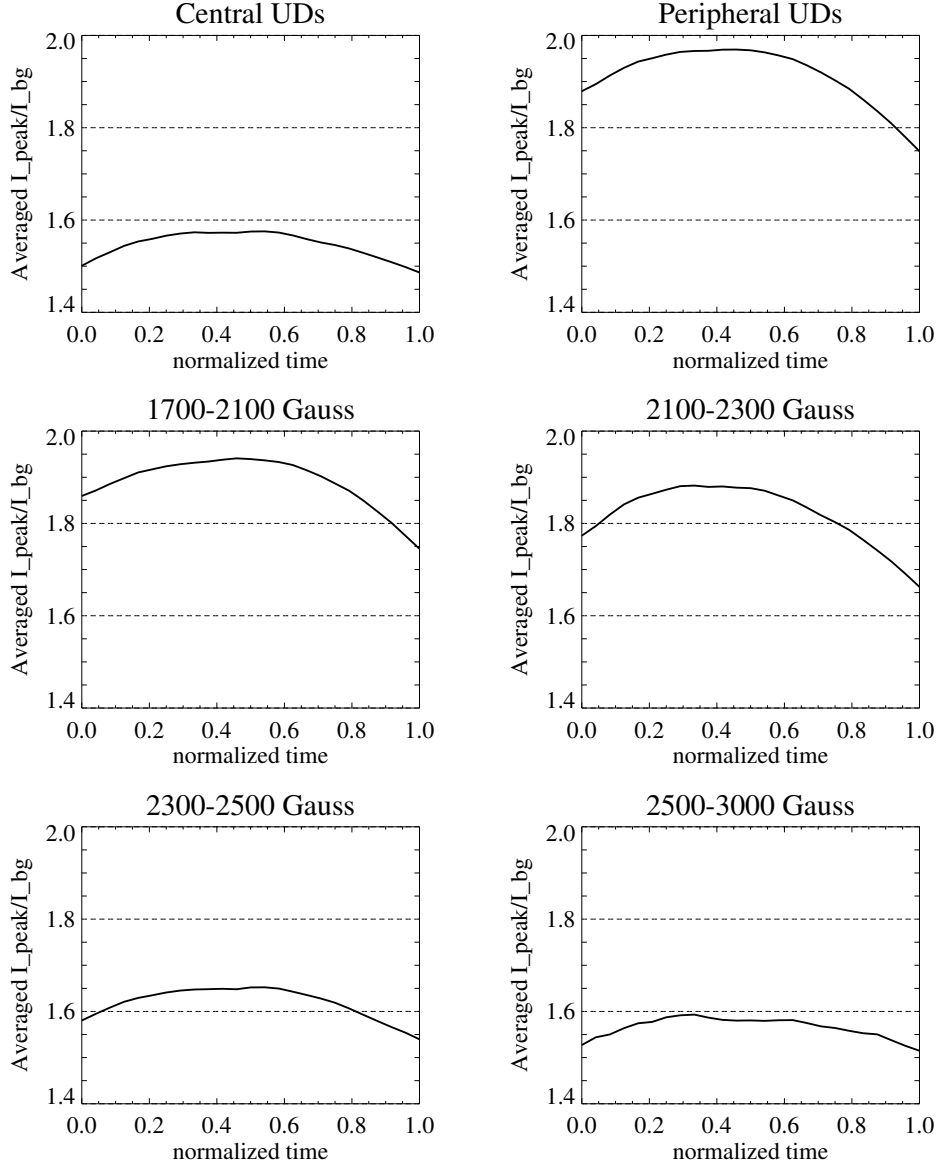


Fig. 28.— Averaged light curves of the central UD's (*top left*), the peripheral UD's (*top right*), UD's born in 1700-2100 G regions (*middle left*), UD's born in 2100-2300 G regions (*middle right*), UD's born in 2300-2500 G regions (*bottom left*), and UD's born in 2500-3000 G regions (*bottom right*).

regions, as was suggested in Section 3.4.2. In the strong field bands, the amplitudes of fluctuations of the brightness ratio get smaller, and the light curves show symmetric brightening and darkening. In the weak field bands, the amplitude of the brightness fluctuations is large, and the light curves show fast brightening and slow darkening.

Another important property of the UD's light curve is its oscillation. We show the light curves of 76 UDs with $T > 1800$ s in Figure 29. The light curves are spaced from each other with a constant offset. We arranged the light curves in order of their field strengths from top to bottom. The bottommost light curve is the brightness of a fixed point in the dark core, which may represent the error fluctuation level. The light curves display oscillatory fluctuations. We should keep in mind that it is very difficult to confirm whether this light curve is the true oscillation in one UD, or the conglomerates of multiple UDs occurring side by side. The identification threshold described in Section 3.3 may also affect the result.

To find the characteristic frequency of the oscillations, a Fourier transformation analysis was performed. The procedure for the Fourier transformation analysis is as follows: first we applied the third order polynomial fit to each light curve, and subtracted it from the original light curve to remove the gradual variations. Second, the IDL routine fast Fourier transformation (FFT) is applied to the subtracted light curves. The amplitude spectrum of the light curve is calculated by taking the absolute value of the Fourier transformed function. Figure 30 shows the amplitude spectra of 76 light curves in color scale. The UDs are arranged in order of their field strength, i.e., UD 0 corresponds to the strongest field (2740 G) and UD 75 corresponds to the weakest field (1880 G). As is shown in Figure 28, the amplitude of fluctuation of the UD brightness is greater in regions with weaker fields than those with stronger fields. The lower frequency components at 1-2mHz (8-16 minutes) are dominant for almost all of the UDs. Note that, since the shortest lifetime of the analyzed UDs is 1800 s, the detectable frequency is limited to larger values than 1.1 mHz. The timescale of 8-16 minutes is consistent with the typical lifetime of UDs. This characteristic frequency was not found in the light curve of the dark core. There is no systematic variation in the amplitude spectra from the weaker magnetized area to the stronger magnetized area. The constant lifetime shown in Figure 24 is consistent with this result.

3.5. Discussion

We analyzed in detail the relationships between the UD's parameters and the magnetic structure. The precise measurement of the magnetic field and the stable high-resolution imaging by the *Hinode* SOT made our analysis possible.

The obtained distributions of the lifetime, the average size, and the proper motion

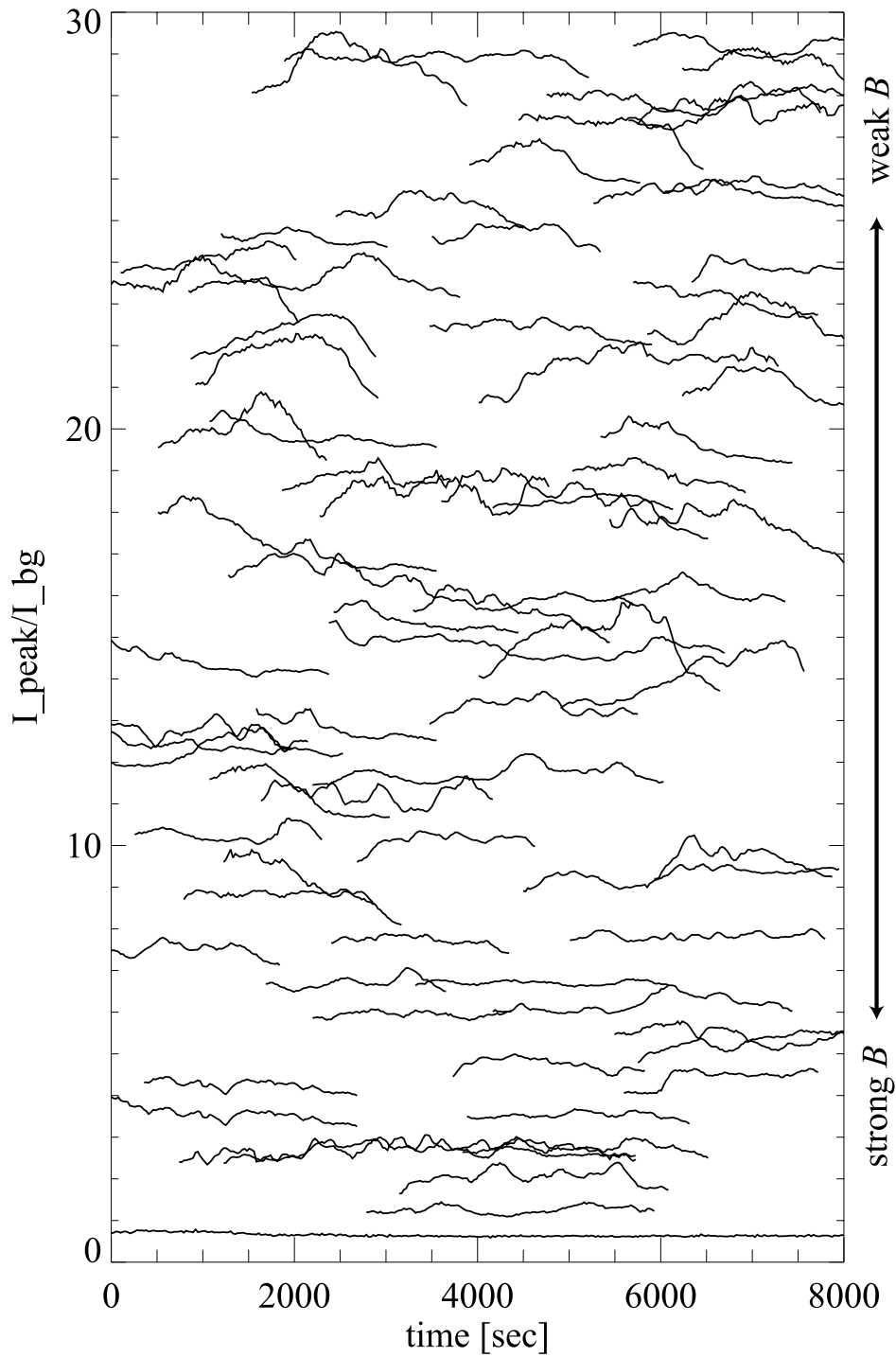


Fig. 29.— Light curves of 76 UD_s with $T > 1800$ s. The light curves are arranged by their field strengths from top to bottom, i.e., the upper curves have the weaker field strength. The light curves are spaced by constant vertical offsets. The bottommost light curve is that of a point in the dark core.

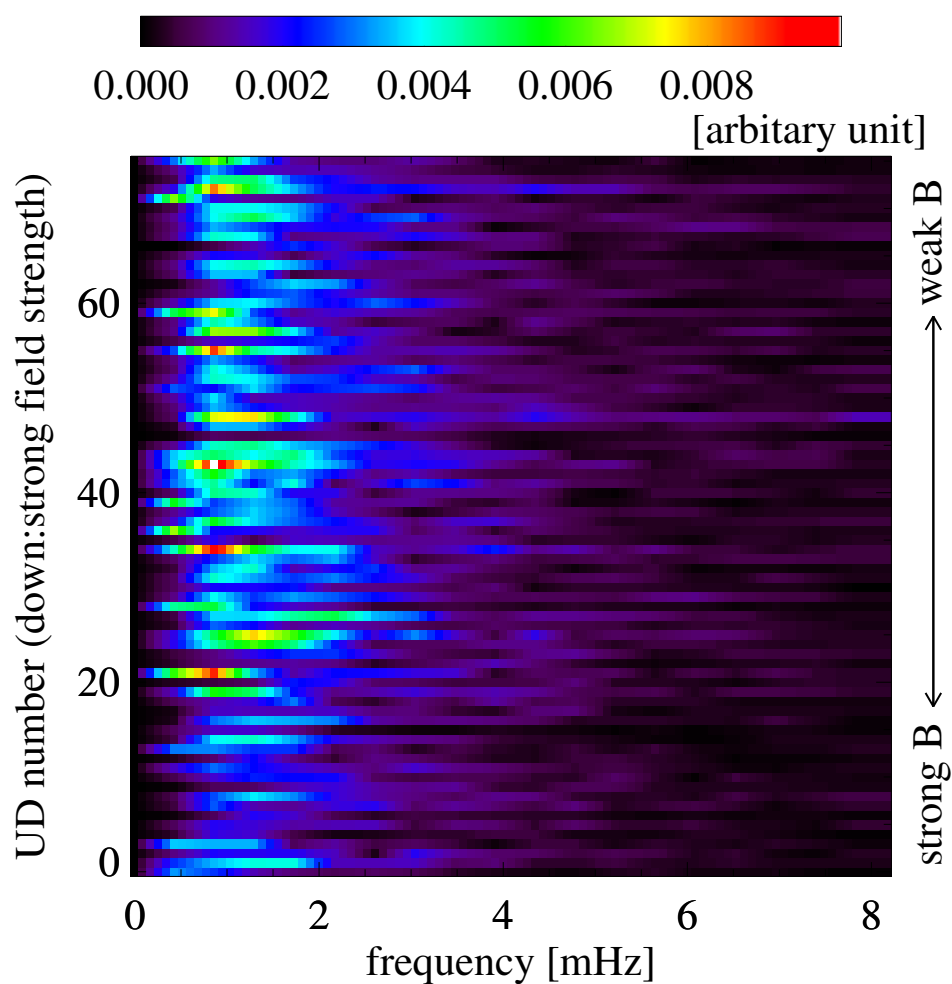


Fig. 30.— Fourier amplitude spectra of the light curves of 76 UD_s. The horizontal axis indicates the frequency, the vertical axis the arrangement of the 76 UD_s (lower positions correspond to stronger fields).

of UDs confirm the performance of our automatic detection algorithm. The averages of each parameter for the central and the peripheral UDs are listed in Table 1. Using these parameters (the lifetime, average size, brightness ratio, velocity amplitude, and velocity orientation) plus three magnetic field components (the field strength, field inclination, and field azimuth), we are able to obtain important correlations between UDs and the magnetic field. The results can be summarized as follows.

1. The lifetimes and average size of UDs show almost no dependence on both the magnetic field strength and field inclination.
2. Highly contrasted UDs come up in the zone near the penumbra, where the magnetic field is weak (~ 2000 G) and inclined above 30° .
3. The velocity amplitudes of the UDs are correlated with the field inclination.
4. The velocity orientations of the UDs in the larger field inclination regions are nearly parallel with field azimuth, while those of the UDs in the smaller field inclination areas have virtually no or random proper motion.
5. The UDs tend to have their origins in regions with weaker, more inclined magnetic fields, and to disappear in regions with stronger, less inclined magnetic fields.
6. There is a negative correlation between the field strength and the occurrence rate of UDs.
7. The analysis of the oscillations of the UD's light curves reveals that low frequency components at 1-2 mHz (8-16 minutes) are dominant for all of the UDs, regardless of the magnetic field strength.

The scatter diagrams shown in Figure 24 have large 1σ errors and the conclusion is not straightforward in our study. The lifetime and average size of UDs are almost independent on the field strength, though there is a hint that the average size at the dark cores is about 20% smaller compared to that at 2000 G. The most significant feature is the positive correlation between the field inclination and UD's velocity amplitude. The gappy model (Spruit & Scharmer 2006; Heinemann et al. 2007) can explain the proper motion of the peripheral UDs. When hot gas ascends along the inclined magnetic field, the gas undergoes radiative cooling and becomes denser. The heavy gas bends the surrounding magnetic field line, increasing their inclination, and then the magnetic field strength at the upper side of the bent field lines is weakened. In order to balance the reduced magnetic pressure, more hot gas rises up from below and causes the apparent movement of the UD. This process occurs repeatedly, and produces the inward migration of peripheral UDs (Scharmer et al. 2008). On

the other hand, this “bending” process will not occur if the field line is vertical. This may be the reason why the central UDs do not show systematic inward migration. The larger correlation coefficient between the field azimuth and the UD’s velocity orientation in the region with larger field inclination provides further evidence of this behavior. However, it is difficult for this idea to explain the fact that the lifetime of central and peripheral UDs are the same. Another possible mechanism is the moving tube model (Schlichenmaier 2002), in which the inward migration corresponds to the footpoint of a rising flux tube. Both models predict the inward migration for UDs in more inclined fields.

Weiss et al. (2002) explained UDs as small scale magnetoconvection modified by the existence of strong magnetic fields. They also suggested that vigorous convection should take place in the weakly magnetized area, which may correspond to light bridges. The small scale convection is a natural consequence of the theoretical model for suppressed eddy motion by strong magnetic fields (Weiss 1981; Blanchflower & Weiss 2002). In our case, the average size of UDs are almost constant ~ 190 km, though there is a hint that the average size in the dark umbral cores ($B > 2600$ G and $i \sim 20^\circ$) is a little smaller. The statistical analysis of the size of UDs is strongly affected by the definition of their size. A more accurate comparison is only possible by a common analysis of both the observed and the simulated umbra smeared using a point spread function consistent with observations. The constant lifetimes we found for UDs is inconsistent with the lifetimes of the simulated UDs by M. Schüssler & A. Vögler (private communication). The mean lifetime of the simulated UDs is 34 minutes for 2000 G sunspots, 28 minutes for 2500 G sunspots, and 25 minutes for 3000 G sunspots, which is significantly longer than the average lifetime of our analysis (7.3 minutes).

The oscillation analysis of the UD’s light curves was first carried out by Sobotka et al. (1997b). However, they used ground-based, seeing-affected observation data. The *Hinode* data are free from such variable atmospheric conditions, which greatly extends the reliability of the oscillation analysis (see Figure 8 in Watanabe et al. 2009). The strong signals at 1-2mHz (8-16 minutes) are commonly found for the UDs with $T > 40$ minutes. As the typical lifetime of UDs is of the order of 10 minutes, this result may show that the successive appearance of UDs causes the oscillatory light curve. We could not find any systematic change in the amplitude spectra of the UDs in the weaker magnetized area and those in the stronger magnetized area. This is consistent with the common lifetime in weak and strong magnetic fields. However, the interpretation of the light curve oscillations of an UD is not straightforward, because they can be caused either by overlapping with adjacent UDs, by an additional heat flux into the UD, or by the period of the oscillatory magnetoconvection.

Recent 3D MHD simulations have successfully simulated the basic characters of UDs. The observational properties of UDs found in this study provide a good test for the theory of UDs, and they should be investigated in future numerical simulations. This strategy will

lead to a more realistic understanding of the structure of sunspots.

REFERENCES

- Beckers, J. M., & Schröter, E. H., *Sol. Phys.*, 1968, 4, 303
- Bharti, L., Jain, R., & Jaaffrey, S. N. A., *ApJ*, 2007, 665, L79
- Blanchflower, S., & Weiss, N., 2002, *Phys. Lett. A* 294, 297
- Chevalier, S. 1916, *Ann. Obs. Astron. Zo-Sè*, 9, B1
- Deinzer, W. 1965, *ApJ*, 141, 548
- Heinemann, T., Nordlund, A., Scharmer, G. B., & Spruit, H. C., 2007, *ApJ*, 669,1390
- Kitai, R., Watanabe, H., Nakamura, T., et al. 2007, *PASJ*, 59, 585
- Parker, E. N., 1979, *ApJ*, 234, 333
- Proctor, M. R. E. & Weiss, N. O. 1982, *Rep. Prog. Phys.*, 45, 1317
- Rempel, M., Schüssler, M., Knölker, M. 2009, *ApJ*, 691, 640
- Riethmüller, T. L., Solanki, S. K., Zakharov, V., & Gandorfer, A. 2008, *A&A*, 233, 243
- Scharmer, G. B., Nordlund, A., & Heinemann, T. 2008, *ApJ*, 677, L149
- Schlichenmaier, R., 2002, *Astron. Nachr.*, 323, 303
- Schüssler, M., & Vögler, A. 2006, *ApJ*, 641, L73
- Sobotka M., Brandt P. N., & Simon G. W. 1997a, *A&A*, 328, 682
- Sobotka M., Brandt P. N., & Simon G. W. 1997b, *A&A*, 328, 689
- Sobotka, M. & Jurčák, J. 2009, *ApJ*, 694, 1080
- Socas-Navarro, H., Pillet, V. M., Sobotka, M., & Vázquez, M. 2004, *ApJ*, 614, 448
- Spruit, H. C., & Scharmer, G. B., 2006, *A&A*, 447, 343
- Tao, L., Weiss, N. O., Brownjohn, D. P., & Proctor, M. R. E., 1998, *ApJ*, 496, L39
- Thomas, J. H., & Weiss, N. O. 2004, *ARA&A*, 42, 517

Tsuneta, S., Ichimoto, K., Katsukawa, Y., et al. 2008, *Sol. Phys.*, 249, 167

Watanabe, H., Kitai, R., Ichimoto, K., et al. 2009, *PASJ*, 61, 193

Weiss, N. O. 1981, *J. of Fluid Mech. Digit. Arch.*, 108, 247

Weiss, N. O., Brownjohn, D. P., Hurlburt, N. E., & Proctor, M. R. E. 1990, *MNRAS*, 245, 434

Weiss, N. O., Proctor, M. R. E., & Brownjohn, D. P. 2002, *MNRAS*, 337, 293

4. Temporal Evolution of Velocity and Magnetic Field in and around Umbral Dots

Abstract

We study the temporal evolution of umbral dots (UDs) using data from the CRISP imaging spectro-polarimeter at the Swedish Solar Telescope. Scans of the magnetically sensitive iron lines at 630 nm were performed under stable and good atmospheric conditions for 71 min with a cadence of 63 s. These data allow us to study the temporal evolution of magnetic and velocity field in and around UD at 0.13'' spatial resolution. From the analysis of 339 UD we draw the following conclusions: (1) Statistically, there seem to be no differences between UD born in the umbra and those detached from penumbral grains. (2) Long-lived UD travel longer distances with slower proper motions. (3) UD show clear hints of upflows, as predicted by MHD simulations. By contrast, we could not find systematic downflow signals associated with UD. Only in very deep layers, we detect localized downflows around UD, but they do not persist in time. (4) We confirm that the magnetic field of UD is weaker and more inclined than that of the surroundings, as reported previously. However, UD that appear in the strong field background or are in the decay phase show enhanced and more vertical fields. (5) There are strong field regions at the migration front of UD detached from penumbral grains, as if their motion were impeded by the strong ambient field. These results are consistent with recent MHD simulations of nearly field-free convection in UD. The effect of the elevation of the optical depth surfaces can explain the observed UD properties.

4.1. Introduction

Umbral dots (UDs) are transient brightenings observed in sunspot umbrae and pores, with typical sizes of 300 km and lifetimes of 10 min (e.g., Sobotka et al. 1997a,b). They cover only 3–10% of the umbral area, but contribute 10–20% of its brightness. For this reason, UD are believed to play a vital role in the energy balance of sunspots (Deinzer 1965; Sobotka et

al. 1993; Moradi et al. 2010).

UDs exhibit systematic proper motions in mature sunspots: those appearing in the central umbral region are static, while UD in peripheral regions move toward the center of the umbra with an average velocity of 1.0 km s^{-1} (Kitai et al. 2007; Riethmüller et al. 2008b). Some UD in the periphery are the continuation of penumbral grains—bright elongated structures at the head of penumbral filaments that move toward the center of the sunspot with speeds of about 0.4 km s^{-1} (Sobotka et al. 1999a; Rimmele & Marino 2006). When the migration front detaches into a circular bright point, the penumbral grain becomes an UD.

It is believed that the mechanism behind UD is convection interacting with the strong vertical field of the umbra, and many observational results support this idea (Riethmüller et al. 2008; Bharti et al. 2010; Watanabe et al. 2010). In the formation phase of sunspots, UD are akin to granules but their apparent motion is more stochastic because of the surrounding magnetic field (Sobotka et al. 1999b). In developed sunspots, UD are small and quiescent due to the stronger suppression of convection.

UD research is entering a new phase in which computer simulations guide observational efforts. The innovative simulations by Schüssler & Vögler (2006) predicted UD with central dark lanes and small localized downflow patches at their ends. A clear detection of those features is important to validate the numerical models, so they have been the target of recent observations. The dark lanes are the result of enhanced density in the upper central part of UD, similarly to the dark cores of penumbral filaments. The hot gas that reaches the surface cools by radiative losses and descends in narrow downflow channels at the end of the dark lanes. Bharti et al. (2007a) found downflows surrounding an UD. Later, Bharti et al. (2007b) observed a dark lane in a big UD. However, the size of this UD was very large ($>1000 \text{ km}$), which suggests that it could actually be a cluster of several UD. Ortiz et al. (2010) reported solid evidence of dark lanes and localized downflow patches based on spectro-polarimetric observations taken at the Swedish 1-m Solar Telescope. The sizes of the dark lanes and downflowing patches found by Ortiz et al. (2010) are near the diffraction limit of the telescope, with the substructures keeping their identity for periods of only a few minutes. These authors also reported enhanced net circular polarization at the site of the downflows.

It is very difficult to study the temporal evolution of UD including magnetic field information because of the need of spectro-polarimetric measurements at high temporal and spatial resolution. To the best of our knowledge, the evolution of the magnetic properties of UD has never been investigated at the required cadence and spatial resolution (but see Sobotka & Jurčák 2009). Ortiz et al. (2010) performed a preliminary analysis of the temporal evolution of six UD, and our work should be considered as a substantial extension of their study. Both the temporal cadence and the polarimetric sensitivity of the measurements

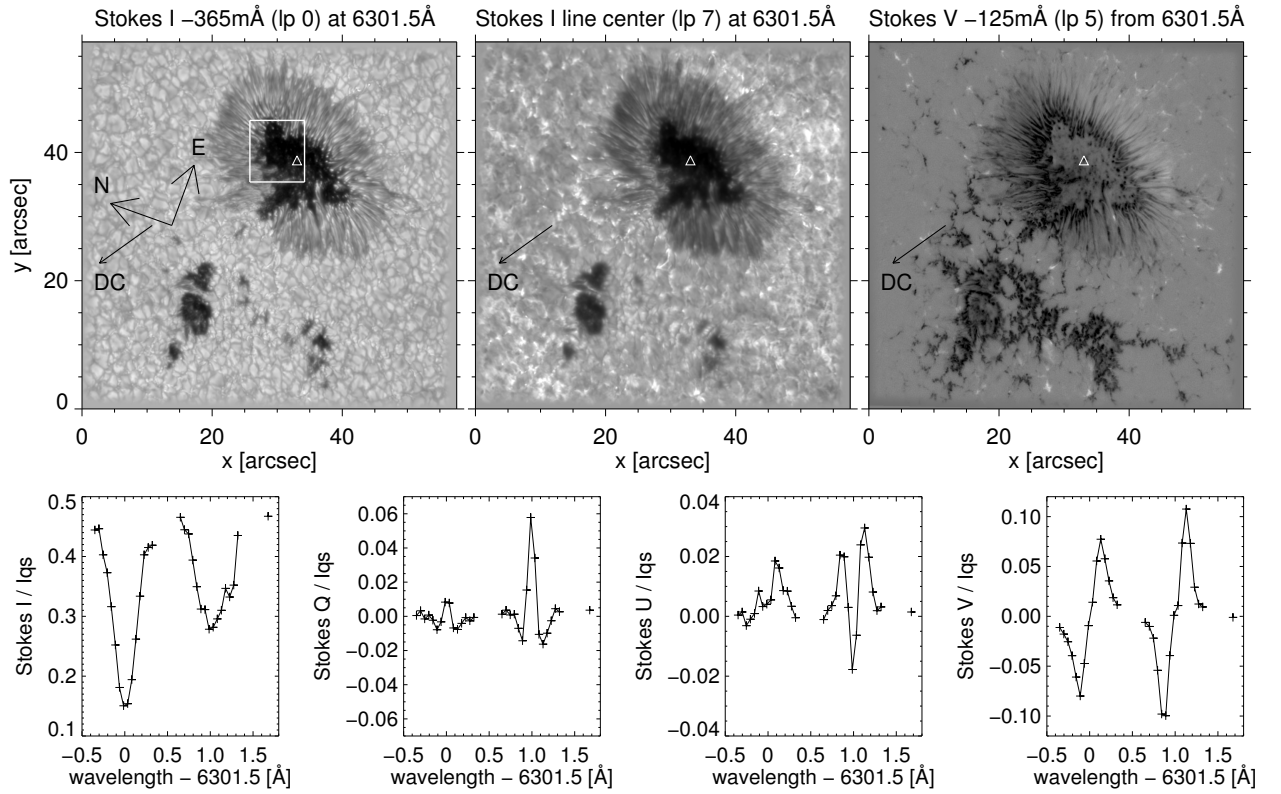


Fig. 31.— Filtergrams from the best scan of the data set, taken at 08:30 UT. The full FOV is shown. From left to right: Stokes I in the blue wing of 6301.5 \AA (line position 0), Stokes I at line center (line position 7), and Stokes V signal in the blue wing (line position 5). The direction to disk center (DC) is displayed with an arrow. The white rectangle indicates the FOV of Figure 32. The bottom row shows the Stokes profiles emerging from the UD marked with triangles in the upper panels. The + symbols indicate the measured signals.

analyzed here are improved with respect to those of Ortiz et al. (2010). The seeing conditions were excellent and stable during the 71 min duration of our time sequence. This unique data set is used here to investigate the temporal evolution of the magnetic and velocity fields in and around UDs.

The paper is organized as follows. The observations are described in Section 4.2, followed by an account of the methods used for the detection of UDs and derivation of the velocity and magnetic information (Section 4.3). In Section 4.4 we quantify how convection is modified in the umbra. In Section 4.5 we describe the evolution of typical UDs, and present the results of our statistical analyses. Finally, based on these results, we discuss the physical properties of UDs in Section 4.6.

4.2. Observations and Data Reduction

The observations were obtained with the CRisp Imaging Spectro-Polarimeter (CRISP) at the Swedish 1-m Solar Telescope (SST, Scharmer et al. 2003) on La Palma, Spain. CRISP is based on a dual Fabry-Pérot interferometer similar to that described by Scharmer (2006). The incoming light is modulated by two liquid crystal variable retarders cycling through four states and then analyzed by a polarizing beam splitter in front of two narrow-band cameras. The narrow-band cameras record orthogonal polarization states to minimize seeing-induced crosstalk. CRISP has a third camera for wide band imaging. All the cameras operate at 35 frames per second and take exposures of 17.1 ms. The synchronism between them is ensured by an external optical chopper.

CRISP was used to measure the four Stokes profiles of the magnetically sensitive Fe I 6301.5 and 6302.5 Å lines, each sampled at 15 wavelength positions in steps of 48 mÅ from -350 to $+322$ mÅ. Line positions 0–14 sample the 6301.5 Å line, while positions 15–29 correspond to the 6302.5 Å line. In addition, a continuum wavelength point (6303.2 Å, line position 30) was measured. We recorded 9 accumulations per modulation state, resulting in 36 exposures per wavelength position. The total time for a complete wavelength scan of the two Fe I lines plus the continuum point was 32 s. Another 30 s were needed to scan the Ca II line at 854.2 nm (not used in this paper). Thus, the temporal cadence of the Fe I scans is 63 s.

The CRISP etalons are mounted in tandem on a telecentric beam. The separation of the cavities of the high resolution etalon sets the wavelength of the transmission profile. This is not strictly the same over the whole field of view (FOV) because the surface cannot be infinitely flat, producing random wavelength shifts (cavity errors) across the FOV. Intensity fluctuations, introduced by cavity errors in the presence of a spectral line, were removed from

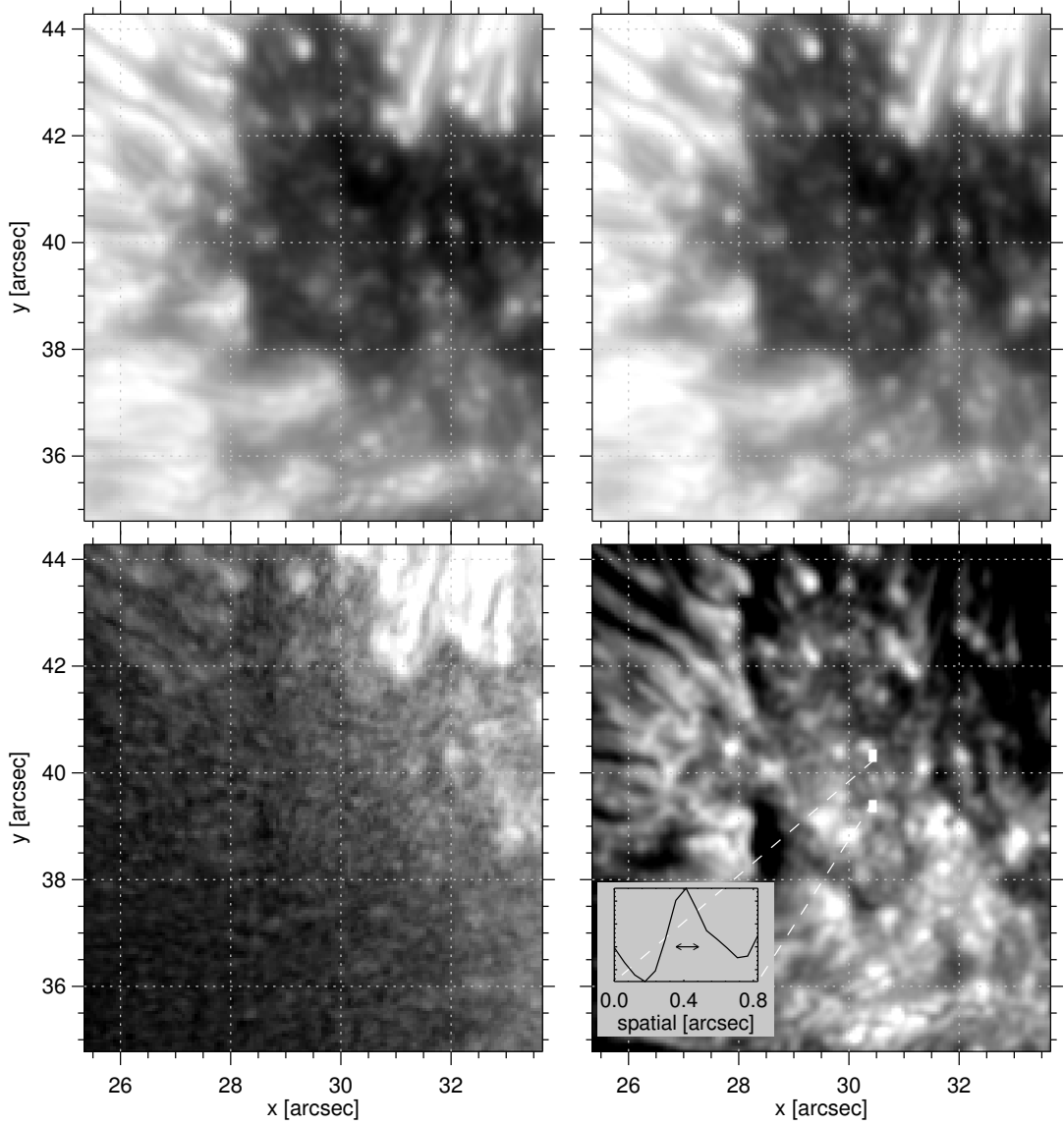


Fig. 32.— Close-up of the region indicated by the white box of Figure 31. *Clockwise, starting from upper left:* intensity in the blue wing of 6301.5 \AA (line position 0), continuum intensity at 6303.2 \AA (line position 30), CP map, and LP map. The spatial intensity profile of a point-like feature (corresponding to an UD) is shown in the CP map. The length of the arrow in the plot is $0''.13$ (equal to the diffraction limit).

the flat-field images in a similar way as described by Schnerr et al. (2011). Their flat-fielding scheme computes a cavity-error-free averaged quiet-sun profile, which is removed from the flats on a pixel-by-pixel basis. This average is obtained by summing many hundreds of exposures acquired by moving the telescope in circles around the disk center. The difference between the Schnerr et al. (2011) scheme and ours is that we applied a polarization-free flat for all the four Stokes states taken at one wavelength position. The average CRISP transmission profile has a Gaussian core (FWHM of 64 mÅ at 6300Å) and wide Lorentzian wings. This profile reduces the line core depth of the Fe I lines by about 20%.

We also corrected the data for spectral intensity gradients introduced by the CRISP prefilter. The prefilter correction can be decomposed in two contributions, an average prefilter shape and a term that accounts for pixel-to-pixel deviations:

$$P(\lambda, x, y) = P_g(\lambda) + dP(x, y). \quad (14)$$

The second term of the equation is included in the flat-field correction. To obtain the global prefilter shape (P_g), our estimate of the averaged quiet-sun profile is compared to the FTS atlas convolved with the CRISP transmission profile. The prefilter is assumed to have a Lorentzian profile which is multiplied with a polynomial term to account for asymmetries:

$$P_g(\lambda) = \frac{1}{1 + [2(\lambda - \lambda_0)/w]^{2N_{\text{cav}}}} (1 + p_0\lambda + p_1\lambda^3), \quad (15)$$

where λ_0 is the central wavelength of the prefilter, w is the FWHM of the prefilter, N_{cav} is the number of cavities of the filter ($N_{\text{cav}} = 2$ in this case), and p_0 and p_1 are the coefficients of the polynomial. A least-squares-fitting scheme (Markwardt 2009) was used to compute the prefilter parameters, minimizing the differences between the observed and modeled curves. This correction curve was then applied to all Stokes parameters.

The theoretical diffraction limit of the telescope around 6300 Å is 0".13, and the image pixel size is 0".059. To improve the spatial resolution, we used the adaptive optics system of the SST and the Multi-Object Multi-Frame Blind Deconvolution image restoration technique (MOMFBD; van Noort et al. 2005). The MOMFBD algorithm considers all frames taken in one scan (31 wavelength points \times 4 modulation states \times 9 accumulations \times 3 cameras) to remove image distortions from the individual filtergrams.

Under enhanced differential-seeing conditions, residual rubber sheet distortions are present between the narrow-band images of the same scan even after MOMFBD restoration. This effect appears when the size of the patches used to divide the images for the MOMFBD processing (here 128 \times 128 pixels) is larger than the spatial scale of the atmospheric distortion (or iso-planatic patch). To attenuate their influence in our measurements, we employed an extra step in the processing following an idea from V. Henriques (private

communication). The wide-band images were used twice in a MOMFBD restoration in the following manner:

1. All the frames were combined to produce the reference anchor image.
2. The frames were separated in sets associated with each wavelength position and modulation state, resulting in one restored wide-band image per wavelength and modulation state.

The second set of wide-band images was not used for wavefront sensing, i.e., they did not contribute to the determination of the PSF in the MOMFBD calculations. The state-dependent restored wide-band images were compared with the anchor wide-band image to remove the residual rubber sheet deformations in the individual filtergrams. This correction is applied prior to the demodulation of the data to ensure almost perfect co-alignment between the 4 liquid crystal states that form the Stokes maps at any wavelength position. Moreover, the method achieves almost perfect co-alignment between the wavelength positions to ensure the integrity of the Stokes profiles over the FOV.

After restoration, the images were demodulated and corrected for instrumental polarization using the telescope model developed by Selbing (2010). For details, see van Noort & Rouppe van der Voort (2008). In addition, we corrected small residual crosstalks from Stokes I to Q , U , V by forcing the polarization to be zero in the far line wings. All the Stokes profiles were normalized to the average quiet-sun continuum intensity (I_{qs}) computed for each time step. The typical noise levels in Stokes Q , U , and V are 1.9×10^{-3} , 2.7×10^{-3} , 1.8×10^{-3} of the continuum intensity, respectively.

We followed the main sunspot of NOAA active region 11024 from 08:05 UT to 09:16 UT on 6 July 2009. The observed FOV covered an area of $58'' \times 57''$. At that time, the solar heliographic coordinates of the spot were 23°N and 31°E (heliocentric angle of 35° , $\mu=0.82$). During the observations the atmospheric conditions were excellent and stable. Figure 31 shows selected filtergrams from one of the best scans (08:30 UT) and the four Stokes profiles recorded at the position of an UD.

Figure 32 shows a close-up of the umbra and the inner penumbra on the disk-center side of the spot. The maps of mean linear polarization (LP) and circular polarization (CP) degree were calculated as

$$\text{LP} = \frac{\int [Q^2(\lambda) + U^2(\lambda)]^{1/2} / I(\lambda) d\lambda}{\int d\lambda} \quad (16)$$

$$\text{CP} = \frac{\int |V(\lambda)| / I(\lambda) d\lambda}{\int d\lambda} \quad (17)$$

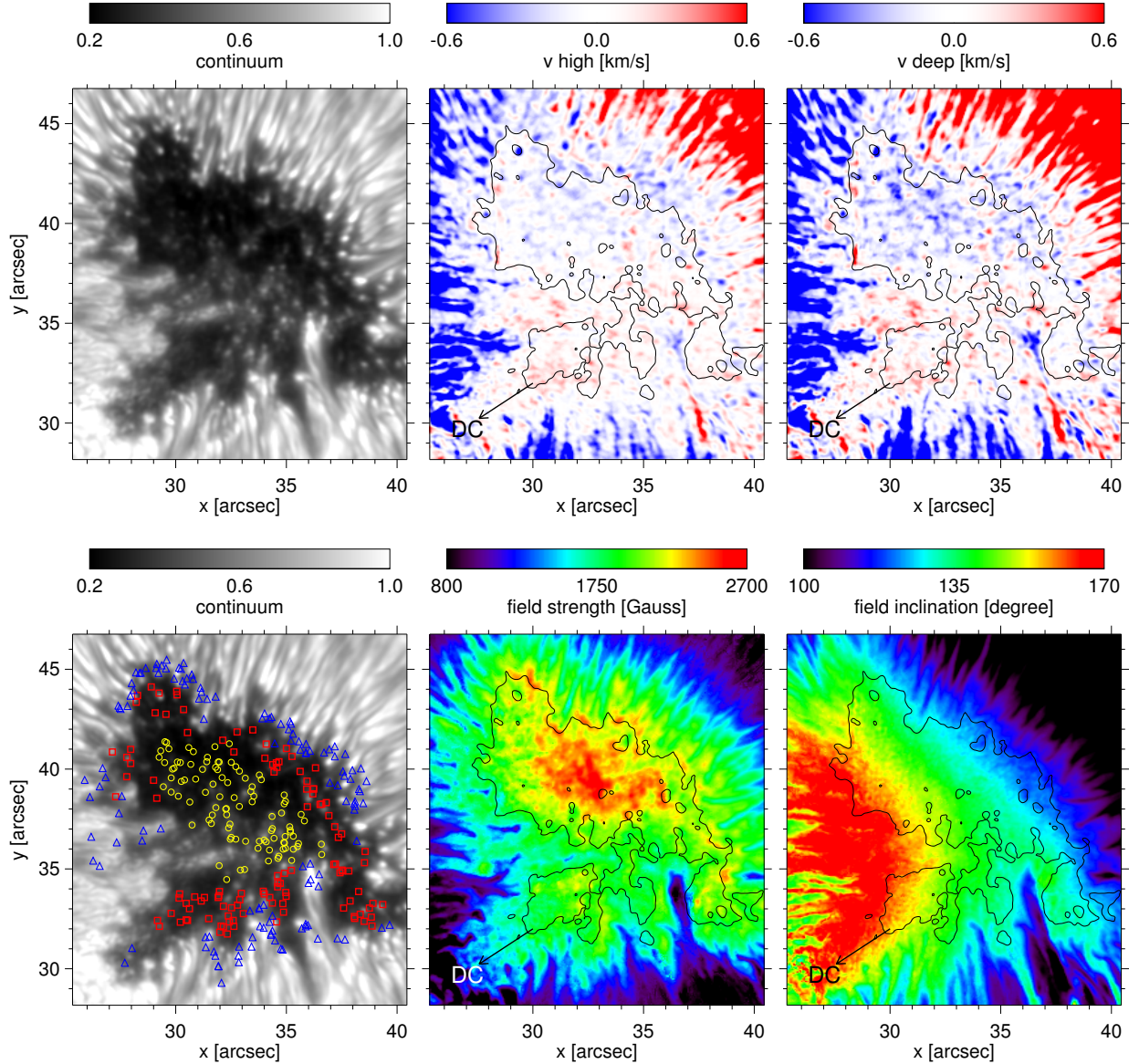


Fig. 33.— Physical parameters derived from the observed Stokes profiles. Shown here is the scan with best seeing conditions, taken at 08:30 UT. The top panels, from left to right, display the continuum intensity map and two bisector maps sampling high (v_{high}) and deep (v_{deep}) photospheric layers. Negative velocities (blue) represent upflows along the line of sight, and positive velocities (red) mean downflows. The bottom panels, from left to right, show the appearance positions of all the detected UDs (yellow circles are central UDs, red squares are peripheral UDs, blue triangles are grain-origin UDs), and the field strength and LOS field inclinations derived from the SIR inversion. The black contours indicate continuum intensities of $0.4 I_{\text{qs}}$. The arrows mark the direction to the disk center (DC).

The LP map shows larger signals towards the limb due to projection effects. Most of the fine scale structures seen in the LP and CP maps coincide with UDs. Figure 32 clearly demonstrates that

1. The first and last continuum images of the scan are perfectly aligned and do not show distortions in spite that they were taken about 30 s apart (top row), demonstrating the good performance of the MOMFBD processing.
2. Almost all UDs in the umbra keep their brightness, size, and position during the line scan (top row), that is, the scan time is shorter than the dynamic timescale of UDs.
3. The smallest features visible in the maps (UDs, dark cores of penumbral filaments) are only slightly larger than the diffraction limit of the SST. They are best seen in the CP map because of the higher contrast.

We believe this is one of the best UD data sets ever obtained, because the spatial resolution is superb ($0.13''$), the seeing conditions were excellent, and high precision spectro-polarimetry was achieved with good temporal cadence (63 s). The main disadvantage of Fabry-Pérot systems, namely, the non-simultaneous acquisition of spectral information, can be well neglected because UDs evolve in longer time scales than the scan time.

4.3. Data analysis

In this section we describe the methods we have used to detect and track UDs, as well as the line bisector calculations and Stokes inversions performed to derive their velocities and magnetic fields.

4.3.1. Detection and Categorization

For the statistical study of UDs, it is convenient to adopt an automatic detection algorithm (Sobotka et al. 1997a; Bharti et al. 2010). However, we have implemented a manual procedure because, even under the very stable seeing conditions of our observations, the image quality still shows an unavoidable amount of residual fluctuation which might compromise the performance of automatic algorithms.

The procedure works as follows. First we inspect the continuum movie to identify the frame of appearance of each UD. The position of the UD is then tracked by clicking on the screen until it disappears. After going through the temporal sequence, we run the movie backward in time to check the consistency. When an UD splits or merges with another

structure, the bigger component is the one that continues to be tracked and the smaller component is selected separately as a new entity. In some cases, UDs show recurrence at the same position. If the recurrent UDs appear within an interval of 3 frames (≈ 3 min), we consider them as one single entity.

UDs evolving from penumbral grains are also studied. In this case, the detection starts from the frame in which the tip of the penumbral grain detaches from the filamentary structure. Sometimes these UDs are connected to the penumbral grains through a faint tail, but they become more isolated and roundish as they move towards the umbra.

This method has allowed us to obtain the trajectories of 339 UDs. According to their origin and place of birth, we categorize them into three groups. UDs located in the central part of the umbra are called “central UDs” (98 samples out of 339 UDs), UDs located in the peripheral area are called “peripheral UDs” (112 samples), and UDs evolved from penumbral grains are called “grain-origin UDs” (129 samples). The peripheral area is an ~ 1 – $2''$ annular region adjacent to the umbra-penumbra boundary. It is known that central UDs are static while peripheral and grain-origin UDs show a systematic inward motion toward the center of the umbra (Ewell 1992; Sobotka et al. 1997b). About 40% of the 339 UDs we have detected did not appear or disappear within the interval covered by the observations. Therefore, their lifetimes could not be computed.

Table 2: Average photometric properties of UDs

Parameter	Central	Peripheral	Grain-origin
Number	98	112	129
Lifetime ¹ [min]	19	18	17
Proper motion [km s ⁻¹]	0.19	0.31	0.49
Brightness ratio	1.46	1.50	1.87
Diameter [km]	358	342	469

In the lower-left panel of Figure 33 we show the appearance position of all 339 UDs. The yellow circles indicate central UDs, the red squares peripheral UDs, and the blue triangles grain-origin UDs. Table 2 lists their average properties over all measurements. The average lifetime is about 18 min. This is relatively long compared to the values reported in previous works (e.g., Riethmüller et al. 2008b), probably because our manual detection is capable of including fainter UDs. The average proper motion speed is defined as the distance between the positions in the first detected frame and the last frame divided by the time interval. No projection correction is applied. The brightness ratio is the UD intensity (the maximum intensity within a ± 2 pixel area) relative to the intensity of the dark background (I_{db}). We use the “dark background (db)” —the region surrounding the UD but excluding the UD

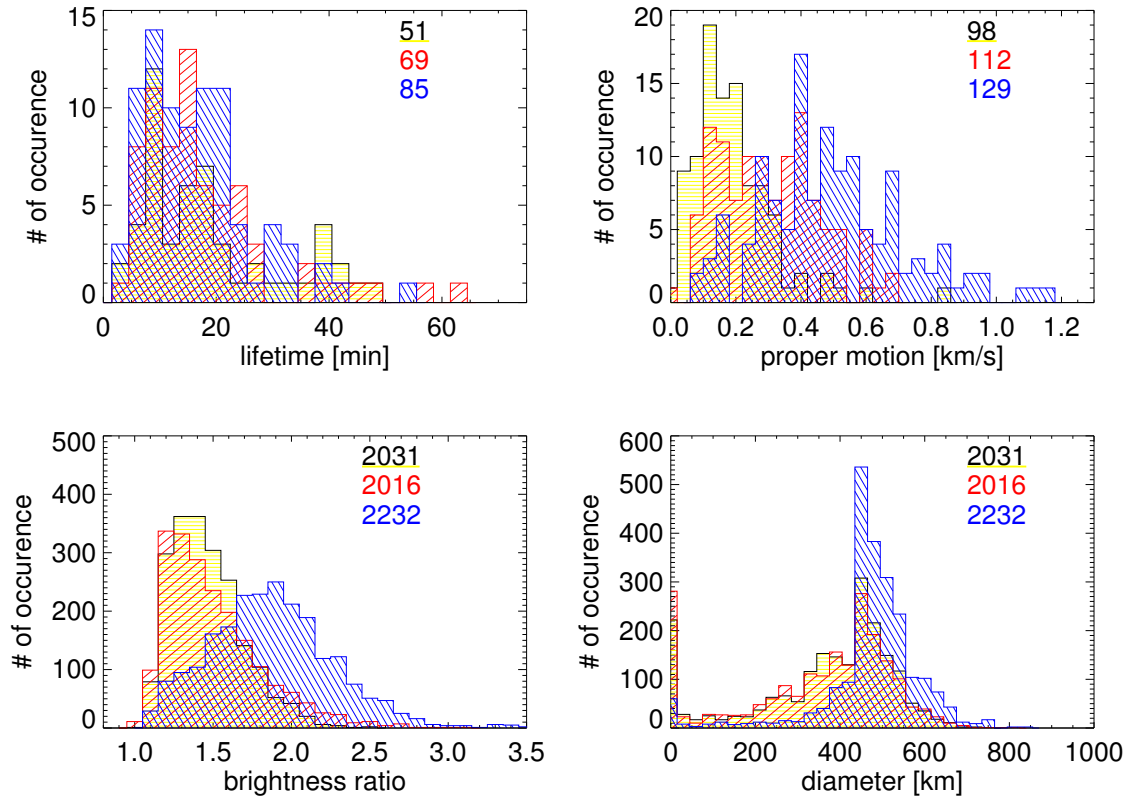


Fig. 34.— Histograms of UD lifetime (upper left), average proper motion speed (upper right), brightness ratio (lower left), and diameter (lower right). Central UDs are displayed with black bars filled with yellow color, peripheral UDs with red color, and grain-origin UDs with blue color. In the upper-right corner of each histogram, the number of measurement points of the three categories (black with yellow underline: central UD, red: peripheral UD, blue: grain-origin UD) are shown.

itself—as a local reference. I_{db} is the mean intensity of pixels over a $2'' \times 2''$ area centered in the UD whose intensity is darker than the average minus 0.5σ . Here, σ represents the standard deviation of the intensity within that area. The UD diameter is calculated as the average distance in eight radial directions along which the intensity is brighter than $1.2 I_{\text{db}}$, or as the distance to the closest inflection point. A similar method was adopted in Watanabe et al. (2009a). There are some instances of zero diameter, which means that the UD intensity was darker than $1.2 I_{\text{db}}$. As the brightness ratio and diameter are calculated for every time step within the UD lifetime, we get in total 6279 values for these parameters.

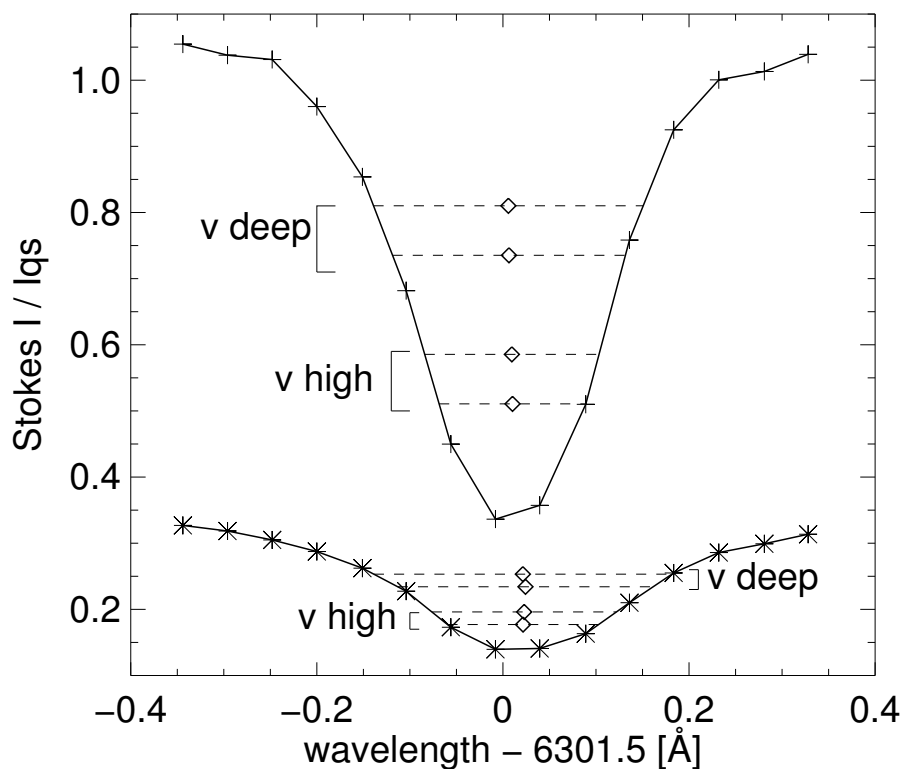


Fig. 35.— Intensity profiles emerging from the tip of a penumbral grain (pluses) and from an UD (asterisks). The diamonds indicate the bisector positions at intensity levels of 10% and 23% (v_{high}), and 49% and 62% (v_{deep}).

Figure 34 shows histograms of the four parameters (lifetime, average proper motion speed, brightness ratio, and diameter). The histograms of central and peripheral UDs are similar except that the latter show faster proper motions. The histograms of grain-origin UDs differ from those of central and peripheral UDs: grain-origin UDs have the fastest proper motions, the brightest intensity contrasts, and the largest diameters.

4.3.2. Derivation of Velocities: Line Bisectors

The mean wavelength position of the two line wings at a certain intensity level is called the line bisector (Figure 35). Bisectors are used to estimate the height variation of the line-of-sight velocity, because different intensity levels sample different atmospheric heights (see e.g., Tritzschler et al. 2004; Ortiz et al. 2010). The 0% intensity level represents the line core, while 100% means the local continuum.

We calculate bisectors only for Fe I 6301.5 Å because the red wing of Fe I 6302.5 Å is strongly blended with the telluric O₂ 6302.8 Å line (see the Stokes *I* profile in Figure 31). The Fe I 6301.5 Å line is less affected by blending, although its far blue wing (intensity levels > 70%) sometimes show influence of molecular lines in the darkest umbral areas (Martinez Pillet & Vazquez 1993), which results in a systematic blueshift there. For this reason we calculated four bisector positions at intensity levels of 10%, 23%, 49%, and 62%, avoiding bisectors close to the continuum. Each bisector position results from a linear interpolation between the relevant intensities in the observed line profile and the corresponding wavelength positions. To reduce noise, two bisector levels are averaged, leading to two bisector maps which will be called v_{high} (10% and 23%) and v_{deep} (49% and 62%) (see Figure 35).

Following Title et al. (1989), we apply a subsonic Fourier filter to the temporal sequence of v_{high} and v_{deep} to suppress disturbances with horizontal speeds larger than 4 km s⁻¹, which are mostly due to *p*-modes and the residual temporal noise. In the umbra, a large spatial-scale velocity pattern (≈ 5000 km) corresponding to the *p*-mode oscillations is observed. This pattern is removed by the filter. We use an edge apodization of 10% in space and time to avoid the propagation of boundary errors. The effect of the subsonic filtering is demonstrated in Figure 36. The dominant redshift signal in the right-hand side of the umbra at $(x, y) \sim (37'', 37'')$ (upper panel) is absent in the subsonic filtered image (lower panel). However small local variations in the map, which coincide with the UD's positions, keep their identity even after the subsonic filtering.

The zero velocity wavelength is determined by averaging the filtered v_{high} over umbral pixels with intensities below $0.4 I_{\text{qs}}$. This is done for each of the 68 frames of the sequence. The appearance of the v_{high} and v_{deep} maps is similar, but the root-mean-square (rms) fluctuations are larger in v_{deep} . The typical rms values over the umbra are 0.15 km s⁻¹ for v_{high} and 0.20 km s⁻¹ for v_{deep} . The rms variations are significantly larger when the data are not filtered. Thus, the filtering is essential to provide a good velocity reference, and also to remove the large velocity offsets induced by the *p*-mode oscillations. This is particularly important when dealing with small velocities such as those observed in UDs.

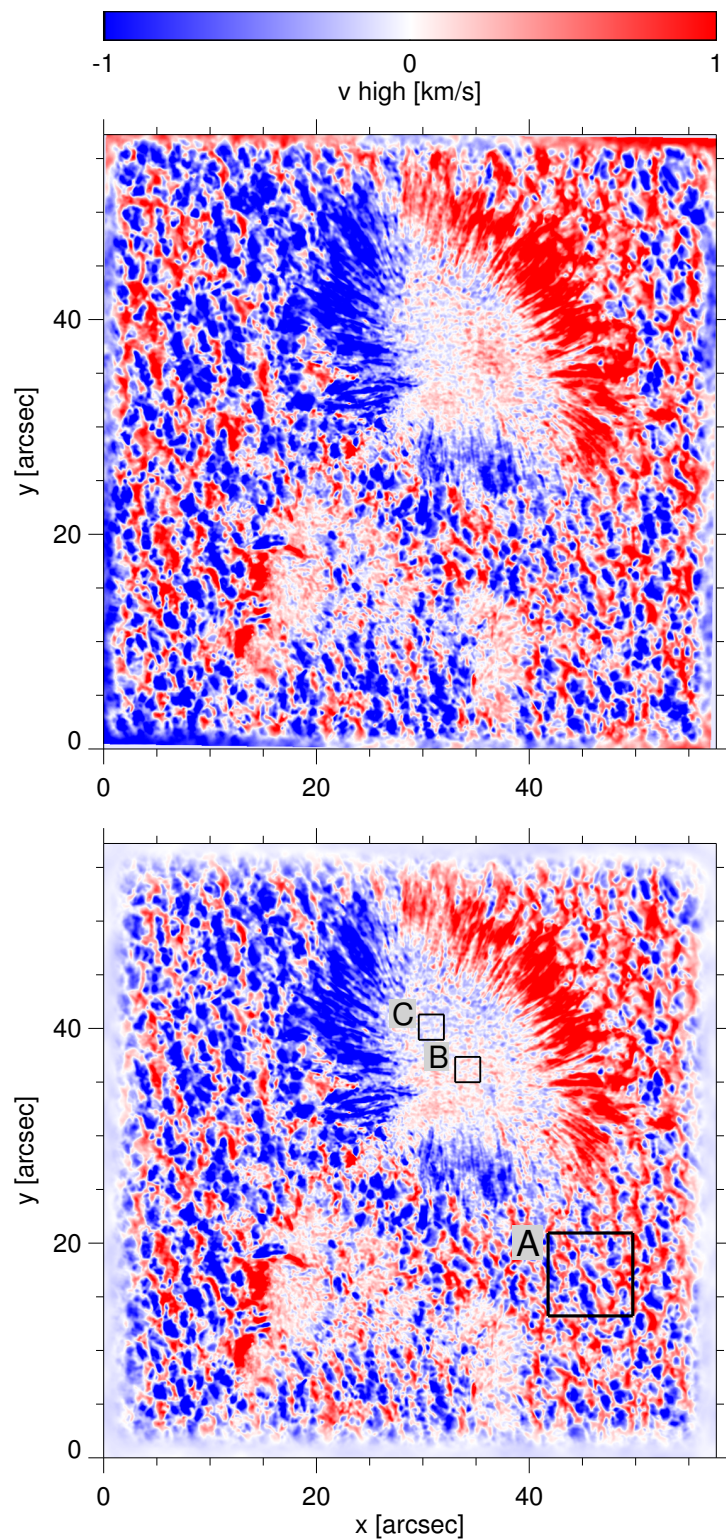


Fig. 36.— Original v_{high} map observed at 08:31 UT (top) and subsonic filtered map (bottom). Negative velocities (blue) mean upflows along the line of sight, and positive velocities (red) mean downflows. The regions marked A–C will be studied in Section 4.4.2.

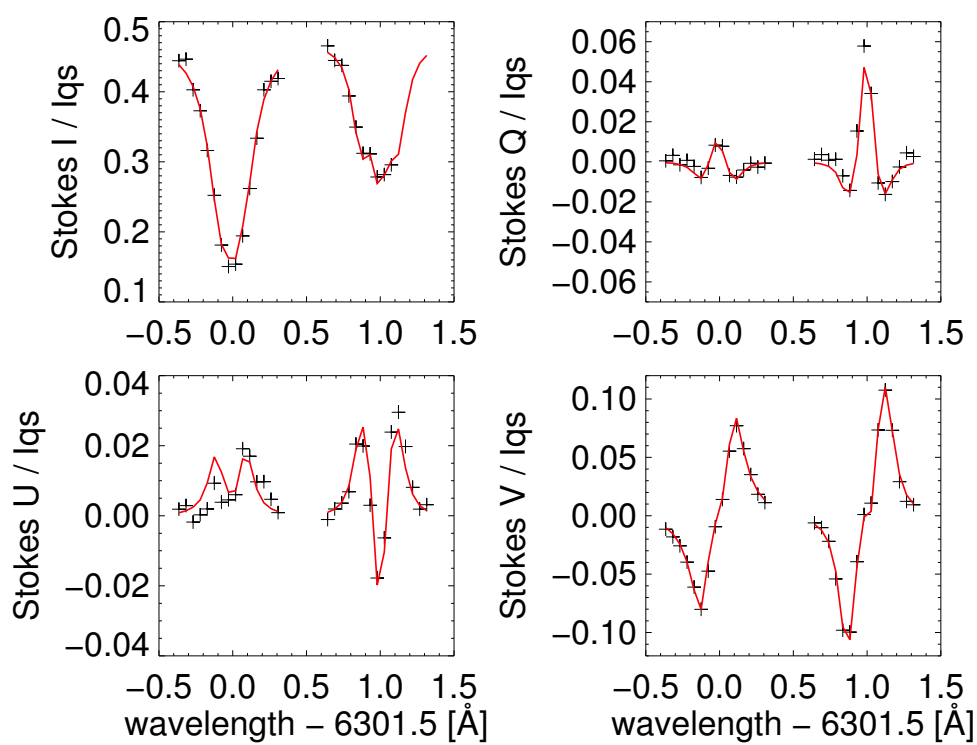


Fig. 37.— Stokes profiles observed at the position of an UD (marked with a triangle in Figure 31) and best-fit profiles returned by SIR (black and red, respectively).

4.3.3. Derivation of Magnetic Properties: Stokes Inversion

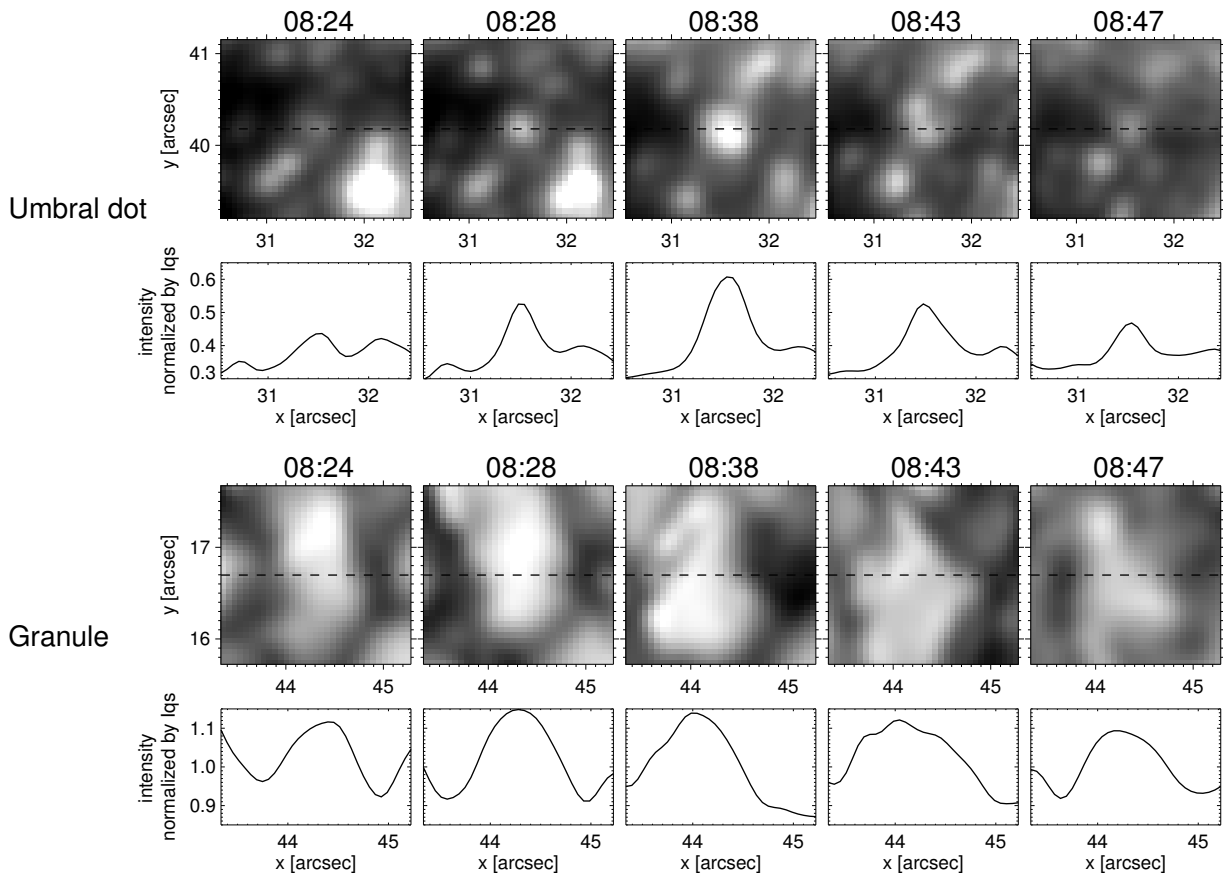


Fig. 38.— Temporal evolution of an UD (top panels) and a quiet Sun granule (bottom). Displayed are continuum intensity maps for an area of $2'' \times 2''$ with a temporal cadence of ≈ 4 min. The (x, y) coordinates coincide with those of Figure 31. An intensity cut along the dashed line plotted at the center of the FOV is shown below each image. The times are given in UT.

We determine the magnetic properties of the umbra by inverting the observed Stokes profiles with the SIR code (Stokes Inversion based on Response functions; Ruiz Cobo & del Toro Iniesta 1992). The two lines are fitted simultaneously for every pixel of the 68 scans. The telluric O_2 blend in the red wing of the Fe I 6302.5 Stokes I profile is excluded from the fit.

The inversion is carried out in terms of a one-component model atmosphere with constant (i.e., height-independent) magnetic fields and velocities, which is sufficient to explain the relatively symmetric Stokes profiles observed in the sunspot umbra (see Figure 37). Zero stray-light contamination and unity magnetic filling factors are assumed. The inver-

sion returns 9 free parameters: the three components of the vector magnetic field (strength, inclination, and azimuth), the line-of-sight velocity, the microturbulent velocity, and the temperature at 4 nodes. The initial guess model used to start the inversion is the hot umbral model of Collados et al. (1994).

Sample maps of field strength and field inclination are displayed in Figure 33. The inclination angles refer to the line of sight which has not been transformed to the local reference frame, varying from zero for fields pointing away from observer to 180° for fields pointing to it. Smaller value of field inclination means more inclined fields, while larger field inclination means more vertical fields. We also note that the line-of-sight velocities returned by the inversion agree well with the bisector velocities obtained from the 6301.5 \AA line.

4.4. Convection in the Umbra

In the solar photosphere, the presence of strong magnetic fields suppresses convective energy transport. This is why sunspots are dark and cool compared to the quiet Sun, which is covered by convective cells called granules. However, convection is not entirely suppressed even in the umbra. As a matter of fact, UDs are the manifestation of a modified convective pattern in the umbra. The properties of this pattern still need to be determined. Here we study how the characteristics of convection differ between the quiet Sun and the umbra, paying special attention to the morphology of the convective cells and the correlation between brightness and velocity.

4.4.1. Morphology

Figure 38 illustrates the morphological evolution of a central UD and a granule. The images cover an area of $2'' \times 2''$. First we notice that the UD ($\approx 0.3''$) is much smaller than the granule ($\approx 1.0''$; c.f., Roudier & Muller 1987). Second, UDs are relatively isolated whereas granules are closely packed with narrow ($\approx 0.3''$) intergranular lanes. Third, the intensity profile of granules is flat-top, usually with intensity depressions in the middle. A granule loses its identity (or disappears) by fragmentation or by merging with neighboring granules. On the other hand, the intensity profile of UDs has a Gaussian shape, and they disappear mostly by fading out.

Both UDs and granules exhibit a turbulent character: although the structures shown in Figure 38 keep their identities over 23 min, they change their brightness, barycenter, and shape in timescales of only a few minutes. According to previous works (e.g., Bahng & Schwarzschild 1961; Hirzberger et al. 1999), the average lifetime of granules is 6–9 min,

which is slightly shorter than that of UDs.

4.4.2. Brightness vs Velocity

The strong correlation between brightness and line-of-sight velocity in granular convection is well known. Bright areas (i.e., granules) show upflows, while dark areas (the intergranular lanes outlining the granules) harbor downflows. This is illustrated in the top panel of Figure 39. Although the bisector velocities (v_{high} and v_{deep}) are not corrected for projection effects, they mostly represent vertical flows because horizontal flows in the umbra are usually weak and randomly directed.

In the umbra, in addition to UDs, there exist diffuse areas with enhanced brightness. These areas may correspond to a convective pattern similar to (but weaker than) that of the quiet Sun, with UDs being another manifestation of the same pattern occurring at positions where convection is more vigorous. To test this possibility, we have examined the correlation between brightness and velocity in the umbra: if bright structures are the result of convection, then they should preferentially be associated with upflows. The middle and bottom panels of Figure 39 show scatter plots for the selected umbral areas B and C (Figure 36). Area B is close to the light bridge, and area C represents the central umbra. In these areas, we find the same tendency of upflows in bright regions and downflows in dark regions for the scan taken at 08:30 UT (left column), yet with weaker correlation. However, the correlation does not persist in time and scans obtained a few minutes apart show the opposite behavior (right column of Figure 39). Thus, we cannot confirm the existence of a global convective pattern in the umbra using the present data. As we will see later, the situation is different for UDs.

4.5. Umbral Dots

In this Section we give a detailed description of the evolution and statistical properties of individual UDs.

4.5.1. Case Studies

We select five UDs (UD#A–UD#E) whose locations are indicated in Figure 40. All of them were observed from their appearance to their disappearance. Movies of the temporal evolution of these UDs are available in the electronic journal.

In Section 4.5.1, another two UDs from one of the best scans of the time series are

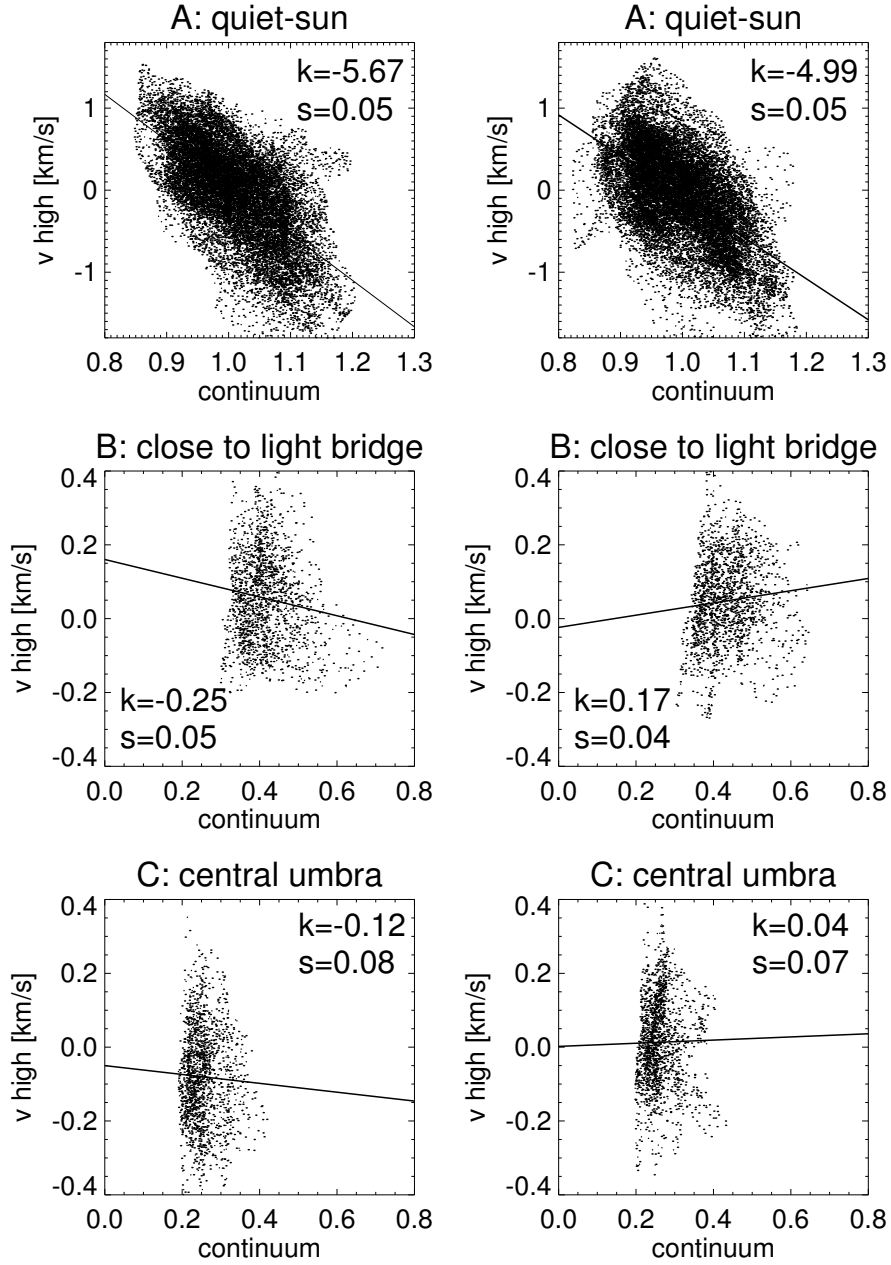


Fig. 39.— v_{high} vs continuum intensity for selected umbral and quiet Sun areas using the line scans taken at 08:28 UT (left column) and 08:39 UT (right column). Negative velocities represent upflows along the line of sight. The positions of areas A–C are indicated in Figure 36. k represents the slope of the best-fit straight line and s is its 1σ uncertainty.

considered. We use them to demonstrate the existence of localized downflow patches around UDs in deep photospheric layers.

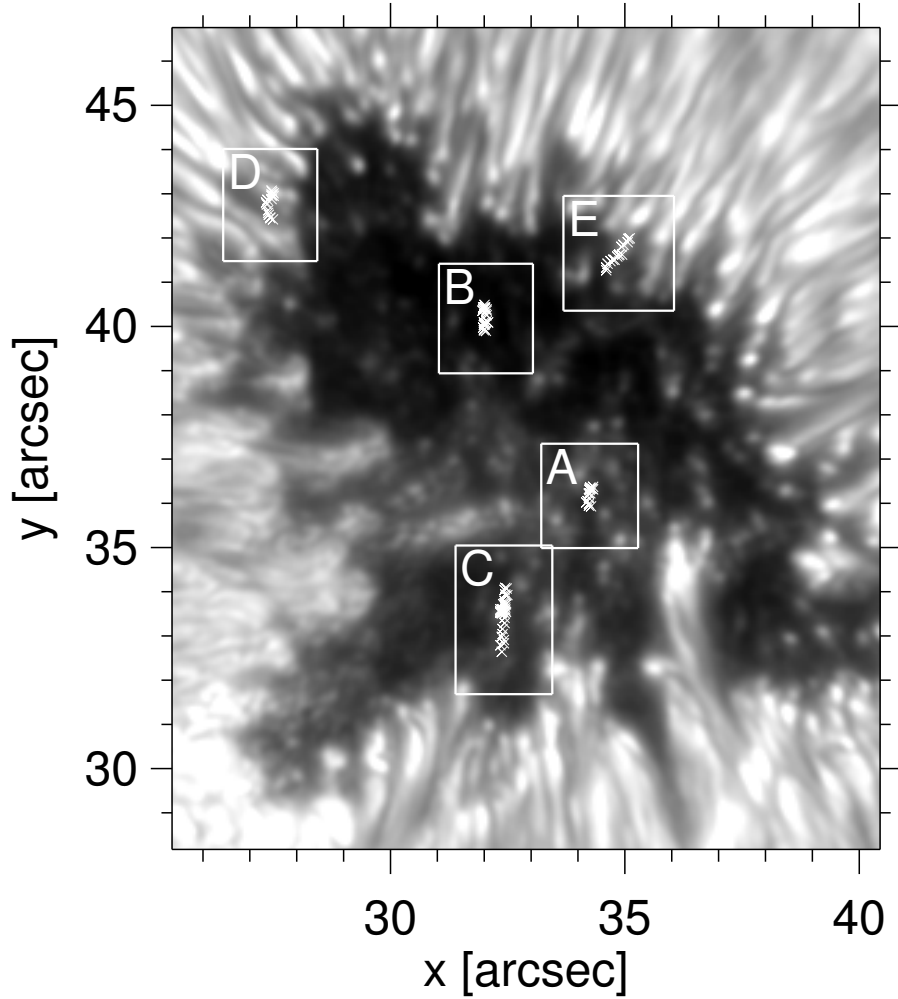


Fig. 40.— Position of selected UDs (A, B: central UD, C: peripheral UD, D, E: grain-origin UD). The background image shows the continuum intensity at 08:30 UT. The cross symbols indicate the trajectories of the UDs.

Typical Central UD

According to our visual inspection, more than 70% of the central UDs do not show any flow field perturbation, i.e., no upflows or downflows are detected. Similarly, magnetic field perturbation associated with central UDs are usually not visible or very small. 17% of the central UDs undergo merging or splitting events with neighboring UDs.

The temporal evolution of one typical central UD (UD#A) is displayed in Figs. 48 and 49. Figure 48 show the temporal evolution of UD#A starting 2 frames before its appearance ($T=0$ s corresponds to the appearance) and ending 2 frames after it disappeared ($T=1006$ s corresponds to the disappearance). In the left column of Figure 49, light curves at the UD's position (solid line) and of the dark background (dashed line) are depicted. The dark background is the average over the dark area within the FOV of the images in Figure 48 (pixels with intensity darker than the average -0.5σ). The right column of Figure 49 shows spatial profiles along the x direction at y positions co-moving with the UD. The Gaussian peaks at $x \approx 34''.3$ in the continuum plot corresponds to the UD.

UD#A was born in a diffuse bright region, then increased in brightness ($0\text{s} < T < 377\text{s}$), and finally merged with a neighboring UD ($755\text{s} < T < 1006\text{s}$). As can be seen in both images and plots, there are no clear upflow or downflow signals associated with this UD. During most of its lifetime, it seems to be located in a patch with enhanced redshifts, whose morphology and amplitude do not correlate with UD#A's evolution. In Figure 48, a local reduction of the field strength at the position of the UD can be seen during $0\text{s} < T < 629\text{s}$, and the UD appears to gradually merge with a pre-existing weak field patch at the $+y$ side. More inclined fields (smaller Δi) are observed during $62\text{s} < T < 692\text{s}$. The amplitude of the magnetic field perturbations is very small, $\approx 50\text{ G}$ for the field strength and $\approx 1^\circ$ for the field inclination.

Distinct Central UD

Figures 50 and 51 show the temporal evolution of a distinct central UD (UD#B). This UD is distinct because of its prominent intensity and upflow. UD#B is born in a very dark area within the umbra and the continuum intensity becomes quite high as it evolves ($566\text{s} < T < 880\text{s}$). A second smaller intensity peak appears during $1069\text{s} < T < 1321\text{s}$. Finally it fades in a diffuse bright background with no detectable intensity peak. There is a significant upflow associated with the continuum intensity enhancements. The maximum upflow of $\approx 0.3\text{ km s}^{-1}$ (v_{high}) is observed at $T=629\text{s}$. A reduction of the field strength of the order of 50 G co-spatial with the UD is observed in the first half of its lifetime. After $T=755\text{s}$, the reduction region of field strength disappears and the UD collides with a pre-existing strong field region. Sometimes there is a small spatial displacement ($\approx 0.2''$) between peaks in brightness and the patches of reduced field strength. The field inclination shows no clear variations.

Typical Peripheral UD

Peripheral UDs are born in the peripheral region of the umbra, where the continuum intensity is brighter and the field lines are more inclined. The most significant property of peripheral UDs is that they show a systematic proper motion toward the center of the umbra (see Table 1). Our visual inspection reveals that 55% of the detected peripheral UDs show upflows, but no systematic magnetic field perturbations. For example, 13% of peripheral UDs show a reduction of field strength, while 16% of them are associated with enhanced fields.

Figures 52 and 53 show the temporal evolution of a typical peripheral UD (UD#C). The inward migration of this UD is very clearly seen in the accompanying animation. The migration speed is $\approx 1.1 \text{ km s}^{-1}$ during $0 \text{ s} < T < 503 \text{ s}$, and almost zero during $503 \text{ s} < T < 1635 \text{ s}$. In the final stages of its life ($1635 \text{ s} < T < 2390 \text{ s}$), the UD migrates again with a speed of 0.5 km s^{-1} . The origin of UD#C is a diffuse bright area within the umbra. It shows three brightness peaks: the first at $T=377 \text{ s}$, the second at $T=1132 \text{ s}$, and the third at $T=1761 \text{ s}$. The same recurrent pattern is observed in the velocity field. The blueshift peaks three times in accordance with the brightness peaks. The peak v_{high} values are -0.11 km s^{-1} ($T=377 \text{ s}$), -0.07 km s^{-1} ($T=1005 \text{ s}$), and -0.003 km s^{-1} ($T=1886 \text{ s}$). A hint of redshifts is seen in both v_{high} and v_{deep} after $T=2076 \text{ s}$, but the connection with UD#C is not clear. The redshift patches at $(x,y)=(32.4'', 33.8'')$ appear to exist at the same location even before the birth of UD#C, and these downflows seem to be enhanced by the collision of UD#C.

The magnetic field shows a complex distribution. A patch of reduced field strength ($\approx 100 \text{ G}$) appears and migrates inward to the umbra during $377 \text{ s} < T < 1069 \text{ s}$. However, another patch of increased field strength can be observed right next to it at $(x,y) = (32''.5, 33''.5)$. This patch already exists from $T=-125 \text{ s}$, when there is no corresponding brightness enhancement in the continuum intensity map. Then as the UD#C moves inwards, the patch of stronger fields also moves inward but with slower speed (0.5 km s^{-1} during $0 \text{ s} < T < 755 \text{ s}$). The patch disappears when the UD's brightness decreases at around $T=2202 \text{ s}$. The field inclination gets more inclined especially during the migration.

Typical Grain-Origin UDs

Grain-origin UDs are characterized by inward migration to the umbra center and high intensity contrasts (Table 2). The perturbations associated with these UDs are more clearly visible than those of central and peripheral UDs. Our analysis demonstrates that 77% of the grain-origin UDs harbor upflows, while 40–50% show weaker strengths and more inclined fields. Grain-origin UDs with enhanced field strength and more vertical fields are not common (less than 20%). Sometimes there are patches of both reduced and increased field strengths

associated with the UD locations.

In this section we describe the evolution of two typical grain-origin UDs: one from the disk center side of the spot and the other from the limb side.

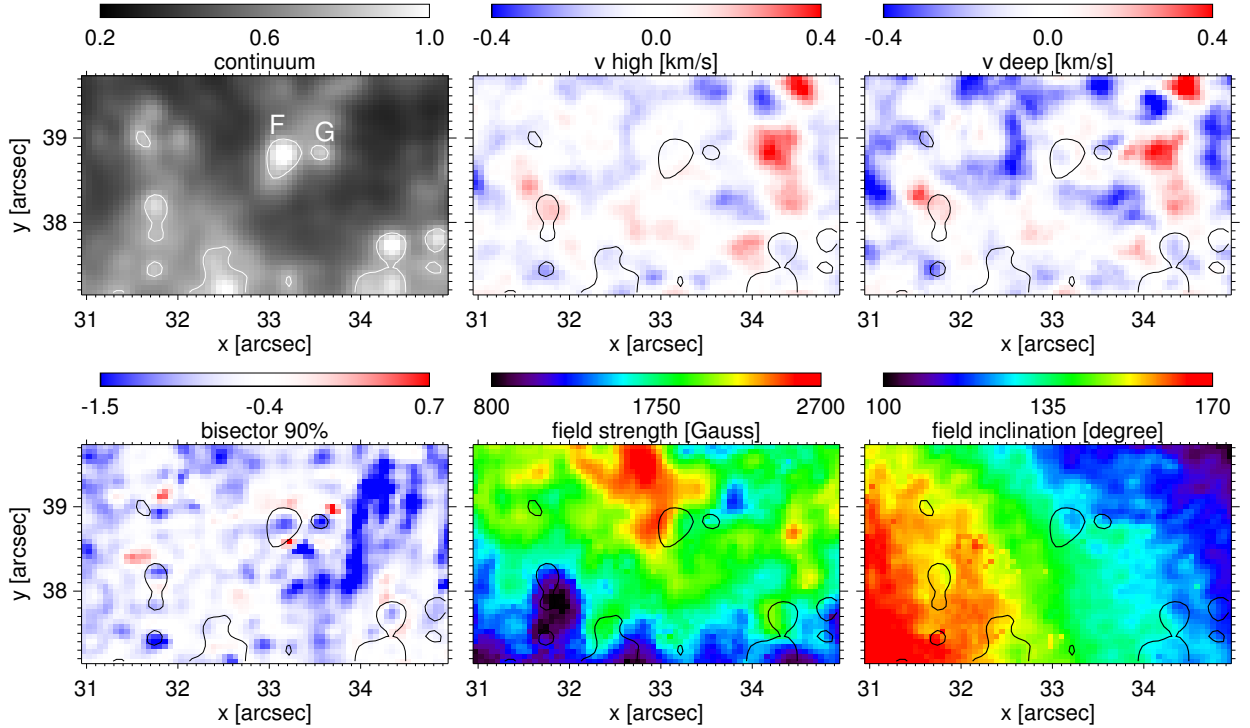


Fig. 41.— Close-up images of the central area of the umbra from the line scan taken at 08:30 UT. *Clockwise, starting from top left:* continuum intensity, v_{high} , v_{deep} , field inclination, field strength, and bisector velocity at the 90% intensity level. Negative velocities represent upflows along the line of sight. The white and black contours show continuum intensities of $0.4 I_{\text{qs}}$.

Figures 54 and 55 show the temporal evolution of the disk-center side case (UD#D). It evolves from a filamentary structure into a circular shape. UD#D follows an unusual trajectory: generally, grain-origin UDs move along the extension line of penumbral grains, but UD#D changes its motion to the $-y$ direction after it detaches from the grain. The continuum intensity decreases a bit during $188\text{s} < T < 314\text{s}$, and then increases again. A decreasing upflow is continuously observed. The strongest upflow of $>0.45\text{ km s}^{-1}$ appears at the tip of the penumbral grain around $T = 62\text{ s}$. There is a broad region of downflows at the leading front of the UD (see for example the image at $T=566\text{ s}$), and finally the UD disappears by colliding into the downflow region. UD#D is located at the boundary of weak and strong field regions. As it moves along the $-y$ direction, the boundary also evolves as if the leading edge of the UD was always blocked by the strong field walls ($440\text{s} < T < 817\text{s}$).

The field inclination gets more inclined during $0 \text{ s} < T < 503 \text{ s}$, but in latter phases the UD does not change the pre-existing field inclination distribution.

Figures 56 and 57 show the temporal evolution of a limb side case (UD#E). UD#E is detached from a penumbral grain and moves along the extension line of the grain with an apparent speed of about 0.7 km s^{-1} . In the case of limb-side UDs, flow field perturbations are hard to detect. Indeed UD#E shows no upflow or downflow. We attribute this to a line-of-sight effect working against the field-aligned flows in the inclined magnetic field. The field inclination shows no perturbation. A local reduction of field strength is observed to the left of the UD position throughout its lifetime.

UDs with Downflow Patches

Ortiz et al. (2010) found evidence of localized downflow patches associated with bright UDs in a pore. A bisector analysis of the Fe I 6301.5 line showed that these downflows are strongest in deep atmospheric layers. We tried to perform a similar analysis including temporal evolution, but this proved difficult because:

1. In the darkest parts of our umbra, the Fe I 6301.5 Å bisectors at high intensity levels ($> 70\%$) appear to show systematic blueshifts.
2. Near the continuum, the quality of the bisector maps is very dependent on the seeing conditions.

Therefore in this section we show examples of downflows extracted from the best scan in our data set, taken at 08:30 UT, focussing on relatively bright areas around the center of the umbra.

Figure 41 shows a region of about $4'' \times 2''$ centered at $(x, y) = (33'', 38.5'')$. The two UDs marked in the upper left panel (UD#F and UD#G) exhibit no clear velocity signals in the v_{high} and v_{deep} maps, but prominent upflows in the bisector map at the 90% intensity level (lower left panel). Next to those upflows, localized downflow patches can be seen on the $+y$ and $-y$ sides of the UDs. The blueshift at the center of UD#F amounts to -1.3 km s^{-1} , and the downflow patches have speeds of 0.16 km s^{-1} ($+y$ side) and 0.75 km s^{-1} ($-y$ side). Similarly, the blueshift at the center of UD#G is -1.5 km s^{-1} , and the downflows to the top right attain 0.68 km s^{-1} . Also the $-y$ side of UD#G is relatively redshifted (-0.17 km s^{-1}). The downflow patches have an approximate size of $0''.2$. In these UDs we do not see the central dark lanes predicted by Schüssler & Vögler (2006).

The magnetic field around UD#F and UD#G is slightly weaker and more inclined than

in the surroundings. When we inspect the continuum movie, these two UDs are both in the peak phase of their brightness.

4.5.2. Statistical Properties

In this section we describe the statistical properties of 339 UDs (98 central, 112 peripheral, and 129 grain-origin UDs). The histograms of lifetime, average proper motion speed, brightness ratio, and diameter are shown in Figure 34.

4.5.3. Statistics of Bisector Velocities around UDs

Figure 42 shows the histograms of average v_{high} and v_{deep} around UDs (average over UD's position ± 3 pixels, so over a total area of 7×7 pixels), including all temporal steps within their lifetimes (i.e., 6279 samples). In each panel, the center-of-gravity value of the histogram is shown. If the UD do not have systematic flows, the histogram would show a symmetric distribution about 0 km s^{-1} . This is the case for central UDs, with only a slight inclination to negative velocities (upflows). On the other hand, a tail extending to strong upflows is seen in the histograms for peripheral and grain-origin UDs. The asymmetric distribution is more prominent in the case of grain-origin UDs as compared with peripheral UDs.

A similar result is visible in Figure 43, which shows the average variation of the flow velocity as a function of radial distance from the center of the UD. Upflows decreasing with distance are found in the region close to the UDs (< 5 pixel), although the 1σ fluctuation is large. The largest upflow coincides with the peak brightness position, with average value of -0.13 km s^{-1} (v_{deep}). Smaller upflows decreasing with distance are found for v_{high} , too (not shown). Within a distance of 10 pixels ($0.6''$) from the UD center, we always find upflows on average, but no downflows.

4.5.4. Statistics of Magnetic Parameters around UDs

The local perturbations of field strength (ΔB) and field inclination (Δi) are obtained by subtracting a smoothed version of the map from the original map itself. The smoothing is done with a boxcar average of width 20×20 pixels (870 km), which is significantly larger than the typical size of the UDs (see Figure 34).

Figure 44 shows the histograms of ΔB and Δi averaged over UD's position ± 3 pixels. To our surprise, the histogram of ΔB indicates that the UD magnetic field is a bit stronger

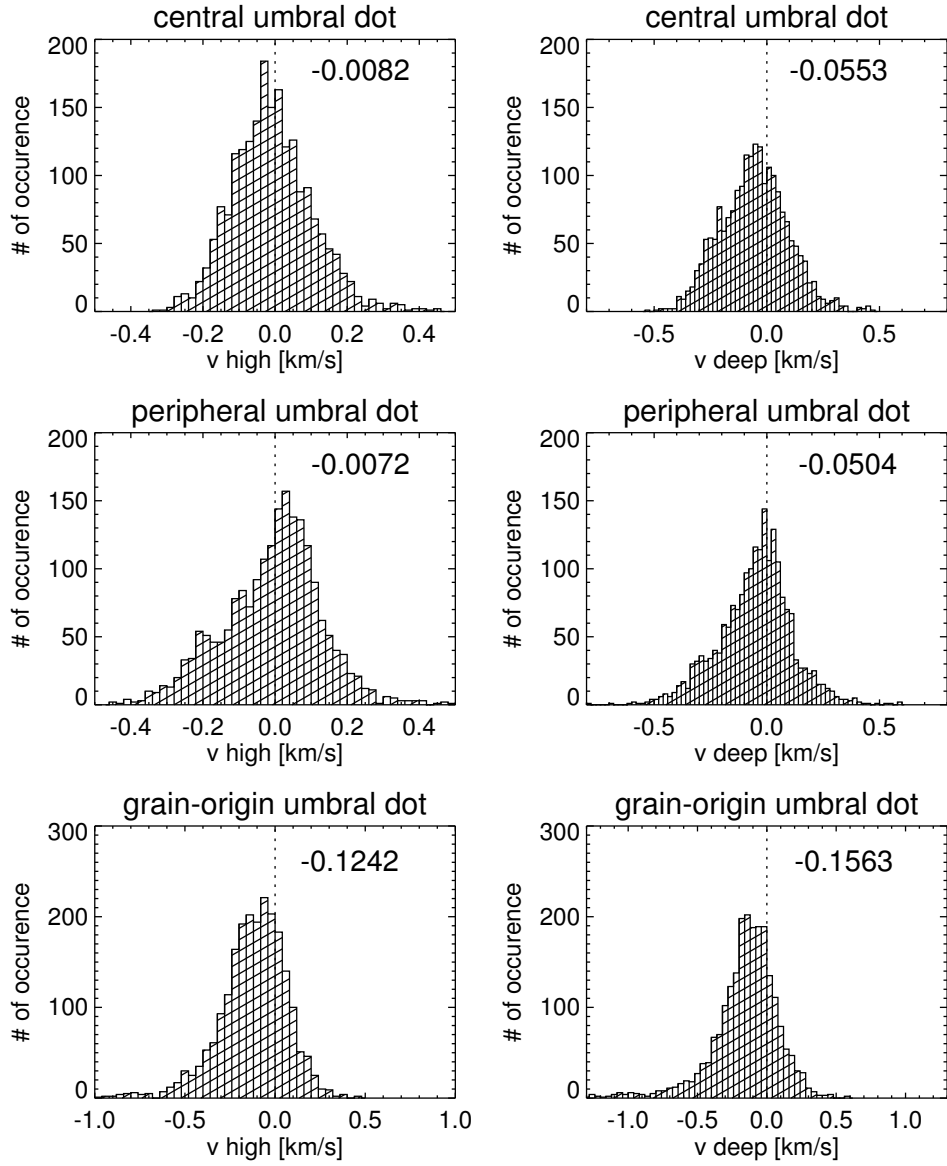


Fig. 42.— Histograms of average v_{high} and v_{deep} around UD. The center-of-gravity of each histogram is given in the upper right corner.

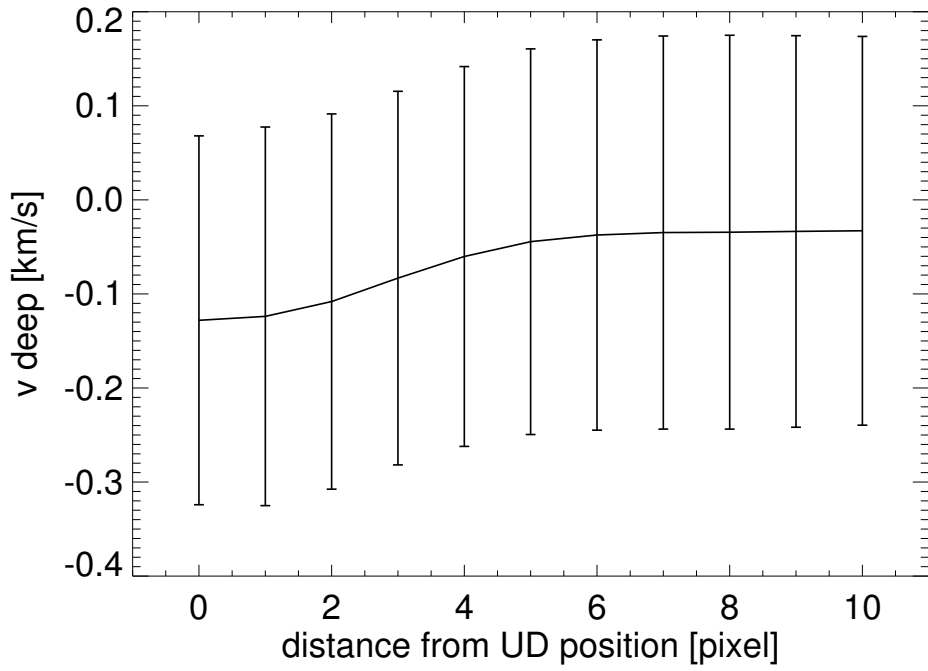


Fig. 43.— Average value of v_{deep} as a function of distance to the closest UD position in all categories. Negative means upflow. The calculation is performed in the umbra, where the continuum intensity is darker than $0.4 \times I_{\text{qs}}$. One pixel corresponds to $0''.06$. The error bars show the $1\text{-}\sigma$ fluctuation within 1 pixel bins.

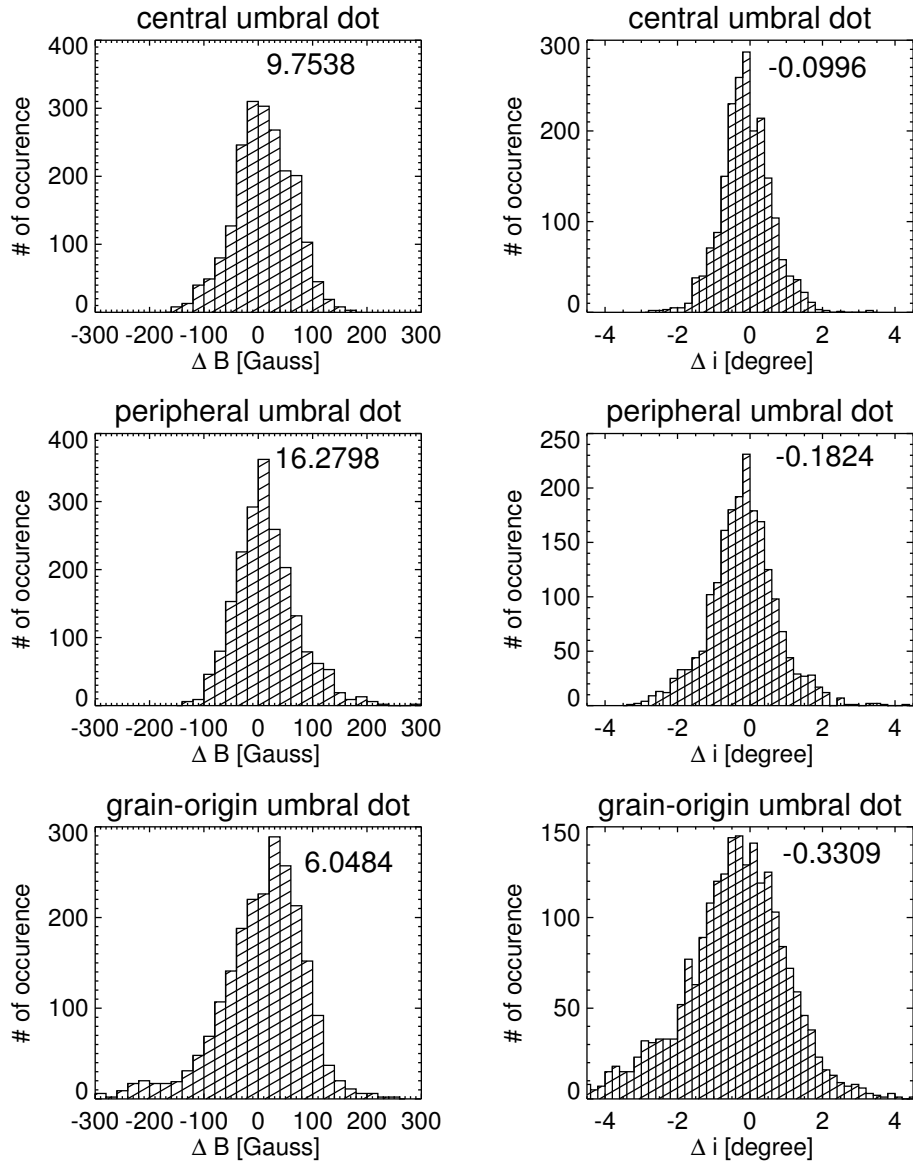


Fig. 44.— Histograms of ΔB and Δi in UDs (UD's position ± 3 pixels). Negative Δi means more inclined field lines, while positive Δi means more vertical fields. Shown in the upper right corner is the center of gravity of each histogram.

than the surroundings, which seems to contradict the field-free model of UDs (Schüssler & Vögler 2006). Our speculation about this result is given in the discussion section. We find small negative Δi (i.e., more inclined fields), which is consistent with previous reports (Socas-Navarro et al. 2004; Riethmüller et al. 2008).

4.5.5. Typical Light Curve

We have studied the typical temporal evolution of UDs using those observed from birth to death and with lifetimes longer than 620 s. In total, we have chosen 36 central, 50 peripheral, and 66 grain-origin UDs for this analysis. By normalizing the lifetime to unity it is possible to average all the evolutionary curves (“light curves” in the following). The results are shown in Figure 45 for eight parameters; I_{peak} , brightness ratio, diameter, field strength, v_{high} , v_{deep} , ΔB , and Δi .

Evolution of Central and Peripheral UDs For central and peripheral UDs, I_{peak} , brightness ratio, diameter, and bisectors show a symmetric increase and decrease over time. The brighter I_{peak} and lower field strength in peripheral UDs compared with central UDs are a natural consequence of peripheral UDs being located in the more external parts of the umbra. We find a peak of upflows for peripheral UDs in the middle of their lives, but for central UDs the v_{deep} curve is almost flat. This is consistent with the conclusion derived in Section 4.2, namely, that in the darkest areas of the umbra the correlation between brightness and upflow breaks up. The magnetic field parameters (field strength, ΔB , Δi) are almost constant throughout the lifetime, although for peripheral UDs ΔB shows the tendency of getting larger as the UDs evolve.

Evolution of Grain-Origin UDs For grain-origin UDs, all parameters other than bisectors show monotonic increase or decrease patterns. It is explained by the smooth transition from penumbral grains to the circular UDs in the central umbra. The bisectors peak at shortly after the beginning of the lifetime, when the tips of penumbral grains are completely detached. Although with larger scatters, local reduction of field strength and more inclined field inclination are found in the first half of the lifetime, while opposite properties (local increased and more vertical field) appear in the latter half of the lifetime.

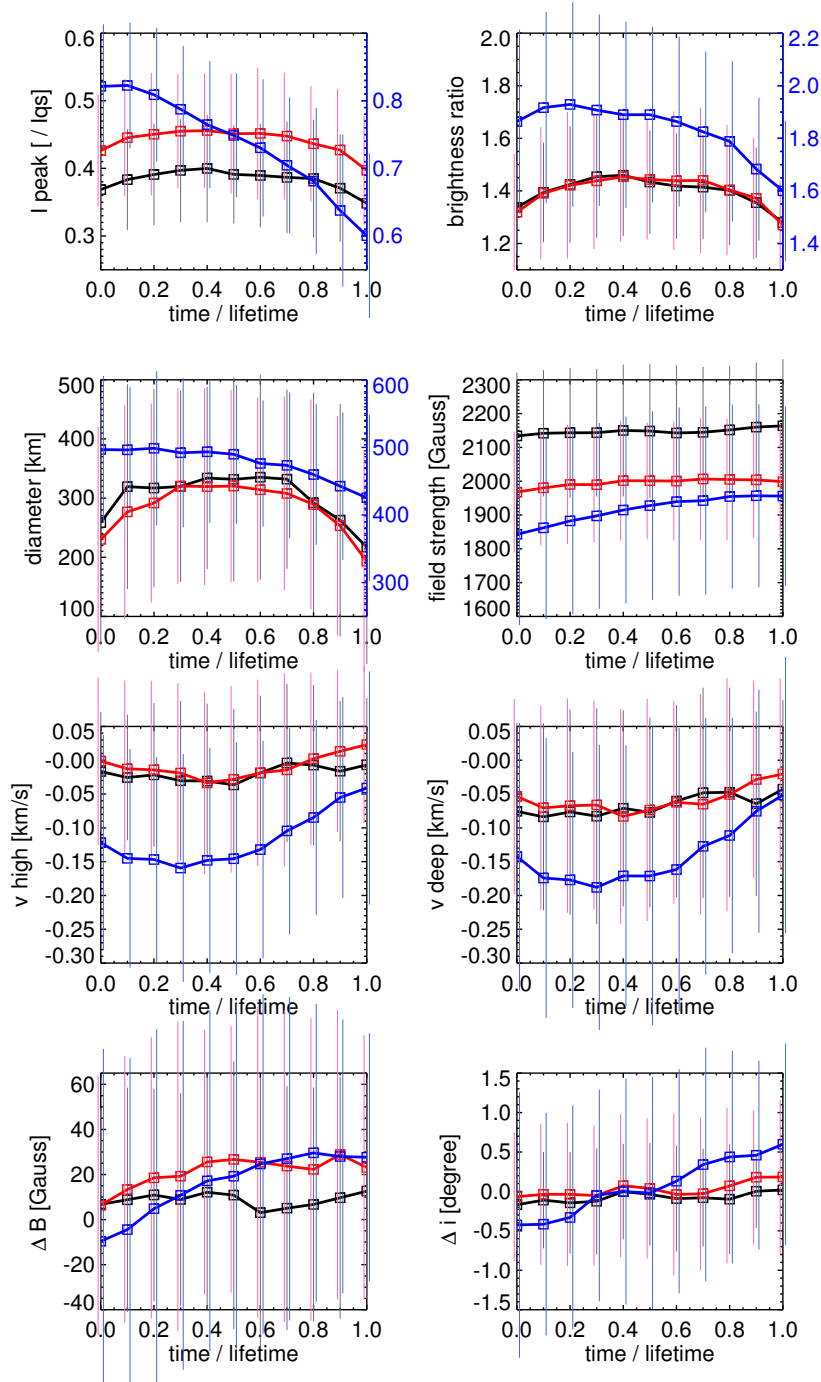


Fig. 45.— Typical light curves of peak brightness (I_{peak}), brightness ratio, diameter, field strength, v_{high} , v_{deep} , ΔB , and Δi for central (black), peripheral (red), and grain-origin UD (blue). The axis for grain-origin UD is separately shown to the right in I_{peak} , brightness ratio, and diameter panels. The $1-\sigma$ error bars are shown by vertical lines.

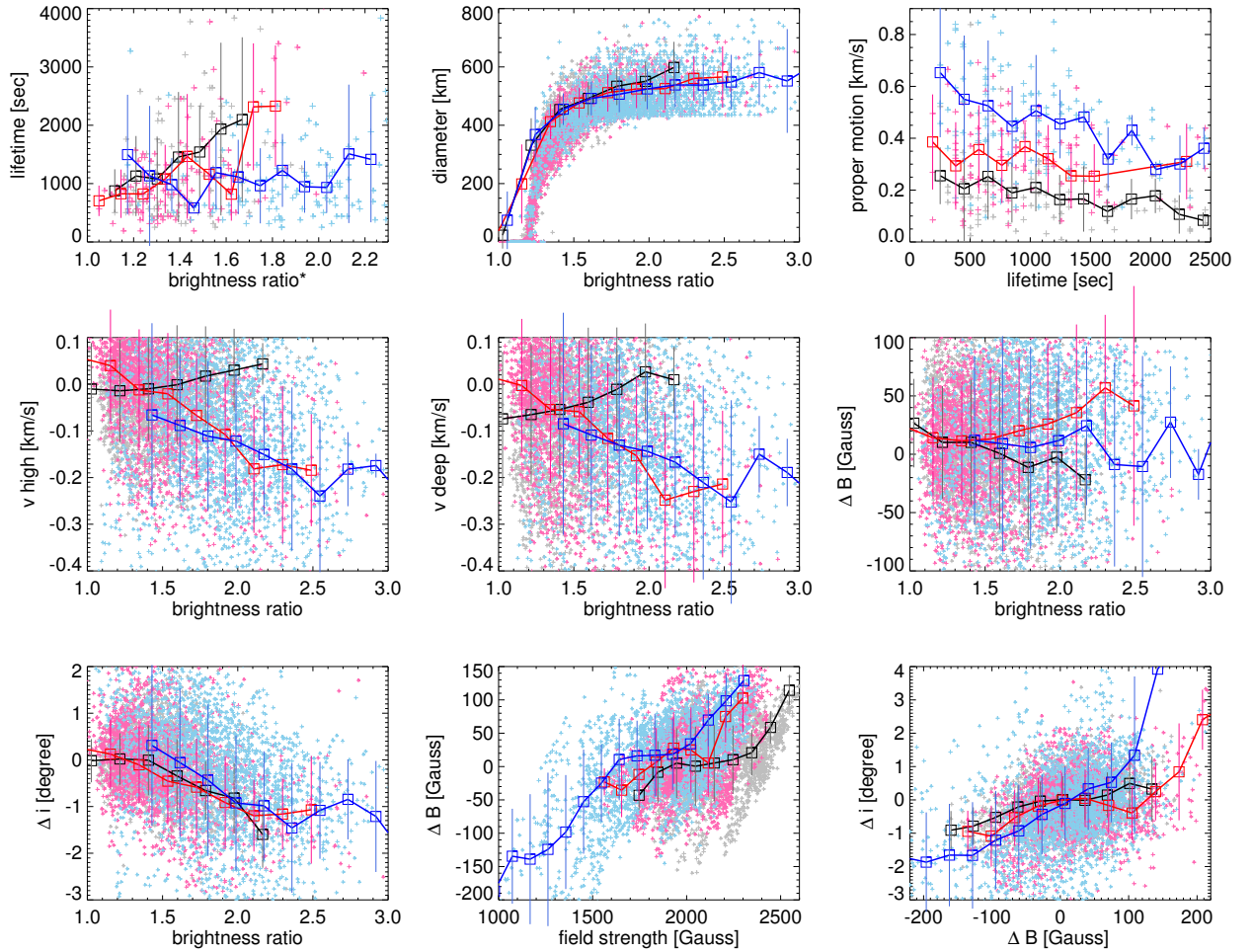


Fig. 46.— Scatter relationships among eight parameters (brightness ratio, lifetime, proper motion, diameter, field strength, v_{deep} , ΔB , Δi) separated for central (black), peripheral (red), and grain-origin UDs (blue). The square signs and thick lines indicate the average values in the corresponding bins. The 1- σ error bars are shown by vertical lines.

4.5.6. Scatter Relations

The scatter diagrams among eight parameters (brightness ratio, lifetime, proper motion, diameter, field strength, v_{deep} , ΔB , Δi) are shown in Figure 46, separately for central (black), peripheral (red), and grain-origin UDs (blue). For example, the scatter diagram between lifetime and proper motion (top right panel) demonstrates the speed is the slowest for central UDs and the fastest for grain-origin UDs, and the speed decreases linearly for long-living UDs. In all diagrams generally, the similar trends apply to all types of UDs, although there are some differences in their bisector properties. We summarize the results derived from the scatter diagrams as follows:

1. Bright central and peripheral UDs often show recurrence, and this is why longer lifetime is seen for brighter ones. Other than that, the lifetime is constant regardless of type of UDs.
2. The diameter increases linearly while brightness ratio is lower than 1.4 as we adopt brightness threshold method for diameter calculation, but it saturates to a constant value (about 500 km), demonstrating that UDs have typical size.
3. The proper motion speed decreases linearly against lifetime.
4. Brighter peripheral and grain-origin UDs show stronger upflow, while the opposite sense applies to central UDs.
5. There is no correlation between brightness ratio and ΔB .
6. Bright UDs are associated with more horizontal fields, while dark UDs are associated with more vertical fields.
7. Strong inverse-correlations are found between field strength and ΔB . In strong field strength regions, ΔB is positive.
8. Negative ΔB is associated with more horizontal fields, and positive ΔB is associated with more vertical fields.

We consider bisectors, ΔB , and Δi as the important parameters to characterize the convective motion of UDs. The field-free convection model of UDs suggests upflow, weakening of field strength, and more inclined field lines. These situations are indeed true at regions where field strength is relatively weak (<2000 Gauss). Brighter UDs are considered to be manifestations of strong convection, and thus we found stronger upflow. However in the strong field regions (>2000 Gauss), positive ΔB and more vertical field lines are found commonly for all types of UDs.

4.6. Discussion and Conclusion

In this paper we give a detailed analysis of UDs in a mature sunspot observed with the CRISP at the SST. The excellent spatial resolution, temporal cadence, and polarimetric sensitivity of our measurements are best optimum for the UD studies. The perturbations caused by UDs are usually very small, and thus the statistics are needed to derive their common properties. Our study marks the first report to show the temporal evolution of velocity and magnetic fields in and around UDs with sufficient statistics.

Convection in the umbra UDs are considered to be manifestations of convection suppressed by the umbral magnetic field, while more vigorous convection occurs in the quiet-sun observed as granules. We confirmed this conclusion in Section 4.4.

The morphological difference between granules and UDs is shown in Figure 38. Granules are characterized by apparent sharp edges and irregular polygonal shapes driven by overshooting cellular convection (Spruit et al. 1990). UDs, on the other hand, have a Gaussian brightness distribution. The linear analysis tells that the preferred horizontal scale of convection decreases with increasing field strength (Weiss et al. 1990), and this explains why the size of UDs is smaller than granules. The convective origin of UDs seems to be solid as many papers including ours found upflows with weaker magnetic fields. However there are other diffuse areas with enhanced brightness, whose their origins are not explained. Our speculation that all brightness patterns observed in the umbra are the convective manifestations, could not be proved by the brightness versus bisector scatter plots (Figure 39).

Photometric property Watanabe et al. (2009a) found constant lifetime regardless of the UD types and the structure of magnetic field at the occurring sites. This is in agreement with our result (Section 4.5.6), although longer lifetime for brighter UDs were found in Tritschler & Schmidt (2002) and Bharti et al. (2010).

The proper motion property of UDs, i.e., faster proper motion as longer radial distance from the umbra center, is consistent with the previous reports Watanabe et al. (2009a). The correlation between shorter lifetime and faster proper motion is first reported in this paper (Figure 46). If we compare lifetime and the travel distance (lifetime \times proper motion speed), it shows linear increase with lifetime, i.e., long-living UDs travel longer distances with slower motion speed. The same conclusion can be obtained from a similar analysis on the data set of Watanabe et al. (2009a). It tells that the proper motion speed rate may depend on the energy dissipation rate, and as the energy dissipation rate is low, the lifetime becomes longer.

We found a consistent value of UD diameter with previous literatures, i.e., about 350 km. The gaussian shape of the histogram (Figure 34) and flat dependency on brightness ratio (Figure 46) support that UDs have a “typical” size. The size evolves as synchronized with the brightness light curve (Figure 45). Watanabe et al. (2009a) could not find clear dependency of size on the background field strength, and we confirmed this using our data set (not shown). This common UD size is probably determined by a universal near-surface stratification of mature sunspots.

We do not study the oscillation of the UD intensity which was reported by, e.g., Rimmele (1997), because of uncertainties accompanied by the seeing disturbances. However it is true that many UDs show recurrence. For example, a peripheral UD shown as UD#C in Figure 53 show a double recurrence at about 13 min interval. This timescale is comparable to the oscillatory UDs shown in Rimmele (1997) and Watanabe et al. (2009b).

Categorization of UDs We adopted the categorization of UDs depending on their origin and place of birth (central, peripheral, and grain-origin UDs), but are they really different or the same? Grain-origin UDs have larger brightness ratio, larger size, and faster proper motion than the other two. The temporal evolution of grain-origin UDs are characterized by monotonic change, while central and peripheral UDs show a mound-shape light curves (Figure 45). However, the scatter plots in Figure 46 tell that the properties of grain-origin UDs are the extension of those of central and peripheral UDs. The difference may arise from stronger convection in grain-origin UDs because of weaker field background. Spruit & Scharmer (2006) proposed the common field-free convection model can explain both UDs and penumbral grains. The computer simulations by Heinemann et al. (2007) and Rempel et al. (2009) succeeded in reproducing basic properties of penumbral filaments as well as UDs in the same framework of the field-free convection. Our results give a supporting evidence for the validity of their models.

Substructures The existence of localized downflow patches is reported in Section 4.5.1. The downflow patches in Figure 41 have size of $0.2''$ and downflow velocity of up to 0.75 km s^{-1} . Both the size and the velocity are in good agreement with those reported in Ortiz et al. (2010). The fact that the downflow patches are observable only at the very deep bisector level is also consistent with their result. In our analysis, the dark lane is not observed.

However, it is true that there are many UDs without downflow patches. We attribute the reason to:

1. The lack of spatial resolution.
2. The downflow patches exist in deep layers that cannot be probed by Fe I bisectors.

3. Downflow patches appear only in a particular phase of the evolution.
4. The convective energy escapes to the upper layers instead of returning to deep layers (see the narrow jet-like upflow above the cusp in Schüssler & Vögler 2006).

Both of the two UDs in Figure 41 (UD#F and UD#G) are in the peak brightness phase when the downflow patches are observed. Possibly the speed of downflow becomes the largest when the brightness peaks.

Evolution of velocity field around UDs The peak of upflow is synchronized with the peak of brightness (Figure 45). This is in a good agreement with the results in Sobotka & Jurčák (2009) and Watanabe et al. (2010). These upflow associated with UDs is considered to be a field-aligned plasma flow, because the upflow is readily found at the disk-center side, but not in the limb side (Section 4.5.1). The same discussion applies to the Evershed flow (Figure 33), which is also a field-aligned flow.

We found the downflow region at the migration front observed in part of grain-origin UDs for the first time (see the evolution of UD#D shown in Figure 54). The MHD simulation by Heinemann et al. (2007) (see Figure 6 in their paper) predicts downflow at the tail of inward migrating penumbral grains, but not at the migration front. We expect the downflow at the migration front of grain-origin UDs are not convective overturning downflow, but are created by the compression of magnetic field located next to the expansion of field at the position of a UD.

Evolution of magnetic field around UDs The prevailing theory of the field-free convection (Schüssler & Vögler 2006) predicts reduction of field strength and more inclined field lines at the sight of UDs. From the scatter relations (Figure 46) we confirmed these properties, but only in the region of weak fields. On the other hand in the strong field regions, increase of field strength and more vertical fields are observed, which seems to contradict the field-free convection model. Many literatures (Socas-Navarro et al. 2004; Riethmüller et al. 2008; Watanabe et al. 2009b) found reduced and more horizontal fields, but those results are based on the data of sunspots located near the disk center. In our case, the target was located away from the disk center (heliocentric angle of 35°). Watanabe et al. (2009b) studied the dependency of UD's local perturbations (Δv , ΔB , Δi) on the heliocentric angle of the sunspot location. They found the reduction of fields for UDs inside the sunspots near the disk center, but the opposite property is found if the sunspot is far from it. They attribute this reason to the center-to-limb variation of the line formation height of the spectral lines. As the sunspot goes away from the disk center, the line formation height becomes higher and higher, and at some point it is raised upper than the field-free convective gaps. The

magnetic field strength above the field-free gaps is supposed to get stronger because of the magnetic tension force.

The magnetic property also depends on the phase of the evolution. Reduced and more inclined fields appear in the appearance phase, while increased and more vertical fields appear in the disappearance phase. This property is the most clearly visible in grain-origin UDs. We want to note that field reduction patches observed in the appearance phase are associated with UDs, but the increase of field strength in the disappearance phase seems to be caused by a intrusion into pre-existing strong field region. The strong field regions at the migration front of grain-origin UDs are observed, as is best seen in UD#E (Figure 56). This signature reminds us of the embedded thin flux tube models in Schlichenmaier et al. (1998), in which the weakly magnetized flux tube (i.e., UD) pushes the pre-existing vertical field and makes a compressed area at the leading edge. However, the field-free convection model can also create the compression of magnetic field around UDs, because of the expansion of field at the sight of UDs.

Model of UDs We found some new and important insights about UDs;

- Central and peripheral UDs statistically show very weak upflow, while grain-origin UDs show clear upflow of the order of a few hundred m/s.
- Increased and more vertical magnetic fields are observed for UDs in strong field regions or UDs in their disappearance phase.
- The strong field regions appear at the migration front of grain-origin UDs as if their motion is impeded by the strong ambient field.

We attribute these differences depending on the type of UDs to the line formation height (optical depth unity). As our target sunspot is located away from the disk center, the line formation height assumed here is higher than the one assumed in the disk center observation case. Figure 47 illustrates our model. The hot plasma plumes emerge into the pre-existing near-vertical magnetic fields and expand them. UDs are observed as a result of radiative heating around the tips of these hot plumes (Schüssler & Vögler 2006; Bharti et al. 2010). Because of the expansion, the fields in the surrounding of plumes get stronger. Also the fields just above the plumes are supposed to get stronger because of the magnetic tension force. For the case of central and peripheral UDs, the formation height is too high to observe the plume itself (i.e., reduction of field and upflow) even in their peak phase. We interpret the reason of positive ΔB in two ways. The first interpretation is denoted by the gray bars shown in the upper panels of Figure 47. The line formation height intersects with the layer above the plume where the field gets stronger. The second interpretation is explained by the

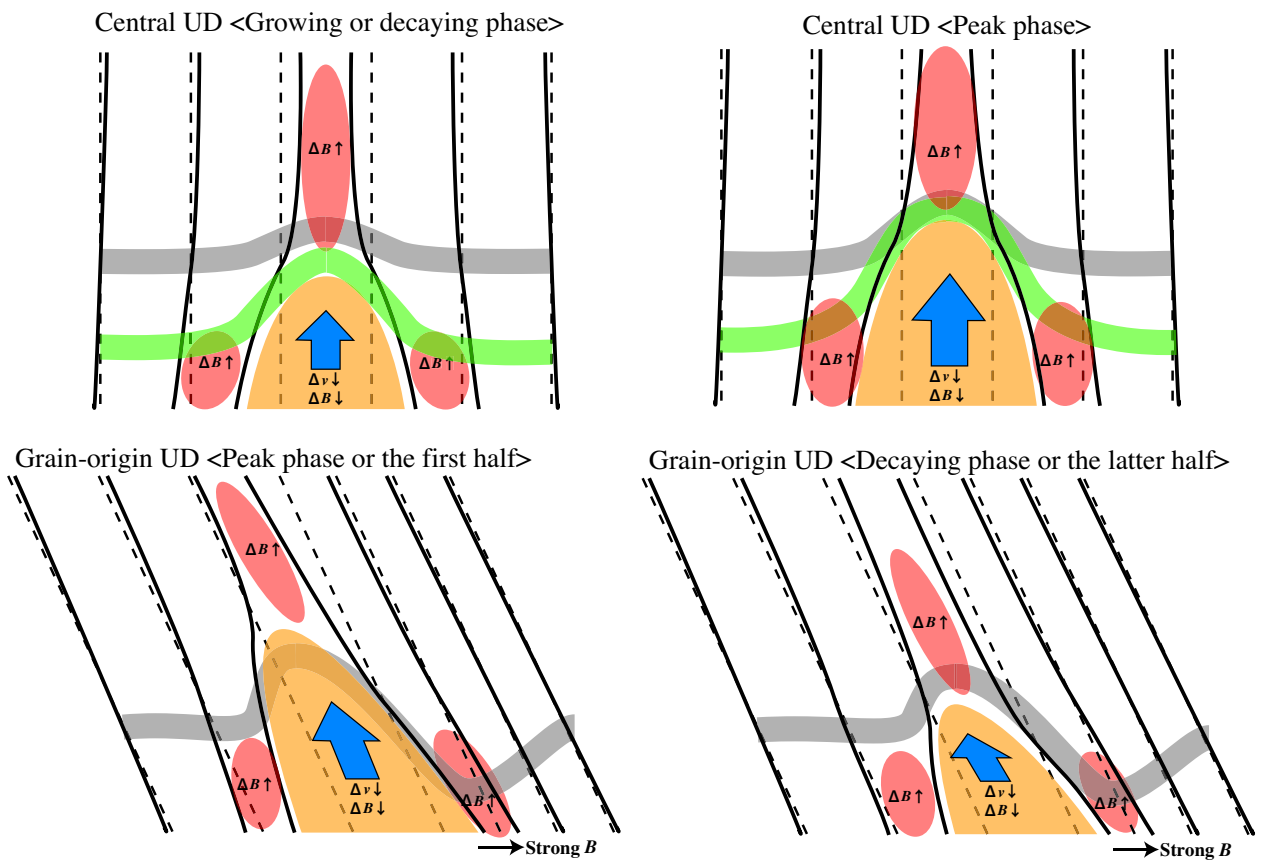


Fig. 47.— The illustrative model of central (top) and grain-origin (bottom) UDs. The near-vertical black lines mean the pre-existing (dash line) and modified (solid line) magnetic field lines. The yellow region corresponds to the hot plasma plume observed as UDs at the surface. The gray band and the green band indicate the line formation height. See the text for further explanation.

green bar. In this case the line formation height intersects with the stronger field regions encompassing the plumes. In order to distinguish these two interpretation, we may need a multi-line spectropolarimetric observation or much higher spatial resolution.

The similar discussion applies to the grain-origin UDs, too. For the grain-origin UDs in their peak phase, when the background field strength is weak, the formation height can reach the plume and thus observes the field reduction and upflow. However in their decay phase, the plumes goes down and again the formation height gets higher than the plumes.

We interpret the inward migration of UDs in the peripheral region of the umbra like this. In the peripheral region of the umbra, the field is characterized by the inclined field line with strength gradient to the umbra center. When an UD appears to the area with gradient of field strength, the intrusion occurs more vigorously in the weaker field side than in the stronger field side. This causes asymmetric magnetic pressure enhancement, and makes the situation that another hot gas, i.e. UD, goes up at the surface of stronger field side. This sequence is observed as the inward migration.

The interpretations of strong field regions at the migration front of grain-origin UDs needs more speculation. Because of the asymmetric emergence of the hot gas, the optical depth unity layer also becomes asymmetric, with the favor of deeper diving at the umbra center side. The MHD simulations performed by Heinemann et al. (2007) predict the existence of enhanced field strength region surrounding the grain-origin UD only in deeper layers than the optical depth unity layer (see Figure 3 in their paper), but both at the leading side and the tail side. Our observation did not find field enhancement at the tail side. The careful comparison between models and our observation may give a suggestion to the validity of our model.

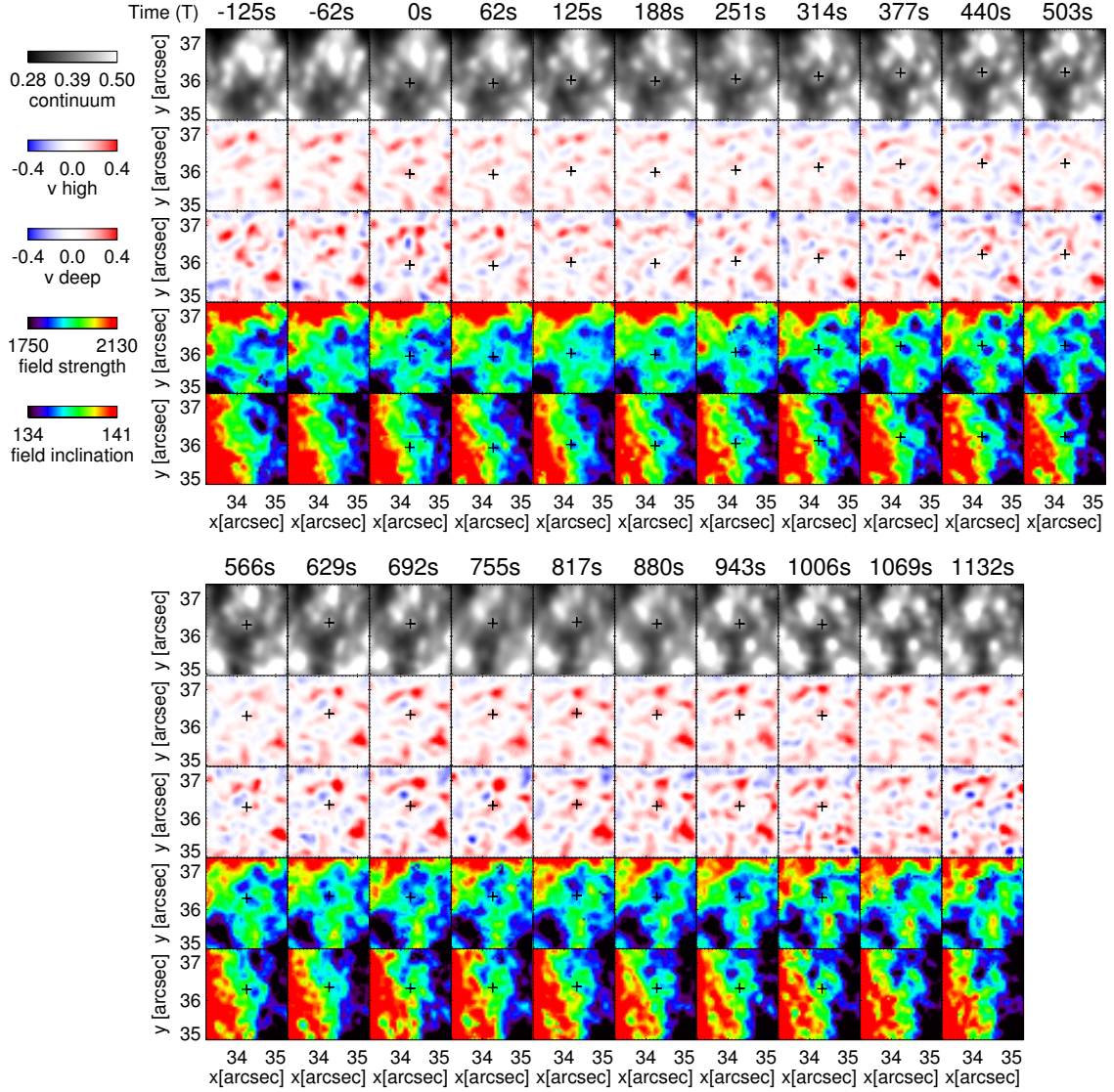


Fig. 48.— The temporal evolution of a central UD (#A) from 2 frames before the appearance until 2 frames after the disappearance. From top to bottom, images of continuum intensity, Δv_{high} , Δv_{deep} , field strength, and field inclination are shown. $T=0$ means the UD appearance timing. The black plus symbols indicate the position of the UD. The (x, y) coordinates follow the coordinate system used in Figure 31.

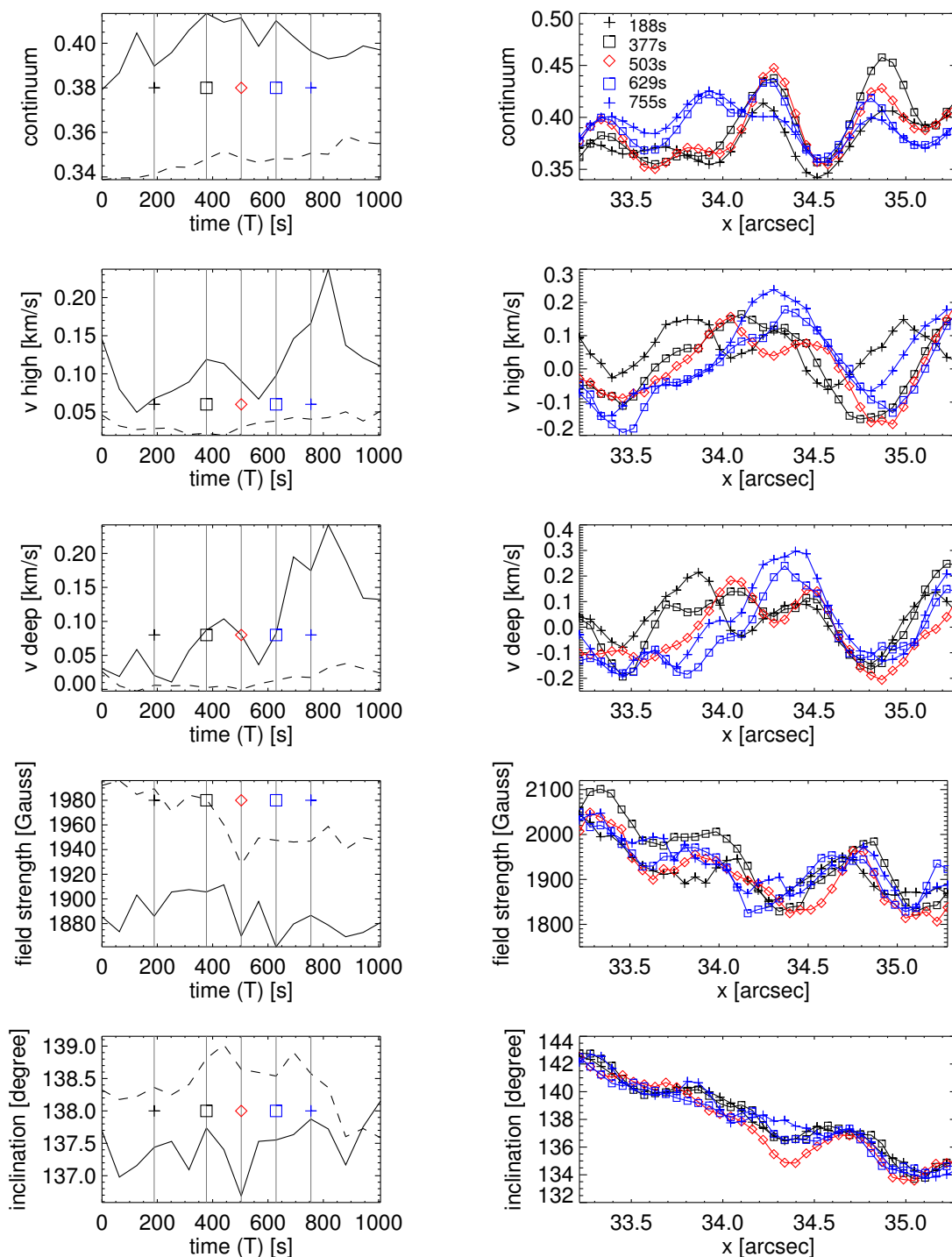


Fig. 49.— *Left*: The light curves of continuum, Δv_{high} , Δv_{deep} , field strength, and field inclination at a central UD#A (solid line, average within UD's position ± 2 pixel area). The dashed lines are light curves of the dark background. Time starts from the appearance of the UD. *Right*: The spatial profiles along x direction of continuum, Δv_{high} , Δv_{deep} , field strength, and field inclination. The five different lines are sampling the timings of 188 s (black plus), 377 s (black square), 503 s (red diamond), 629 s (blue square), and 755 s (blue plus).

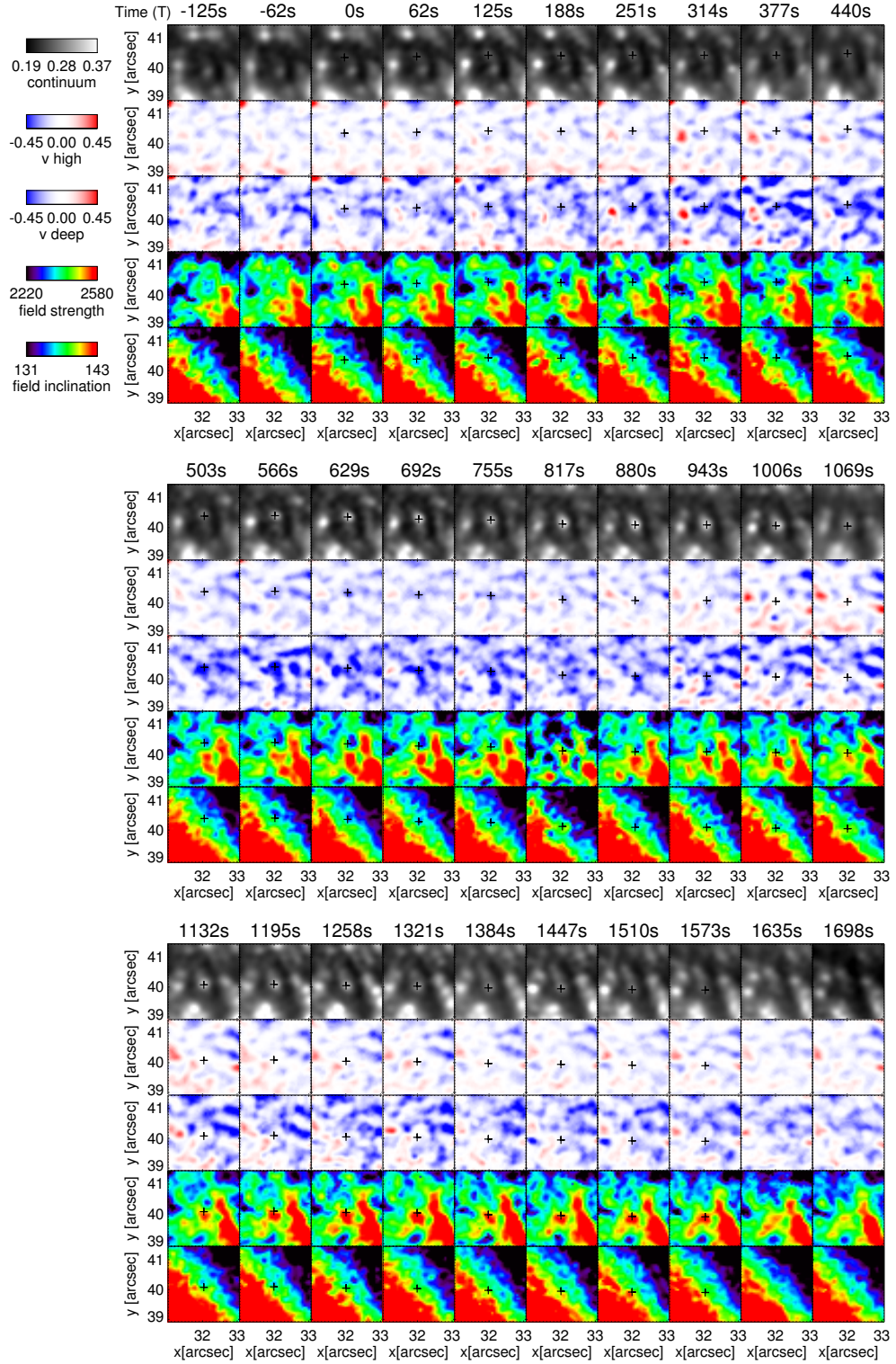


Fig. 50.— The temporal evolution of a central UD (#B) from 2 frames before the appearance until 2 frames after the disappearance. From top to bottom, images of continuum intensity, Δv_{high} , Δv_{deep} , field strength, and field inclination are shown. $T=0$ means the UD appearance timing. The black plus symbols indicate the position of the UD. The (x, y) coordinates follow the coordinate system used in Figure 31.

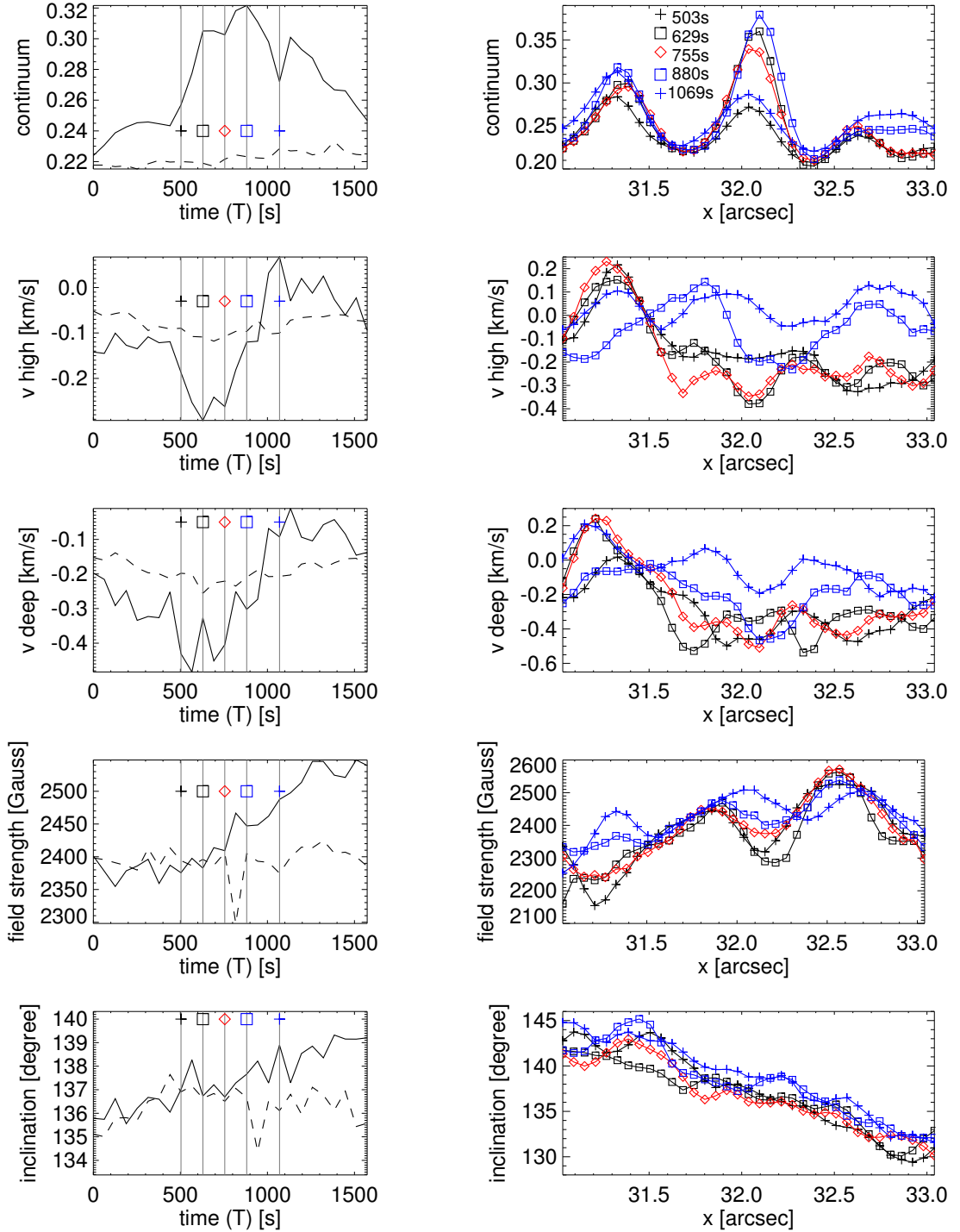


Fig. 51.— *Left:* The light curves of continuum, Δv_{high} , Δv_{deep} , field strength, and field inclination at a central UD#B (solid line, average within UD's position ± 2 pixel area). The dashed lines are light curves of the dark background. Time starts from the appearance of the UD. *Right:* The spatial profiles along x direction of continuum, Δv_{high} , Δv_{deep} , field strength, and field inclination. The five different lines are sampling the timings of 503 s (black plus), 629 s (black square), 755 s (red diamond), 880 s (blue square), and 1069 s (blue plus).

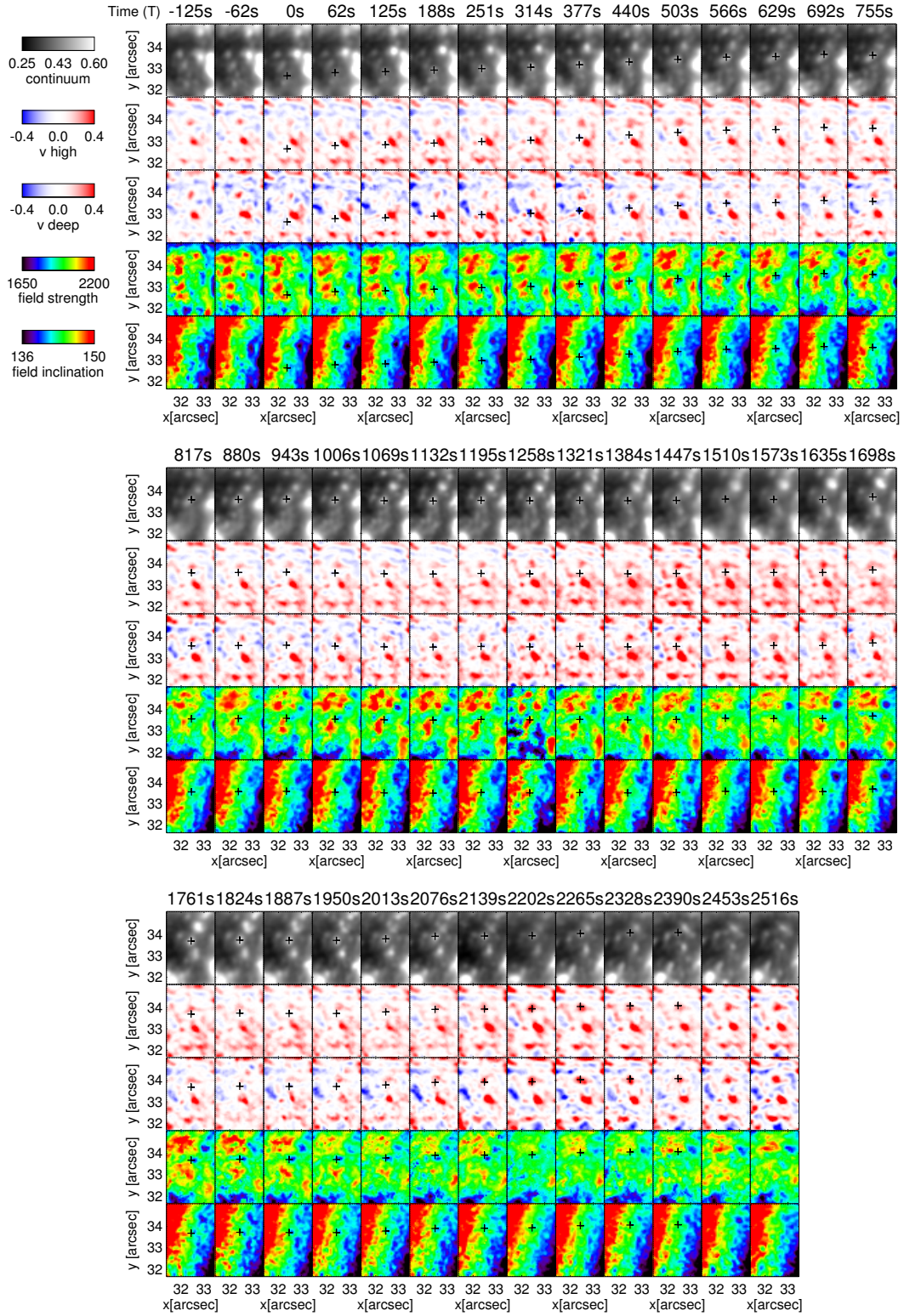


Fig. 52.— The temporal evolution of a peripheral UD (#C) from 2 frames before the appearance until 2 frames after the disappearance. From top to bottom, images of continuum intensity, Δv_{high} , Δv_{deep} , field strength, and field inclination are shown. $T=0$ means the UD appearance timing. The black plus symbols indicate the position of the UD. The (x,y) coordinates follow the coordinate system used in Figure 31.

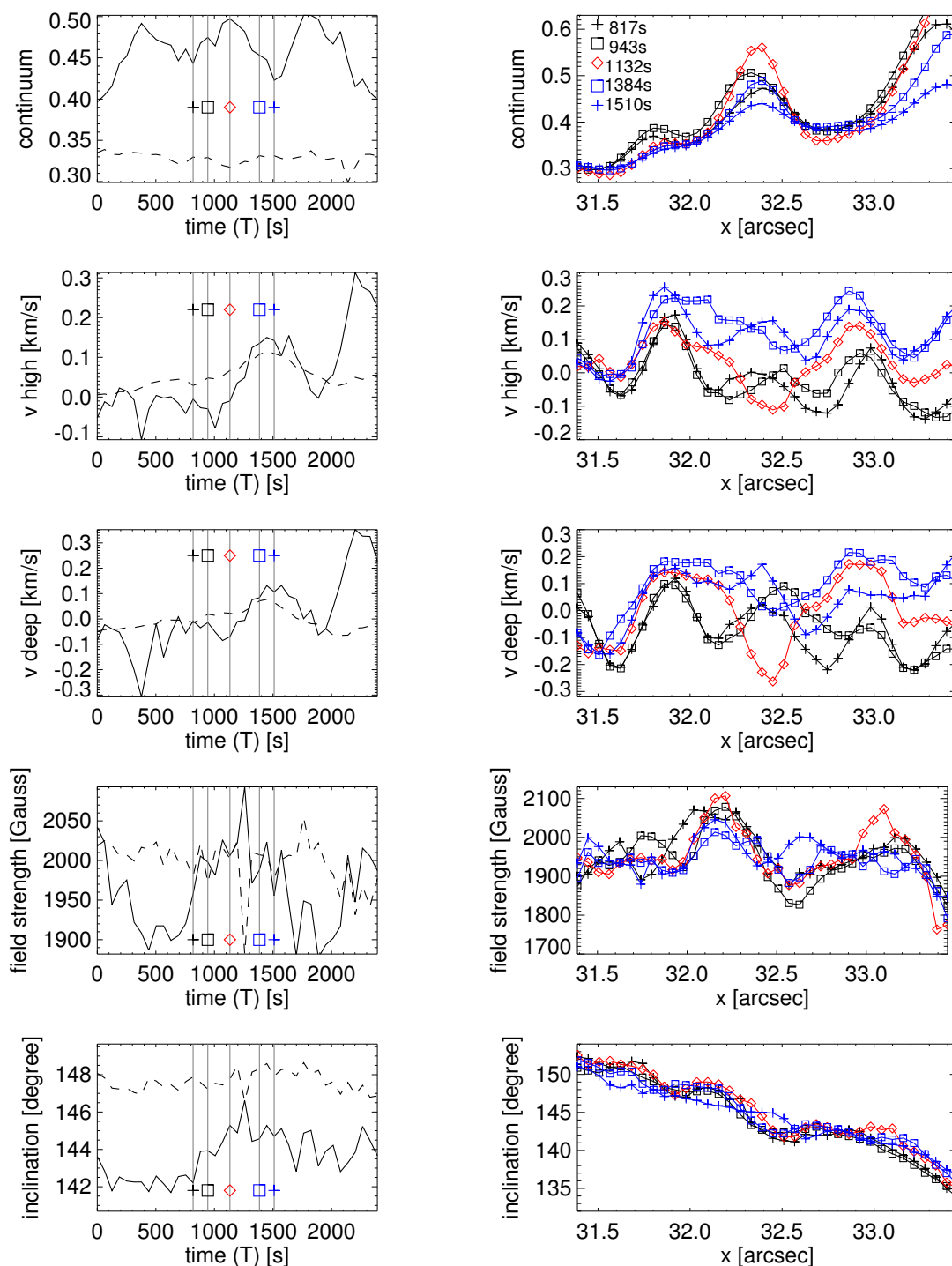


Fig. 53.— *Left:* The light curves of continuum, Δv_{high} , Δv_{deep} , field strength, and field inclination at a peripheral UD#C (solid line, average within UD's position ± 2 pixel area). The dashed lines are light curves of the dark background. Time starts from the appearance of the UD. *Right:* The spatial profiles along x direction of continuum, Δv_{high} , Δv_{deep} , field strength, and field inclination. The five different lines are sampling the timings of 817s (black plus), 943s (black square), 1132s (red diamond), 1384s (blue square), and 1510s (blue plus).

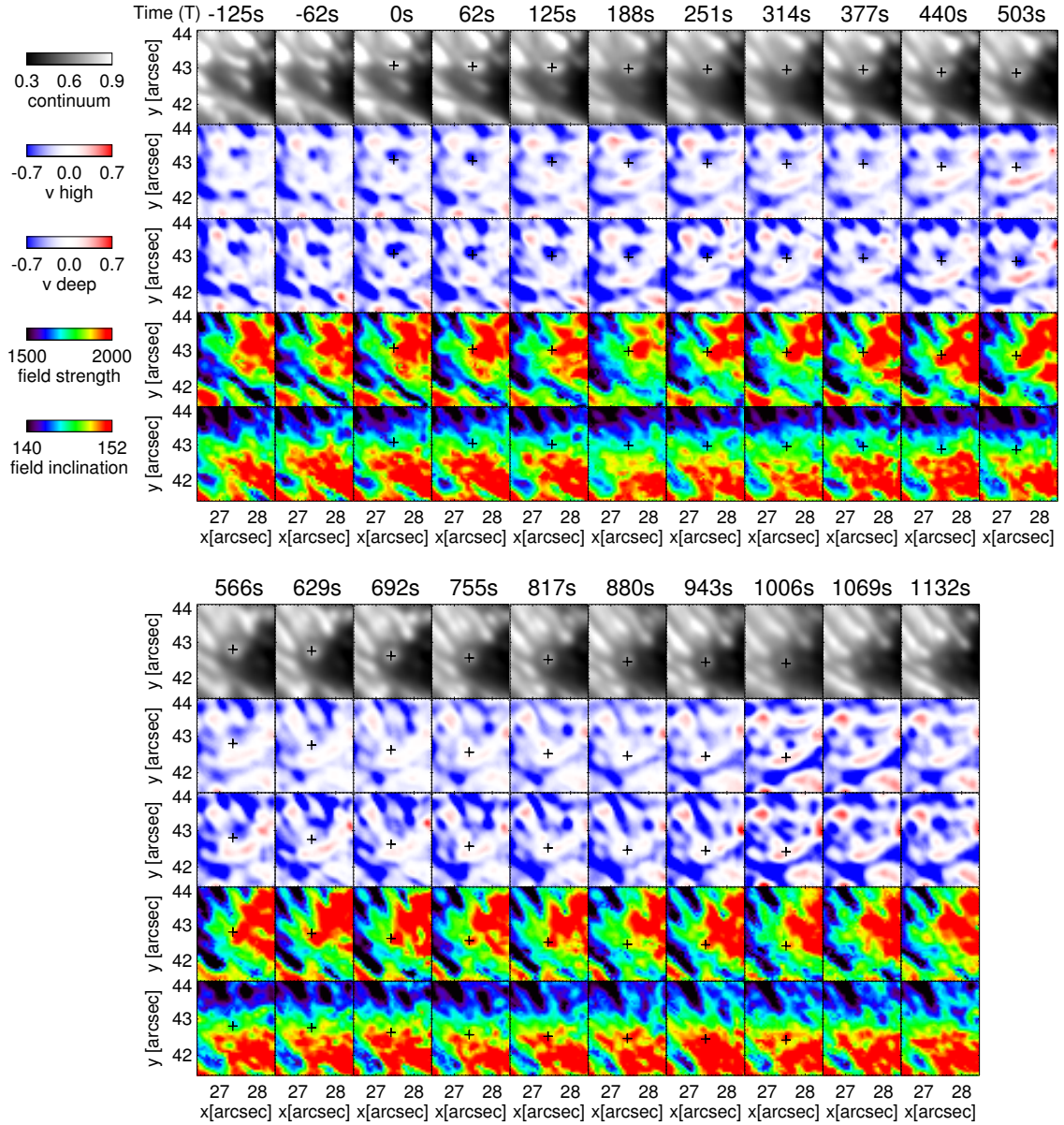


Fig. 54.— The temporal evolution of a grain-origin UD (#D) from 2 frames before the appearance until 2 frames after the disappearance. From top to bottom, images of continuum intensity, Δv_{high} , Δv_{deep} , field strength, and field inclination are shown. $T=0$ means the UD appearance timing. The black plus symbols indicate the position of the UD. The (x,y) coordinates follow the coordinate system used in Figure 31.

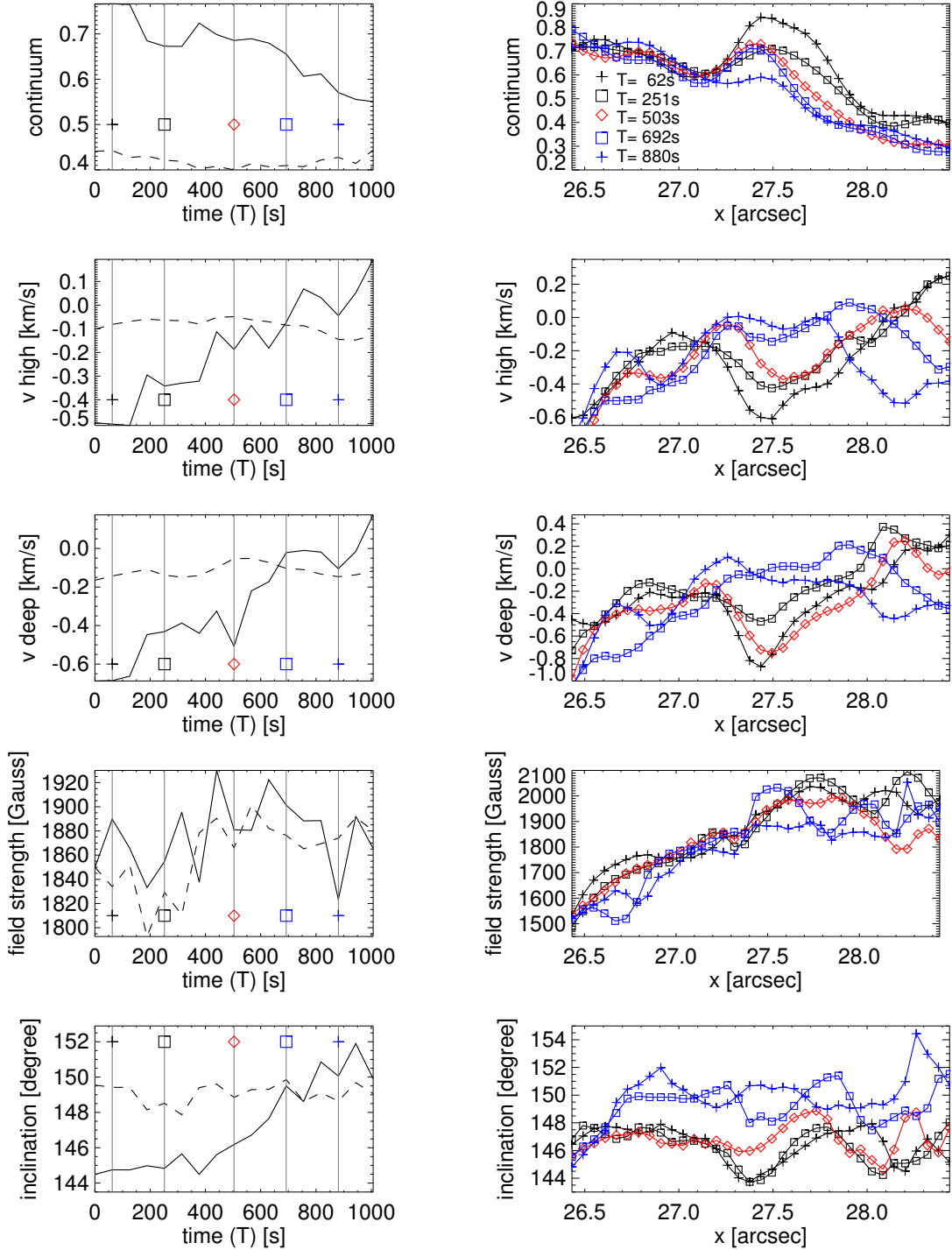


Fig. 55.— *Left:* The light curves of continuum, Δv_{high} , Δv_{deep} , field strength, and field inclination at a grain-origin UD#D (solid line, average within UD's position ± 2 pixel area). The dashed lines are light curves of the dark background. Time starts from the appearance of the UD. *Right:* The spatial profiles along x direction of continuum, Δv_{high} , Δv_{deep} , field strength, and field inclination. The five different lines are sampling the timings of 62 s (black plus), 251 s (black square), 503 s (red diamond), 692 s (blue square), and 880 s (blue plus).

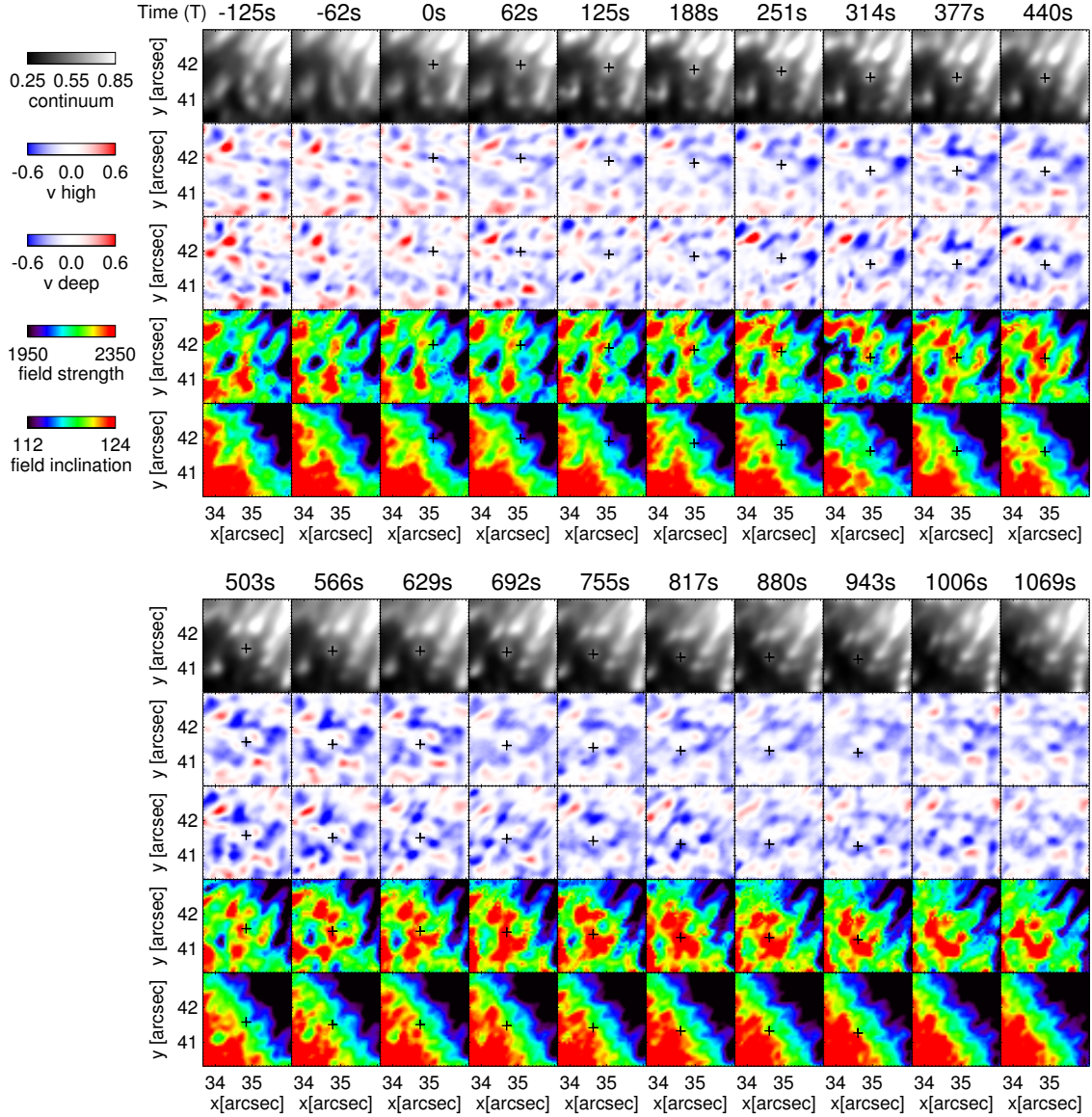


Fig. 56.— The temporal evolution of a grain-origin UD (#E) from 2 frames before the appearance until 2 frames after the disappearance. From top to bottom, images of continuum intensity, Δv_{high} , Δv_{deep} , field strength, and field inclination are shown. $T=0$ means the UD appearance timing. The black plus symbols indicate the position of the UD. The (x,y) coordinates follow the coordinate system used in Figure 31.

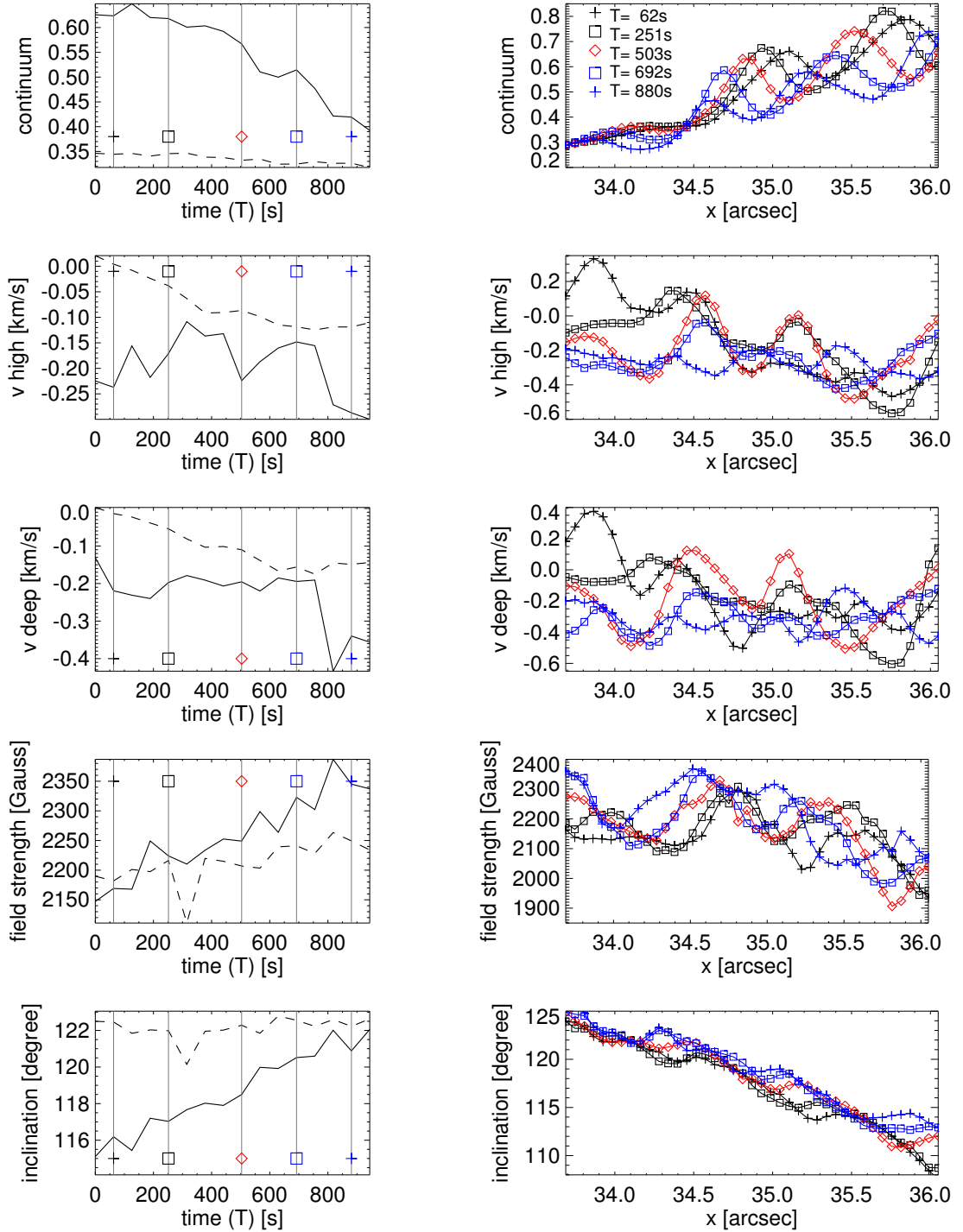


Fig. 57.— *Left*: The light curves of continuum, Δv_{high} , Δv_{deep} , field strength, and field inclination at a grain-origin UD#E (solid line, average within UD's position ± 2 pixel area). The dashed lines are light curves of the dark background. Time starts from the appearance of the UD. *Right*: The spatial profiles along x direction of continuum, Δv_{high} , Δv_{deep} , field strength, and field inclination. The five different lines are sampling the timings of 62 s (black plus), 251 s (black square), 503 s (red diamond), 692 s (blue square), and 880 s (blue plus).

REFERENCES

- Bahng, J., & Schwarzschild, M. 1961, *ApJ*, 134, 312
- Bharti, L., Beeck, B., & Schüssler, M. 2010, *A&A*, 510, A12
- Bharti, L., Jain, R., & Jaaffrey, S. N. A. 2007a, *ApJ*, 665, L79
- Bharti, L., Joshi, C., & Jaaffrey, S. N. A. 2007b, *ApJ*, 669, L57
- Collados, M., Martinez Pillet, V., Ruiz Cobo, B., del Toro Iniesta, J. C., & Vazquez, M. 1994, *A&A*, 291, 622
- Deinzer, W. 1965, *ApJ*, 141, 548
- Ewell, M. W., Jr. 1992, *Sol. Phys.*, 137, 215
- Heinemann, T., Nordlund, Å., Scharmer, G. B., & Spruit, H. C. 2007, *ApJ*, 669, 1390
- Hirzberger, J., Bonet, J. A., Vázquez, M., & Hanslmeier, A. 1999, *ApJ*, 515, 441
- Kilcik, A., Yurchyshyn, V. B., Rempel, M., et al. 2012, *ApJ*, 745, 163
- Kitai, R. 1986, *Sol. Phys.*, 104, 287
- Kitai, R., et al. 2007, *PASJ*, 59, 585
- Lites, B. W. 1992, *NATO ASIC Proc. 375: Sunspots. Theory and Observations*, 261
- Markwardt, C. B. 2009, *Astronomical Data Analysis Software and Systems XVIII*, 411, 251
- Martinez Pillet, V., & Vazquez, M. 1993, *A&A*, 270, 494
- Moradi, H., et al. 2010, *Sol. Phys.*, 267, 1
- Ortiz, A., Bellot Rubio, L. R., & Rouppe van der Voort, L. 2010, *ApJ*, 713, 1282
- Rempel, M., Schüssler, M., & Knölker, M. 2009, *ApJ*, 691, 640
- Riethmüller, T. L., Solanki, S. K., & Lagg, A. 2008a, *ApJ*, 678, L157
- Riethmüller, T. L., Solanki, S. K., Zakharov, V., & Gandorfer, A. 2008b, *A&A*, 492, 233
- Rimmele, T., & Marino, J. 2006, *ApJ*, 646, 593
- Rimmele, T. R. 1997, *ApJ*, 490, 458
- Roudier, T., & Muller, R. 1987, *Sol. Phys.*, 107, 11

- Roupe van der Voort, L. H. M., Rutten, R. J., Sütterlin, P., Sloover, P. J., & Krijger, J. M. 2003, *A&A*, 403, 277
- Ruiz Cobo, B., & del Toro Iniesta, J. C. 1992, *ApJ*, 398, 375
- Scharmer, G. B. 2006, *A&A*, 447, 1111
- Scharmer, G. B., Bjelksjo, K., Korhonen, T. K., Lindberg, B., & Petterson, B. 2003, *Proc. SPIE*, 4853, 341
- Schlichenmaier, R., Jahn, K., & Schmidt, H. U. 1998, *A&A*, 337, 897
- Schnerr, R. S., de La Cruz Rodríguez, J., & van Noort, M. 2011, *A&A*, 534, A45
- Schüssler, M., Vögler, A. 2006, *ApJ*, 641, L73
- Selbing, J. 2010, arXiv:1010.4142
- Sobotka, M., Bonet, J. A., & Vazquez, M. 1993, *ApJ*, 415, 832
- Sobotka, M., Brandt, P. N., & Simon, G. W. 1997a, *A&A*, 328, 682
- Sobotka, M., Brandt, P. N., & Simon, G. W. 1997b, *A&A*, 328, 689
- Sobotka, M., Brandt, P. N., & Simon, G. W. 1999a, *A&A*, 348, 621
- Sobotka, M., & Jurčák, J. 2009, *ApJ*, 694, 1080
- Sobotka, M., Vázquez, M., Bonet, J. A., Hanslmeier, A., & Hirzberger, J. 1999b, *ApJ*, 511, 436
- Socas-Navarro, H., Martínez Pillet, V., Sobotka, M., & Vázquez, M. 2004, *ApJ*, 614, 448
- Spruit, H. C., Nordlund, A., & Title, A. M. 1990, *ARA&A*, 28, 263
- Spruit, H. C., & Scharmer, G. B. 2006, *A&A*, 447, 343
- Title, A. M., Tarbell, T. D., Topka, K. P., et al. 1989, *ApJ*, 336, 475
- Tritschler, A., Schlichenmaier, R., Bellot Rubio, L. R., the KAOS Team, Berkefeld, T., & Schelenz, T. 2004, *A&A*, 415, 717
- Tritschler, A., & Schmidt, W. 2002, *A&A*, 388, 1048
- van Noort, M., Roupe van der Voort, L., Löfdahl, M. G. 2005, *Sol. Phys.*, 228, 191
- van Noort, M. J., & Roupe van der Voort, L. H. M. 2008, *A&A*, 489, 429

Watanabe, H., Kitai, R., & Ichimoto, K. 2009a, *ApJ*, 702, 1048

Watanabe, H., Kitai, R., Ichimoto, K., & Katsukawa, Y. 2009b, *PASJ*, 61, 193

Watanabe, H., Tritschler, A., Kitai, R., & Ichimoto, K. 2010, *Sol. Phys.*, 266, 5

Weiss, N. O., Brownjohn, D. P., Hurlburt, N. E., & Proctor, M. R. E. 1990, *MNRAS*, 245, 434

5. Summary and Concluding Remarks

5.1. Summary of Results

This thesis is dedicated for the observational study of umbral dots (UDs) in the solar sunspots. UD's are the manifestation of the magnetoconvection whose typical size of 300 km and lifetime of 10 min. The author places special emphasis on the temporal evolution of velocity and magnetic field of UD's, and discuss the results in comparison with the computer-based magnetoconvection simulations. In this section, the brief summary of the results is given, and describe how our results help to improve the understanding of UD's, sunspots, and magnetoconvection.

In Section 4, we report one specific UD which shows significant upflow and fast proper motion appeared at the umbra boundary and propagated towards the center of the umbra, based on the observation at the Dunn Solar Telescope. This is one of the pioneering works that investigate the temporal evolution of UD's velocity field. The average speed of its proper motion is 1.3 km s^{-1} , which is faster than the typical speed of UD's (1.0 km s^{-1} at most). From the spectral bisector analysis, the blueshifts (upflow) associated with this rapidly-moving UD is derived to be about 0.1 km s^{-1} , and show deceleration with height. The upflow of 0.1 km s^{-1} is stronger than any other UD's in the observed sunspot. The decelerating upflow with height is consistent with the scenario of the overshooting convection. The blueshifts reach at least more than 100 km above the continuum level. From the fact that there are no timing difference between the peak blueshifts at different bisector levels, we estimate the propagation speed of the overshooting convection is about $0.5\text{--}0.7 \text{ km s}^{-1}$. No overturning downflow signal was detected in this observation.

We attribute the fast proper motion and strong upflow to the precursor of a light-bridge formation. One day after our observation, a strong light bridge was formed on the trajectory of the rapid-moving UD. Katsukawa et al. (2007) also found rapid-moving UD's in the formation phase of a light bridge. The magnetic fields in light bridges are known to be weaker and more inclined, forming a canopy or arcade shape of field lines (Leka 1997; Jurčák et al. 2006). The rapid-moving UD's may appear only during the period when the reorganization of fields are occurring. Qualitatively, the region with large gradient in field strength is the preferred location for rapid-moving UD's (Scharmer et al. 2008). The next step is the full reproduction of light-bridge formation in the MHD simulations, which has not been succeeded yet.

Section 5 describes the correlation between UD's and their local vector magnetic field

using the high-precision spectropolarimetric observation by the *Hinode* Solar Optical Telescope. The lifetime of UDs is found to be constant regardless of the magnetic field strength at their emergence sites. The size of UDs also shows almost no dependency on the magnetic field, with a small tendency of getting smaller at strong field regions. The direction of the proper motion of UDs is parallel with the horizontal components of magnetic field. There is a positive correlation between the proper-motion speed of UDs and the field inclination. Some UDs show oscillatory intensity variation, whose low-frequency components around 1–2 mHz (corresponds to period of 8–16 min) are dominant.

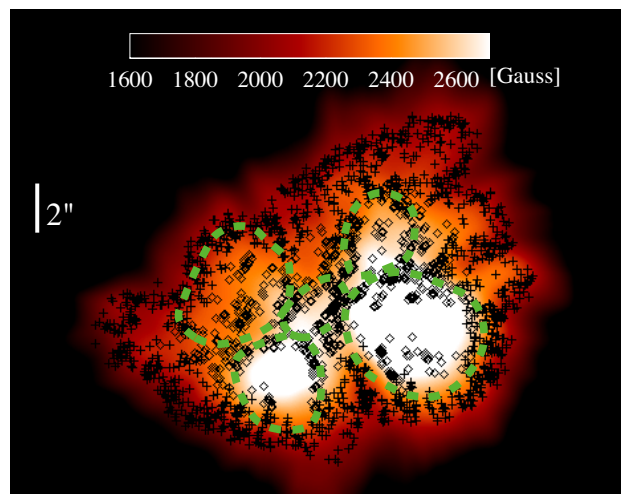


Fig. 58.— The emergence positions of the central UDs (diamonds) and the peripheral UDs (plus signs), overlaid on the background image of magnetic field strength. The green dashed line contours indicate the cluster-like distribution of UD emergence.

No dependency of UD's lifetime and size on their magnetic field strength is inconsistent with the property of the simulated UDs by M. Schüssler & A. Vögler (2006, private communication). In their simulation, shorter lifetime was found in stronger field regions. However their simulation is performed on the basis of vertical uniform magnetic field. The inconsistency may come from the realistic inclined field configuration where the field is weak. The positive correlation between the field inclination and UD's proper motion speed can be explained in terms of the bending process of field lines (Spruit & Scharmer 2006). When hot gas ascends along the inclined magnetic field, the gas undergoes radiative cooling and becomes denser. The heavy gas bends the surrounding magnetic field line, increasing their inclination, and then the magnetic field strength at the upper side of the bent field lines is weakened. In order to balance the reduced magnetic pressure, more hot gas rises up from below and causes the apparent movement of the UD. This process occurs repeatedly, and produces the inward migration of peripheral UDs. The interpretation of the oscillatory intensity variation is not straightforward, because they can be caused either by overlapping

with adjacent UDs, by an additional heat flux into the UD, or by the period of oscillatory convection.

Another impressive finding is the cluster-like distribution of UDs (Figure 58). In addition to the negative correlation between the field strength and the occurrence rate of UDs, Figure 58 shows cellular patterns which remind us of the cluster model of the sunspot structure (Parker 1979), i.e., the flux tubes encircled by the dense UD distribution is the components of the cluster-type sunspot. Most probably, the structure of the sunspot is intermediate between the monolithic and cluster type. Although the very deep root of the fields may be scattered in bundles, the near-surface physics can be described in the monolithic structure.

Finally in Section 6, we study the temporal evolution of UDs with excellent spatial and temporal resolution data observed by the Swedish Solar Telescope. This far superior data enable us to study the local variation of velocity and magnetic field associated with the UD evolution in the statistical way. The main results are summarized as follows: (1) Statistically, there seem to be no differences between UDs born in the umbra and those detached from penumbral grains. (2) Long-lived UDs travel longer distances with slower proper motions. (3) UDs show clear hints of upflows, as predicted by the MHD simulation of Schüssler & Vögler (2006). By contrast, we could not find systematic and persistent downflow signals associated with UDs. (4) We confirm that the magnetic field of UDs is weaker and more inclined than that of the surroundings, as reported previously (e.g., Riethmüller et al. 2008). However, UDs that appear in the strong field background or are in the decay phase show enhanced and more vertical fields. (5) There are strong field regions at the migration front of UDs detached from penumbral grains, as if their motion were impeded by the strong ambient field. Especially, the items (4) and (5) are reported for the first time. These results are consistent with recent MHD simulations of nearly field-free convection in UDs.

We devised a schematic UD model to explain the observed UD properties (Figure 59). The yellow region corresponds to UDs with reduction of field strength and upflow. It emerges into the vertical (or pre-existing) magnetic fields and expands them. Because of the expanding, red colored regions, i.e., surrounding and above the UDs, receive compression and increase their field strength. The MHD simulation in Bharti et al. (2010) (see Figure 14 in their paper) shows UDs harboring strong magnetic field at their peripheries. The line formation height is indicated by the gray or the green band. For the central and peripheral UD case, the formation height is too high to observe the reduction of field and upflow. For grain-origin UDs, especially at the appearance phase when the background field strength is weak, the formation height is deep enough to reach the reduced field region. When an UD disappears the hot gas region goes down, and thus we tend to observe the increase of field strength.

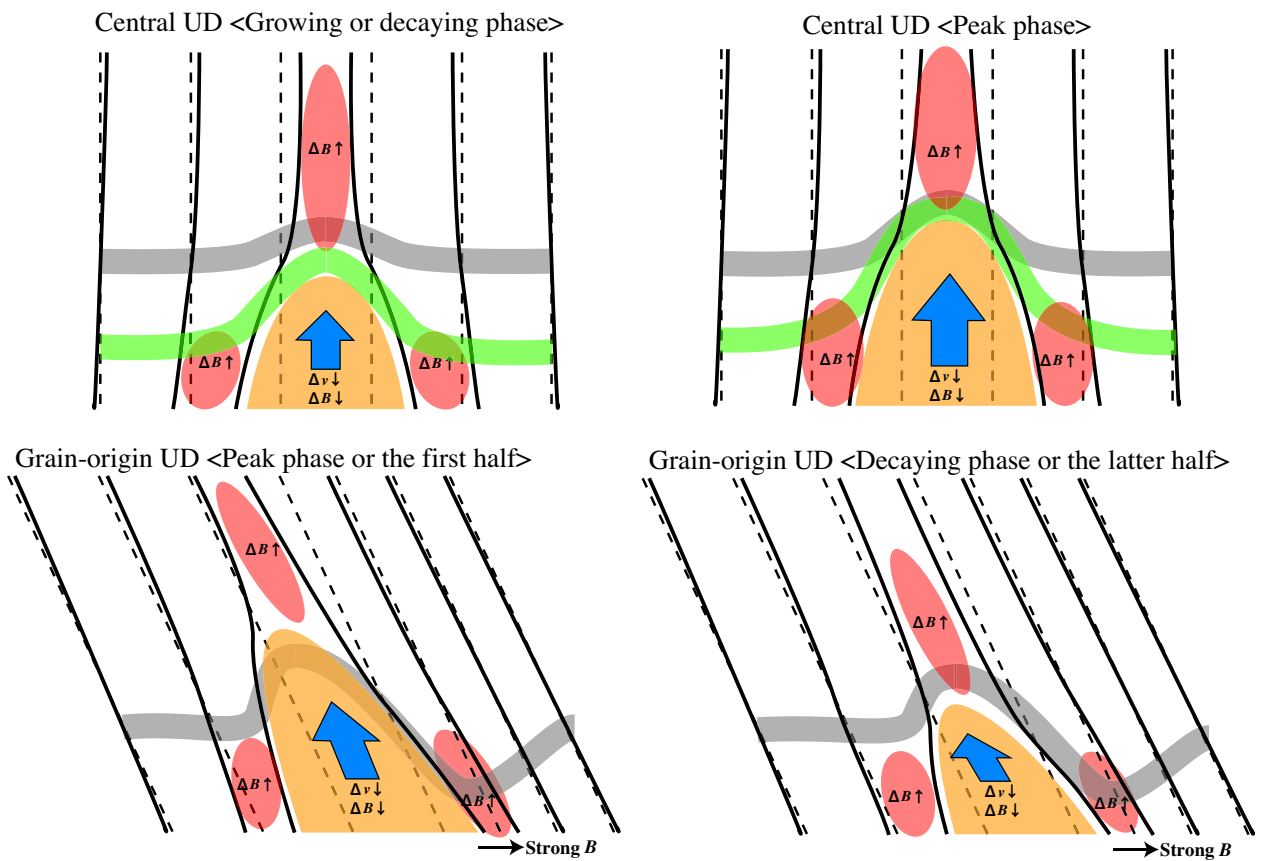


Fig. 59.— The illustrative model of central (top) and grain-origin (bottom) UDs. The near-vertical black lines mean the pre-existing (dash line) and modified (solid line) magnetic field lines. The yellow region corresponds to the hot plasma plume observed as UDs at the surface. The gray band and the green band indicate the line formation height. See the text for further explanation.

5.2. Open Issues

The fine structures in the solar sunspots have proved to be a source of fascinating researches, since the first observation by Chevalier (1916). The research progress is accelerating, as new observing and computer technologies have made great advances. In spite of the rapid progress, a number of questions remain unanswered or disagreed. A selection of such questions is listed below, with the author's outlooks.

- Can UDs give a conclusive answer to the subsurface structure of sunspots: monolithic or cluster?
 - The cluster-like distribution of UD's appearances may reflect the global substructure of a cluster-type sunspot. However the UD physics itself is confined within the near surface of the photosphere, where the monolithic assumption works to a large extent. The author considers the realistic sunspot structure may be somewhere in-between the monolithic and the cluster model.
- How do UDs contribute to the intrinsic brightness of umbrae?
 - It is roughly estimated that UDs contribute 10–20% of the umbral brightness, but its process and the qualitative estimate have not been detailed. The lack of the downflow associated with the overshooting upflow at UDs is one of the evidence of heat injection to the upper atmosphere. In the MHD simulation, the injection above UDs are driven by the release of the pressure enhancement to the upper, less-dense atmosphere. Higher spatial resolution observations is necessary to detect signatures associated with this injection.
- Why are the average size and lifetime of UDs in the umbra so similar for all categories (central and peripheral) and for all sunspots?
 - Our researches including other previous literatures reveal no dependency of UD size and lifetime on the magnetic field strength, field inclination, and belonging sunspots. The physics which determines the typical, minimum, or maximum size and lifetime of UDs has not been clarified. The comparison with UDs in pores may give an important insight.
- Are UDs in pores (free of penumbrae) and sunspots different?
 - At a rough investigation, UDs in pores have larger size and more turbulent motion. There are no systematic inward migration for pore UDs. The systematic analysis has not yet performed, but this work may provide the knowledge about the role of penumbrae on the UD kinetics.

- Is there chromospheric counterpart of the photospheric UDs?
 - No literature has provided a definitive evidence about a connection between chromospheric umbral oscillation and UDs. The existence of chromospheric UDs is reported by only a few literatures. Multi-layer spectroscopic observations are necessary to identify the chromospheric counterpart of UDs.
- How do UDs contribute to the decay of sunspots?
 - The rapid-moving UDs are proved to be a precursor of the light-bridge formation. As light bridges are often observed in the decay phase of sunspots, UDs should play a role in the sunspot decay. The property of UDs such as the speed of their proper motion can show a characteristic signature before the change of the field configuration occurs. The characteristic change of UDs according to their affiliated sunspot's evolution is an interesting topic.
- Are UDs in the different phase of the solar cycle different?
 - No one has studied the characteristic difference of UDs on the phase of the solar cycle. UDs in the solar minimum and those in the solar maximum can be different, because of the different subsurface condition of magnetic field. In the coming ten years, this kind of challenging work will be possible to be started by the data accumulation of the *Hinode* satellite.

The resolution of these questions needs either or both of observations with high spatial and temporal resolution and computer simulations with more realistic models. The local helioseismic observations may play an important role.

5.3. Concluding Remarks

The author's work provided many important knowledges about UD structures and the physics of the magnetoconvection. It is clear that the UD remains a rich area of research with many features left to explore. The coming ten years will be the best time to perform this study, because new large aperture ground-based telescopes (4-m Advanced Technology Solar Telescope; Rimmele et al. 2011) and space satellites (SOLAR-C Mission; Katsukawa & Solar-C Working Groups 2011) are planned and will start their operations.

The future study of UDs should proceed to the cooperative study with the geophysics scientists, for the purpose of the space weather forecast. Sunspots are the sites of large energetic phenomena such as solar flares, and UDs can be an important observational signature

to derive the sunspot's subsurface structure, phase of the evolution, and source of chromospheric umbral heating. The ultimate understanding of sunspots through the knowledge of UDs will lead to the reliable space weather forecast, and helps to secure a safer environment of the space.

REFERENCES

- Bharti, L., Beeck, B., & Schüssler, M. 2010, *A&A*, 510, A12
- Chevalier, S., 1916, *Ann. Obs. Astron, Zo-Sè*, 9, B1
- Jurčák, J., Martínez Pillet, V., & Sobotka, M. 2006, *A&A*, 453, 1079
- Katsukawa, Y., et al. 2007, *PASJ*, 59, 577
- Katsukawa, Y., & Solar-C Working Groups 2011, *Astronomical Society of the Pacific Conference Series*, 437, 281
- Leka, K. D. 1997, *ApJ*, 484, 900
- Parker, E. N. 1979, *ApJ*, 230, 905
- Riethmüller, T. L., Solanki, S. K., & Lagg, A. 2008, *ApJ*, 678, L157
- Rimmele, T. R., Keil, S., Wagner, J., & ATST Team 2011, *Bulletin of the American Astronomical Society*, 801
- Scharmer, G. B., Nordlund, Å., & Heinemann, T. 2008, *ApJ*, 677, L149
- Schüssler, M., Vögler, A. 2006, *ApJ*, 641, L73
- Spruit, H. C., & Scharmer, G. B. 2006, *A&A*, 447, 343
-